University of California

Los Angeles

Spontaneous Thermal Waves and Exponential Spectra Associated with a Filamentary Pressure Structure in a Magnetized Plasma

A dissertation submitted in partial satisfaction

of the requirements for the degree

Doctor of Philosophy in Physics

by

David Carl Pace

2009

© Copyright by
David Carl Pace
2009

The dissertation of David Carl Pace is approved.

James E. Maggs

Mark Moldwin

Walter Gekelman

George J. Morales, Committee Co-chair

Troy A. Carter, Committee Co-chair

University of California, Los Angeles

2009

To my parents, Robert and Tina

Table of Contents

1 Introduction **1**

1.1 Motivation 1

1.2 Low Frequency Turbulence 6

1.3 Summary of Thesis Results 7

1.3.1 Confirmation of Physics Results Due to Plasma Geometry 7

1.3.2 Thermal Wave 8

1.3.3 Exponential Spectra 9

1.4 Thesis Outline 11

2 Experimental Setup and Overview of the Temperature Filament 13

2.1 Large Plasma Device 13

2.2 Temperature Filament Setup 15

2.2.1 Afterglow Plasma 15

2.2.2 Basic Overview 16

2.2.3 Heating Source: Lanthanum Hexaboride Electron Beam . . 17

2.2.4 Diagnostics 20

2.2.5 Measuring Electron Temperature 21

2.2.6 Measuring Parallel Flow 27

2.2.7 Transport Modeling 30

2.3 Filament Behavior 31

2.3.1 Temporal Behavior 31

2.3.2 Spatial Behavior 36
2.3.3 Spatiotemporal Evolution 38
2.4 Relationships Between Physics Results and Filament Behavior . . 40
2.4.1 Thermal Waves Appear in the Filament Center 40
2.4.2 Exponential Spectra Occur in the Anomalous Transport Regime 40

3 Identification of a Spontaneous Thermal Wave 41
3.1 Observations of a Thermal Wave 42
3.2 Theory 45
3.3 Calculating Electron Collision Frequency based on Thermal Wave Properties 50
3.4 Summary 53

4 Exponential Frequency Spectrum and Lorentzian Pulses 55
4.1 Observations of Exponential Spectra and Pulse Structures 56
4.2 Exponential Spectra in the Temperature Filament Environment . 59
4.2.1 Spatial Details 59
4.2.2 Temporal Details 61
4.2.3 Interaction Between Thermal Wave and Drift-Alfvén Mode 63
4.3 Lorentzian Pulses 70
4.4 Comparison Between Spectra and Pulses at Different Axial Positions 73
4.5 Modeling Exponential Power Spectra 78
4.6 Generation of Lorentzian Pulses 81

4.7 Summary . . . 81

5 Comparisons Between Turbulent Features of the Temperature Filament and Limiter-Edge Experiments . . . 83

5.1 About the Limiter-Edge Experiment . . . 83

5.2 Similarities Between the Limiter-Edge and Temperature Filament Experiments . . . 84

5.3 Exponential Spectra . . . 85

5.4 Lorentzian Pulses . . . 87

5.5 Distortion of Lorentzian Pulses . . . 89

5.6 Summary . . . 91

6 Plasma Flow Parallel to Background Magnetic Field . . . 93

6.1 Spatiotemporal Behavior and Modeling . . . 93

6.2 Relation to Thermal Wave . . . 100

6.3 Flow as a Function of Input Power . . . 102

6.4 Summary . . . 106

7 Conclusions . . . 108

7.1 Spontaneous Thermal Waves . . . 108

7.2 Exponential Power Spectra Related to Lorentzian Pulses . . . 109

7.3 Future Work . . . 110

7.3.1 Thermal Waves . . . 110

7.3.2 Exponential Spectra . . . 111

7.3.3 Filamentary Structures . . . 111

A Wavelet Analysis to Calculate Power Spectra 113

A.1 Overview 113

A.2 Parameters of Wavelet Analysis 114

A.3 Fixed Frequency Test Signals 117

A.4 Evolving Frequency Test Signals 119

A.5 Experimental Data 121

B Pulse Detection Techniques 124

B.1 Overview 124

B.2 Wavelet Phase Method 124

B.2.1 Test Lorentzian Pulses 125

B.2.2 Application to Experimental Results 128

B.2.3 Limitations of the Wavelet Phase Detection Technique . . 129

B.3 Amplitude Threshold Method 130

Bibliography 134

List of Figures

1.1 Satellite image of coronal loops on the Sun. 2

1.2 Filamentary pressure structures photographed in the MAST fusion device. 3

1.3 Spectrogram showing transition from coherent modes to broadband spectra and simultaneous appearance of Lorentzian pulses. . 5

1.4 Exponential spectrum in the presence of coherent modes. 10

2.1 Schematic of the Large Plasma Device 13

2.2 Discharge current and electron density throughout an LAPD-U pulse. 16

2.3 Diagram of the temperature filament geometry. 17

2.4 Photograph of the LaB_6 electron beam. 18

2.5 Circuit diagram of the electron beam heat source. 19

2.6 Photograph of heated LaB_6 crystal in plasma. 20

2.7 Example I-V characteristics from alternative sweep method. . . . 23

2.8 Electron temperature at the radial center of the filament measured using the swept probe technique. 24

2.9 Photograph of triple probe head against a ruler. 25

2.10 Circuit diagram of the triple probe system. 26

2.11 Electron temperature measured using the triple probe technique. . 27

2.12 Ion saturation current measurements from both sides of a Janus probe compared to the calculated flow. 29

2.13 Time trace comparing the filament temperature to the background afterglow temperature, along with the beam current. 32

2.14 Cross-covariance contour of the drift-Alfvén ($m = 1$) mode along with narrow time traces of coherent oscillations typically observed early in the filament evolution. 35

2.15 Radial and two-dimensional profiles of the temperature filament. . 37

2.16 Diagram of radial regions of interest. 38

3.1 Average power spectrum highlighting the coherent modes in the radial center of the filament. 43

3.2 Electron Temperature Oscillations Corresponding to a Thermal Wave 44

3.3 Time series of collected probe current illustrating the long-term presence of low frequency fluctuations. 45

3.4 Theoretial prediction of thermal wave cavity length. 48

3.5 Thermal wave oscillations in comparison to theoretical model. . . 50

3.6 Radial Profile of the Thermal Wave 52

4.1 Electron temperature time series at $(r, z) = (0.8, 384)$ cm. 57

4.2 Electron temperature power spectra from three different times at the position $(r, z) = (0.8, 384)$ cm. 58

4.3 Diagram of the radial structure of the temperature filament. . . . 60

4.4 Spectrogram showing transition from coherent modes to broad-band spectra and simultaneous appearance of Lorentzian pulses. . 62

4.5 Extracted time slices from spectrogram comparing pre- and post-transition spectra. 63

4.6 Contour of I_{sat} at $z = 64$ cm along with markings indicating the position of additional fixed probes. 64

4.7 Time series of I_{sat} measurements at different positions within the same discharge. 65

4.8 Sample data extraction region from amplitude threshold pulse detection. 68

4.9 Radial I_{sat} profiles corresponding to the temperature filament's behavior during pulse detection in the outer region. 69

4.10 Lorentzian pulse exhibiting positive polarity. 72

4.11 Lorentzian pulse exhibiting negative polarity. 73

4.12 Time series of I_{sat} at two different axial positions. 74

4.13 Pulses identified in I_{sat} traces from the same plasma discharge. . . 75

4.14 Power spectra of I_{sat} measurements from different axial positions during the same discharges. 76

4.15 Pulses and corresponding Lorentzian fits. 78

4.16 Exponential power spectrum comparison with model. 80

5.1 Schematic of the limiter-edge experiment. 84

5.2 Density profile from the limiter-edge experiment. 85

5.3 Ion saturation current traces from the limiter-edge experiment. . . 86

5.4 Exponential power spectra from the limiter-egde experiment. . . . 87

5.5 Example of a negative polarity pulse from the limiter-edge experiment. 88

5.6 Example of a positive polarity pulse from the limiter-edge experiment. 88

5.7 Functional curve fit to an asymmetric pulse measured in the limiter-edge experiment. 90

5.8 Comparison of power spectra for skewed Lorentzian curve fits. . . 91

6.1 Time series of parallel flow with comparison to theoretical result. . 94

6.2 Two-dimensional parallel flow profile through time compared to the theoretical prediction. 95

6.3 Radial profiles of parallel flow from measurements and modeling. . 96

6.4 Contours of parallel flow at different axial positions. 98

6.5 Temporal evolution of parallel flow at the filament center for three axial positions. 100

6.6 Parallel flow demonstrating repeatable pattern at the period of the thermal wave. 101

6.7 Parallel flow at the filament center for multiple axial positions and input heating powers. 103

6.8 Theoretical axial profiles of electron temperature for different beam voltages. 105

6.9 Theoretical parallel Mach number for different values of the electron beam voltage. 106

A.1 Test signals used to validate wavelet power spectrum technique. . 116

A.2 Identification of a 5 wave using different wavelet basis functions. . 117

A.3 Power spectra from wavelet and Fourier techniques. 119

A.4 Test signal featuring the sudden appearance of a secondary frequency. 120

A.5 Wavelet spectrogram of the evolving frequency test signal. 121

A.6 Spectrograms of electron temperature fluctuations comparing wavelet and Fourier methods. 122

B.1 Phase contours of test signal Lorentzian pulses calculated using wavelet methods. 126

B.2 Phase versus frequency for test signal Lorentzian pulses of varying width. 127

B.3 Comparison of wavelet phase contours for positive and negative polarity Lorentzian pulses. 128

B.4 Measured pulse and corresponding wavelet phase contour. 129

B.5 Floating potential and ion saturation current time series of axially separated probes. 130

B.6 Fluctuating I_{sat} signal and corresponding temporal evolution of RMS fluctuation level. 131

B.7 Time series of I_{sat} with pulses identified using the amplitude threshold method. 132

B.8 Example false positive peak detection with the amplitude threshold method. 133

List of Tables

2.1 LAPD-U Parameters 14

4.1 Calculated Pulse Widths 77

Acknowledgments

I would like to thank my advisors, Dr. James Maggs and Professors Troy Carter and George Morales, for their countless hours of support throughout the duration of this thesis effort. I am especially grateful to Troy for providing me with an opportunity to begin a research project as soon as I arrived at UCLA, and for mentoring me throughout my graduate career. I feel fortunate to have worked with James and George. Their thoughtful review of this work has made me a better physicist.

I am grateful to everyone in the LAPD-U laboratory. Professor Walter Gekelman directs a healthy research environment that was a great pleasure to experience. The research staff, including Steve Vincena, Marvin Drandell and Zoltan Lucky, always came to my aid at the potentially most stressful times when a mechanical problem needed to be solved quickly. Additionally, I thank Marvin for helping me get into the lab many times while I was using crutches following knee surgery. I am grateful for the camaraderie of my fellow graduate students. Brian Brugman provided many humorous discussions, in addition to useful plasma physics ones, while taking classes together and learning our way through the lab.

I am fortunate to have had a unique and positive experience during my first research project in the Electric Tokamak Laboratory at UCLA. I am grateful to Dr. Robert Taylor for sharing his immense experience in tokamak physics and excitement for fusion energy. Pierre Gourdain and Dave LaFonteese eased my transition to graduate school with their friendship.

I am thankful for the never ending support of my wonderful family. My parents, Robert and Tina, have continually supported my decade-long collegiate

effort in pursuit of this degree. This thesis is dedicated to them. I am grateful to my brothers, Robert and Nicholas, for their interest in my work and even more so for their willingness to listen to my descriptions. I am ever thankful to my grandparents, William and Joan, for their love and support. They taught me to use tools from the age of three, and that surely set me along the path to become an experimental physicist. I am also fortunate to have added wonderful family along the way. I am grateful to my wife, Anne, for her patience and support in addition to her critical review of my work. I also thank my in-laws, John and Mary, for accepting me into their family with open arms. I am grateful to my brother-in-law and his wife, John Michael and Manisha, for making me part of the family.

Vita

August 7, 1979	Born, Lodi, California, USA.
2002	B.Sc. Physics University of the Pacific Stockton, California
2003	M.Sc. Physics University of California, Los Angeles Los Angeles, California
2003 - 2008	Ph.D. Research in the LAPD-U Laboratory University of California, Los Angeles Los Angeles, California

Publications

D. C. Pace, M. Shi, J. E. Maggs, G. J. Morales, and T. A. Carter, "Exponential Frequency Spectrum and Lorentzian Pulses in Magnetized Plasmas," Phys. Plasmas 15, 122304 (2008)

D. C. Pace, M. Shi, J. E. Maggs, G. J. Morales, and T. A. Carter, "Exponential Frequency Spectrum in Magnetized Plasmas," Phys. Rev. Lett. 101, 085001 (2008)

D. C. Pace, M. Shi, J. E. Maggs, G. J. Morales, and T. A. Carter, "Spontaneous Thermal Waves in a Magnetized Plasma," Phys. Rev. Lett. 101, 035003 (2008)

R.J. Taylor, T.A. Carter, J.-L. Gauvreau, P.-A. Gourdain, A. Grossman, D.J. LaFonteese, D.C. Pace, L.W. Schmitz, A.E. White, and T.F. Yates. Nuclear Fusion, 45(12):16341641, 2005.

Abstract of the Dissertation

Spontaneous Thermal Waves and Exponential Spectra Associated with a Filamentary Pressure Structure in a Magnetized Plasma

by

David Carl Pace

Doctor of Philosophy in Physics

University of California, Los Angeles, 2009

Professor Troy A. Carter, Co-chair

Professor George J. Morales, Co-chair

An experimental study of plasma turbulence and transport is performed in the fundamental geometry of a narrow pressure filament in a magnetized plasma. An electron beam is used to heat a cold background plasma in a linear device, the Large Plasma Device (LAPD-U) [W. Gekelman et al. Rev. Sci. Instrum. **62**, 2875 (1991)] operated by the Basic Plasma Science Facility at the University of California, Los Angeles. This results in the generation of a filamentary structure ($\approx$ 1000 cm in length and 1 cm in diameter) exhibiting a controllable radial temperature gradient embedded in a large plasma. The filament serves as a resonance cavity for a thermal (diffusive) wave manifested by large amplitude, coherent oscillations in electron temperature. Properties of this wave are used to determine the electron collision time of the plasma and suggest that a diagnostic method for studying plasma transport can be designed in a similar manner. For short times and low heating powers the filament conducts away thermal energy through particle collisions, consistent with classical theory. Experiments performed with

longer heating times or greater injected power feature a transition from the classical transport regime to a regime of enhanced transport levels. During the anomalous transport regime, fluctuations exhibit an exponential power spectrum for frequencies below the ion cyclotron frequency. The exponential feature has been traced to the presence of solitary pulses having a Lorentzian temporal signature. These pulses arise from nonlinear interactions of drift-Alfvén waves driven by the pressure gradients. The temporal width of the pulses is measured to be a fraction of a period of the drift-Alfvén waves. A second experiment involves a macroscopic (3.5 cm gradient length) limiter-edge geometry in which a density gradient is established by inserting a metallic plate at the edge of the nominal plasma column of the LAPD-U. In both experiments the width of the pulses is narrowly distributed, resulting in exponential spectra with a single characteristic time scale. The temperature filament experiment permits a detailed study of the transition from coherent to turbulent behavior and the concomitant change from classical to anomalous transport. In the limiter experiment the turbulence sampled is always fully developed. The similarity of the pulse shapes and fluctuation spectra in the two experiments strongly suggests a universal feature of pressure-gradient driven turbulence in magnetized plasmas that results in non-diffusive cross-field transport. This may explain previous observations in helical confinement devices, research tokamaks and arc-plasmas.

CHAPTER 1

Introduction

1.1 Motivation

Anomalous transport is an area of great interest within the plasma physics research community. The field of magnetically confined thermonuclear fusion may benefit significantly from an improved understanding of this topic. It has already been shown that turbulent fluctuations increase the transport of mass and energy [Horton, 1999] in magnetically confined laboratory plasmas. Improved confinement can expedite the development of fusion reactors as controllable energy sources.

Space plasma research also encounters anomalous transport [Committee on Solar and Space Physics, 2004] across naturally occurring boundaries in temperature, density, and magnetic field. The modeling of space weather can be beneficially impacted by improvements in plasma transport understanding.

Filamentary pressure structures, meaning structures that are aligned along magnetic field lines with narrow radial extent compared to their length, are prevalent in both space and fusion plasmas. Figure 1.1 is a satellite photograph of the solar corona in which bright filaments are seen flowing along looping magnetic field lines. Energy transport along these filaments, and even through the solar wind en route to interaction with the Earth's magnetic field, are ongoing areas of research. An example of filamentary structures from a fusion device is seen in

Fig. 1.2, a photograph from the MAST fusion device. This image shows bright filaments in the outer edges of the device. They are the manifestation of edge-localized modes (ELMs) that transport hot plasma from the center of the device out to the walls. Controlling ELMs to minimize their transport or to avoid them altogether is presently a major effort within the fusion community [Evans et al., 2008].

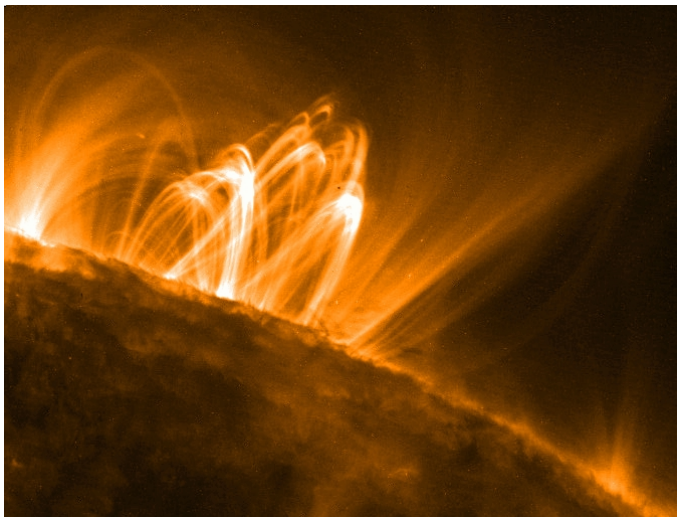

Figure 1.1: Coronal loops on the Sun as imaged by the Transition Region and Coronal Explorer (TRACE) satellite. Filamentary structures form along the magnetic field lines emanating from the Sun. Image taken from Stanford-Lockheed Institute for Space Research.

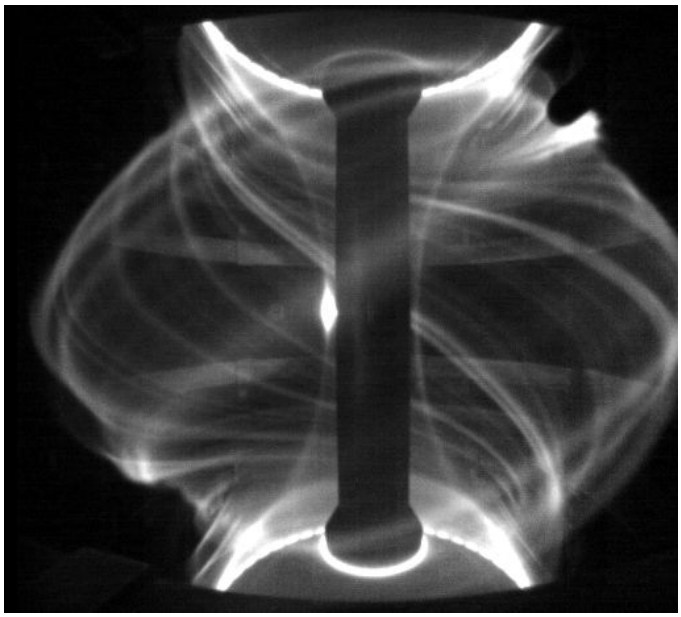

Figure 1.2: Photograph of filamentary structures in the MAST fusion device. Edge-localized modes appear as bright filaments as they conduct large amounts of energy and particles out of the confinement region. Image taken from UKAEA.

Many features of filamentary structures remain unknown, including their capacity for transport, mechanisms leading to their generation, and which plasma waves they may produce. A difficulty in studying these issues within the space and fusion examples above is that the resulting systems are actually a mixture of many individual filaments. Interactions between the filaments and the existence of background instabilities complicate the interpretation of observations. This thesis utilizes an experiment in which a single filamentary structure is generated in the background of a quiescent plasma. The resulting system may be imagined as the isolation of one of the many structures seen in the previous two images. The fluctuation spectra and associated transport generated by this single filament proves rich with dynamic behavior. Studies related to plasma turbulence, sponta-

neously generated temperature waves, and non-linear interactions of drift-Alfvén waves are all performed within this configuration.

The experimental configuration used in this project was originally motivated by the desire to present experimental evidence for classical heat transport in magnetized plasmas. A summary of that successful effort is available as a Ph.D. thesis [Burke, 1999]. The theory of heat transport due to Coulomb collisions [Landshoff, 1949; Spitzer and Härm, 1953a; Rosenbluth and Kaufman, 1958; Braginskii, 1965] was developed nearly 50 years before it was quantitatively validated in a laboratory plasma [Burke et al., 1998, 2000b] using this configuration. The experiment consists of a narrow cylindrical region of warm plasma ($T_e \approx 5$ eV) embedded in a cold background plasma. The heated filament of plasma is manipulated to control the temperature gradient, thus driving classically described heat transport. Classical transport is always initially observed in this experiment, but if the heating is applied over a longer time interval or above a certain temperature threshold, the system transitions to a regime of enhanced, or anomalous, transport greater than that predicted by classical theory. Turbulent fluctuations are observed in this regime, and while some of their features have been investigated [Burke et al., 2000a], a mature understanding requires more detailed experimentation.

A summary of the transition from classical to anomalous transport in this experiment is provided by Fig. 1.3, a spectrogram of I_{sat} power spectra (color contour) with the fluctuating component of a single I_{sat} trace ($\tilde{I}_{sat}$, solid white) overplotted. The heated filament is generated at time $t = 0$ ms and maintained until $t = 12$ ms. Prior to $t = 6$ ms there is one well defined mode between 25 and 45 kHz. This is a drift-Alfvén eigenmode that has been detailed extensively both theoretically [Peñano et al., 2000] and experimentally [Burke et al., 2000a]. The presence of this coherent mode does not alter the transport levels, i.e., the

observed transport remains classical during the presence of the drift-Alfvén wave. After $t = 6$ ms, a transition from coherent spectra to broadband spectra occurs. The transition is delineated by the disappearance of the coherent drift-Alfvén line into a broad region of power spread across many frequencies. Transport levels are enhanced, or anomalous, during times after this transition. All of this behavior occurs within a range corresponding to low frequency turbulence. The low frequency range is an area of active research within plasma physics, as discussed in the following section.

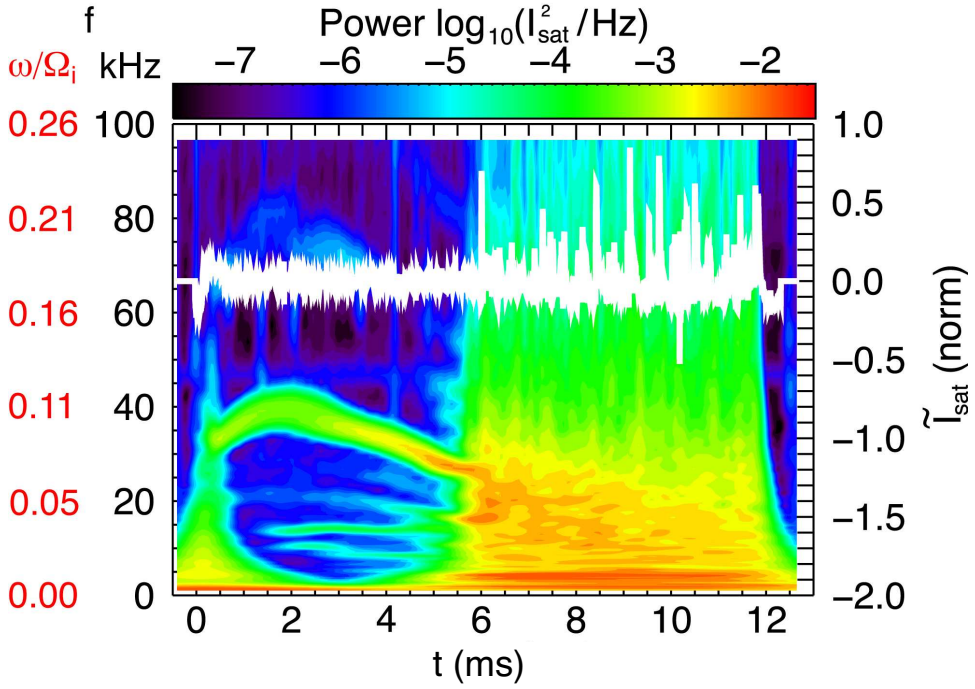

Figure 1.3: Time evolution of the power spectrum (color contour) with an overplot of the fluctuating component of an $I_{\rm sat}$ signal (solid white) from the same spatial position. Coherent fluctuations of the drift-Alfvén eigenmode are visible for $t \leq 5.5$ ms. After 5.5 ms there is a sharp transition to broadband spectra that correlates with the appearance of large relative amplitude pulses in the $I_{\rm sat}$ signal.

1.2 Low Frequency Turbulence

Identification of the processes underlying low frequency turbulence in magnetized plasmas is an ongoing challenge within plasma physics [Krommes, 2002]. By "low frequency" it is meant that the frequency of the fluctuating quantity, ω, is less than the ion cyclotron frequency, Ω_i. This topic is relevant to the magnetically confined fusion research community because turbulent fluctuations can enhance the transport of mass and energy [Horton, 1999], thereby degrading tokamak performance. The topic is also of interest in space plasma efforts [Committee on Solar and Space Physics, 2004] in which enhanced transport across naturally occurring boundaries in temperature, density, and magnetic field can result in major effects observable by space and ground-based instruments.

A significant effort has been devoted to the identification of universal behaviors in the spectra of turbulent fluctuations. A rich literature exists for both laboratory [Chen, 1965; Kamataki et al., 2007; Labit et al., 2007; Škorić and Rajković, 2008; Budaev et al., 2008; Pedrosa et al., 1999; Stroth et al., 2004; Carreras et al., 1999; Zweben et al., 2007] and space [Tchen, 1973; Kuo and Chou, 2001; Milano et al., 2004; Zimbardo, 2006; Bale et al., 2005] plasmas. The cited references are merely a representative sample of the available literature. Kolmogorov's early contribution [Kolmogorov, 1941] has had a major influence in these activities [Frisch, 1995]. In particular, that pioneering work makes a general prediction of algebraic spectral dependencies that has resulted in most modern spectral results being presented in a log-log format. Piecewise fits are then applied in order to extract power-law values for comparison to the Kolmogorov prediction. A large dynamic range is compressed by the log-log display, however, and important features related to the turbulence may be obscured. An exponential frequency spectrum is one such important feature, and its presence

and underlying mechanism are described in this thesis.

1.3 Summary of Thesis Results

In the following an abbreviated description is presented regarding the major results obtained in this thesis. These are:

- Confirmation of previous results due to filamentary geometry.
- Observation of a spontaneous thermal wave in the absence of an externally driven source.
- Observation of exponential power spectra associated with anomalous transport that are generated by Lorentzian pulses in measured time series data.

1.3.1 Confirmation of Physics Results Due to Plasma Geometry

The previously cited work of Burke, et al. was performed in the LAPD device prior to 2000. The present studies are performed in the machine that replaced the original LAPD, which has been named the LAPD-U, signifying it as an "upgrade" over the original. With similar plasma production sources and plasma properties, the major difference between these two machines is their length along the applied background magnetic field. The LAPD featured a plasma of less than 9.4 m in length. The LAPD-U plasma length is approximately 15 m. Throughout this thesis the LAPD-U designation will be used to emphasize the completely different linear device used for this work compared to the foundational efforts conducted on the LAPD.

Precisely because the LAPD-U is a different machine, all of the results in this thesis confirm that fundamental plasma physics is responsible for the observed phenomena, rather than the geometry of a particular device. The LAPD-U pro-

vides boundary conditions that were not present in the previous device, yet the coherent modes observed are the same, along with the important features of transport that have been re-observed.

1.3.2 Thermal Wave

The existence of low frequency, coherent, fluctuations is documented in the earlier work within this experimental environment [Burke et al., 2000a]. Observations show this is a coherent mode that, while seemingly unrelated to the generation of low frequency turbulence, is capable of strongly modulating the drift-Alfvén modes that are excited by the filament. These fluctuations are identified here as representing a spontaneously excited thermal wave. A thermal wave is the diffusive propagation of a temperature oscillation driven by a similarly oscillating source. Although thermal waves in plasmas have been studied [Gentle, 1988; Jacchia et al., 1991], and even manipulated to deduce subtle issues of anomalous transport in tokamaks [Mantica et al., 2006; Casati et al., 2007], controlled experiments in basic plasma devices are made difficult by the geometry of a magnetized plasma. The complexity arises due to the large difference in the thermal conductivities along and across the magnetic field, $\kappa_{\parallel} \gg \kappa_{\perp}$, requiring plasmas with significant length along the magnetic field direction.

The discrepancy in thermal conductivities results in an extended structure that acts as the cavity for a thermal wave resonator [Shen and Mandelis, 1995]. The results presented here represent thermal wave oscillations that appear without the setting of a driver. Other experimental work involving this phenomenon, including those referenced, drive the wave with a controllable heat source. The drive source is as yet unidentified here, though it is demonstrated that the electron beam heating is not the direct cause, i.e., there are no coherent low frequency

oscillations in the beam source. A possible candidate for the drive source is the heat-flux instability that is found in the solar wind [Forslund, 1970] and in laser-plasma interactions [Tikhonchuk et al., 1995]. This work has been summarized in Pace et al. [2008b].

1.3.3 Exponential Spectra

Figure 1.4 provides an example of an exponential power spectrum from the experiment. In a semi-log display, an exponential dependence appears as a straight line. This behavior is used to calculate the scaling frequency (decay constant) of the spectra for comparison with the time width of the Lorentzian pulses. The coherent peaks in Fig. 1.4 (located at approximately $f = 30, 60, 90$, and 120 kHz) coexist with the exponential behavior that extends from $20 \leq f \leq 200$ kHz.

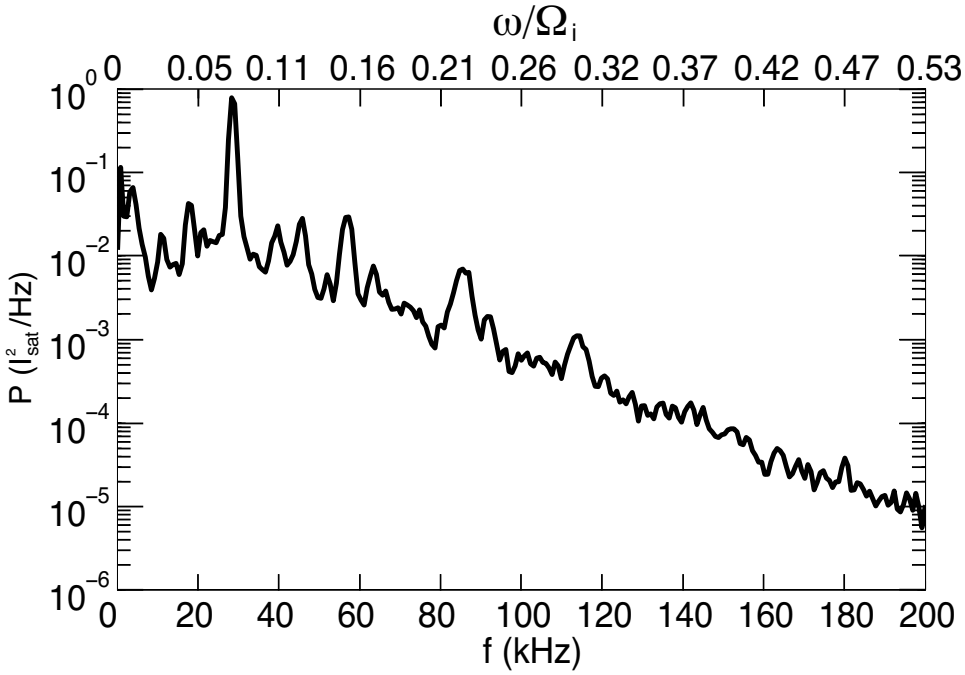

Figure 1.4: Semi-log plot of an I_{sat} power spectrum. Coherent modes, due to the presence of drift-Alfvén waves, can be seen in the range $20 \leq f \leq 120$ kHz and coexist with the exponential in the range $20 \leq f \leq 200$ kHz.

Exponential spectra from a variety of experiments are found throughout the published literature. This is made possible by the semi-log display some researchers have chosen to use for the results. Figure 1a of Xia and Shats [2003] exhibits exponential behavior over four orders of magnitude from floating potential measurements. This experiment was performed in a helical device that reported proof of an inverse cascade. Figure 1 of Fiksel et al. [1995] features an exponential dependence in an experiment observing magnetic fluctuation-induced heat transport. Figure 6b in Kauschke et al. [1990] shows an exponential spectrum with embedded coherent modes for a nonlinear dynamics experiment in a low pressure arc discharge plasma. Figure 7 of Maggs and Morales [2003]

presents an exponential spectrum from magnetic fluctuations at the free edge of the LAPD-U. The exponential spectra in these examples are readily identified because of the semi-log plot display. The appearance of such spectra in a wide variety of experiments suggests that it may also be present in other results where it is simply compressed by a log-log display.

The power spectra, P, of measured fluctuations display an exponential dependence in frequency, $P(f) \propto \exp(-2f/f_s)$, where f_s is a scaling frequency. This exponential feature is only observed after the temperature filament transitions into the enhanced, or anomalous, transport regime. Concomitant with the exponential spectrum is the observation of pulses or spikes in the time series data. These pulses, which can be either upward or downward going in amplitude depending on the measurement location, are Lorentzian in temporal shape. A Lorentzian pulse has an exponential power spectrum, leading to the conclusion that the appearance of these pulses causes the exponential spectrum. A brief summary of this work may be found in Pace et al. [2008a].

1.4 Thesis Outline

This thesis is composed of five chapters. Chapter 2 presents the laboratory device in which this study is performed, along with a review of the various diagnostics employed to measure plasma properties. Chapter 3 details the results surrounding the identification of a spontaneously generated thermal wave in the filament. This is the culmination of an effort to identify coherent oscillations featuring a lower frequency than the other previously known modes of the system. The thermal wave is likely to be supported in many filamentary plasma systems including the solar corona. Modification of the temperature profile by the thermal wave leads to large amplitude pulses in time series signals. These pulses are discussed

in Chapter 4, which also presents evidence for a universal characteristic of power spectra in turbulent plasmas. Such spectra exhibit exponential dependencies in frequency and are found to result from the Lorentzian shape of the measured pulses. Similar spectra, and in many cases similar pulses, are observed in the existing plasma literature and in ongoing research at linear machines and tokamaks. A density gradient experiment performed in the same device as this thesis work also exhibits these pulses and exponential spectra. Chapter 5 compares the density gradient experiment to the temperature filament experiment as part of the argument for the universal nature of the exponential spectra and Lorentzian pulses. Conclusions and a unifying summary of these topics are presented in Chapter 7. Finally, the appendices present results on plasma flows in relation to the primary topics, techniques of wavelet analysis that have been applied in power spectra calculations, and a summary of techniques employed to detect the Lorentzian pulses that generate exponential power spectra.

CHAPTER 2

Experimental Setup and Overview of the Temperature Filament

2.1 Large Plasma Device

The Large Plasma Device (LAPD-U), part of the Basic Plasma Science Facility (BaPSF) at UCLA, provides an ideal parameter regime in which to perform this experimental investigation. The present device, as shown in Fig. 2.1, is a larger version of the one described in Gekelman et al. [1991].

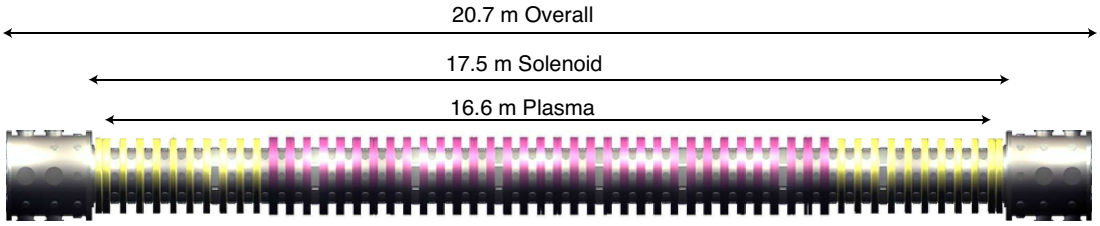

Figure 2.1: Dimensional schematic of the LAPD-U, illustrating the long axial extent that is vital to the parallel heat transport studies performed.

The LAPD-U produces plasma by discharging a cathode-anode pair. A barium-oxide coated, nickel cathode is heated to emission temperature near 850 °C. A wire mesh molybdenum anode is positioned 50 cm away from the cathode. A large capacitor bank connects the pair and discharges a few thousand Amperes of current for some fixed bias voltage (typically in the 65 V range). The anode

mesh is 50% transparent, allowing half of the electrons emitted by the cathode to pass through and travel down the length of the device. This produces plasmas that fill the 20 meter-long vacuum chamber. During the main discharge (a flat-top current pulse between the cathode-anode pair lasting up to 12 ms), the resulting plasma column extends up to 60 centimeters in diameter.

The LAPD-U provides a wide range of plasma parameters for study. The solenoidal magnetic field may be set to any value between 500 and 2500 Gauss. Magnetic coil elements are separately connected, allowing for various field configurations (mirror, beach, etc.). Inert gases are typically used to generate plasmas since these do not chemically interact with the oxide coating of the cathode. Table 2.1 lists typical plasma parameters for the LAPD-U.

Parameter	Symbol	Range
Magnetic Field	B_o	500 - 2500 Gauss
Electron Density	n_e	1 - 3 $\times 10^{12}$ cm^{-3}
Electron Temperature	T_e	6 - 8 eV
Ion Temperature	T_i	1 eV
Ion Cyclotron Frequency	Ω_i	190 - 950 kHz
Electron Collision Frequency	ν_e	$\approx$ 3.5 MHz
Electron Thermal Speed	v_{the}	$\approx 1 \times 10^8$ cm^{-3}

Table 2.1: LAPD-U Parameters

2.2 Temperature Filament Setup

2.2.1 Afterglow Plasma

The principal results of this thesis are obtained in the afterglow phase of the LAPD-U plasma. The afterglow is a common term used to describe the plasma that remains in the vacuum chamber after a cathode discharge has been turned off. Figure 2.2 is a plot of the LAPD-U discharge current (black trace) and the line-averaged electron density (red trace) as measured by an interferometer. A double-sided blue arrow extends across the post-discharge regime in which the plasma is in the afterglow phase. When the discharge shuts off there is no longer a heating source to maintain plasma temperature. Thermal conduction to the ends of the device causes the electron temperature to decay rapidly, on the order of microseconds. Diffusion is a much slower processes, however, so the plasma density decays on the order of milliseconds. As a result, the LAPD-U afterglow plasma features a very low temperature ($T_e, T_i < 1$ eV) while maintaining a moderate density ($n_e \approx 1 \times 10^{12}$ cm^{-3}) for the first 30 ms after the primary discharge ends. Most of the temperature filament experiments begin at a time 0.5 ms after the discharge current ends and last for 10 to 15 ms.

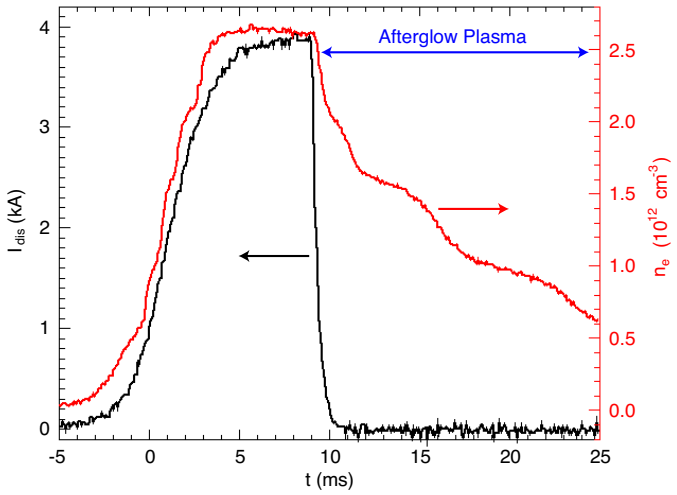

Figure 2.2: Time evolution of the discharge current through the anode-cathode pair (black, I_{dis}) and the line-averaged column electron density (red, n_{e}) during an LAPD-U plasma-pulse.

2.2.2 Basic Overview

A small heat source is applied at one end of the LAPD-U during the early afterglow phase in order to create a temperature filament that is approximately five times hotter than the surrounding background. Plasma properties are measured throughout the resulting three dimensional structure over time scales that allow the relevant transport and turbulence behaviors to arise.

A schematic of this system (not to scale) is given in Fig. 2.3. A cylindrical coordinate system is shown and is referenced throughout this treatment. The axial coordinate is labeled z, the radial coordinate r, and the azimuthal coordinate is θ. The electron beam is located at $(r, z) = (0, 0)$ cm. The heat source is modeled as a one meter long, 3 mm across rigid cylinder of hot plasma that is placed 16 m away from the main cathode/anode. The heating done in this region

is classically transported to setup the filament structure that may reach 12 m in length and 1 cm in diameter. Further details of this system are presented in the following sections.

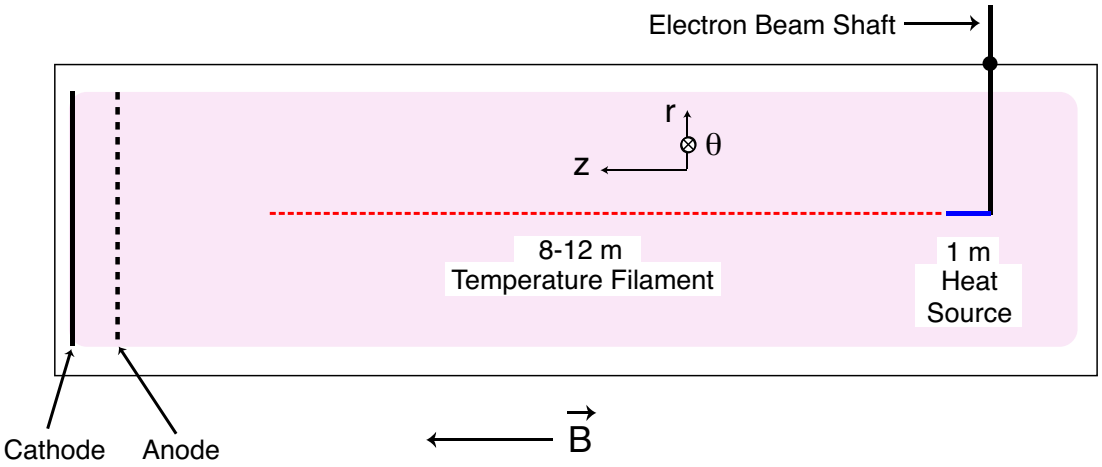

Figure 2.3: Not to Scale. Schematic of the temperature filament experiment highlighting the extended structure parallel to the background magnetic field.

2.2.3 Heating Source: Lanthanum Hexaboride Electron Beam

Plasma heating is accomplished by the injection of energetic electrons from a crystal of lanthanum hexaboride (LaB_6). The work function of LaB_6 is low enough that direct heating of the crystal, accomplished by running current through it, provides adequate energy for thermionic emission. An operating temperature of 1800° K is used. Such crystal temperatures are achieved by running a current through the crystal itself. Figure 2.4 shows the electron beam device as purchased from Applied Physics Technologies (a-p-tech.com): a single crystal of LaB_6 is held in place above a ceramic washer by molybdenum-rhenium (Mo-Re) posts. On the underside of the washer, the posts provide the access point for driving the heater current.

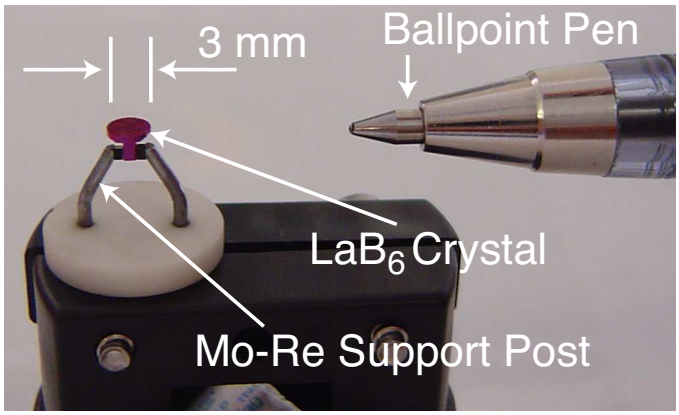

Figure 2.4: Photograph of the LaB_6 electron beam. The beam is a single crystal of LaB_6 permanently fixed in a mounting structure. The crystal is held in place by Mo-Re posts. A common ballpoint pen is provided for scale.

The LaB_6 crystal is mounted on the end of a standard LAPD-U probe shaft and placed in the plasma away from the main cathode/anode (drawn in Fig. 2.3). The main LAPD-U anode also serves as the anode for beam circuit, as shown in the diagram of Fig. 2.5. A heater current is continually run through the crystal to maintain emission temperature at all times during an experiment. The anode connection includes a pulse circuit that applies the beam voltage, V_{beam}, at a prescribed time within each LAPD-U discharge. The applied voltage set by V_{beam} determines the energy of the emitted electrons, which allows the input heating power to be varied. Electron beam current is measured by monitoring the voltage across a 1 Ω resistor connected within the current path. Unless otherwise specified, the beam energy is 20 V for all experiments performed in helium. The ionization energy of helium is approximately 24.6 eV, which allows these experiments to be conducted with minimal concern for density production from the injected electrons. Some experiments are conducted at energies above 24.6 V, but these are not presented as part of the heat transport study.

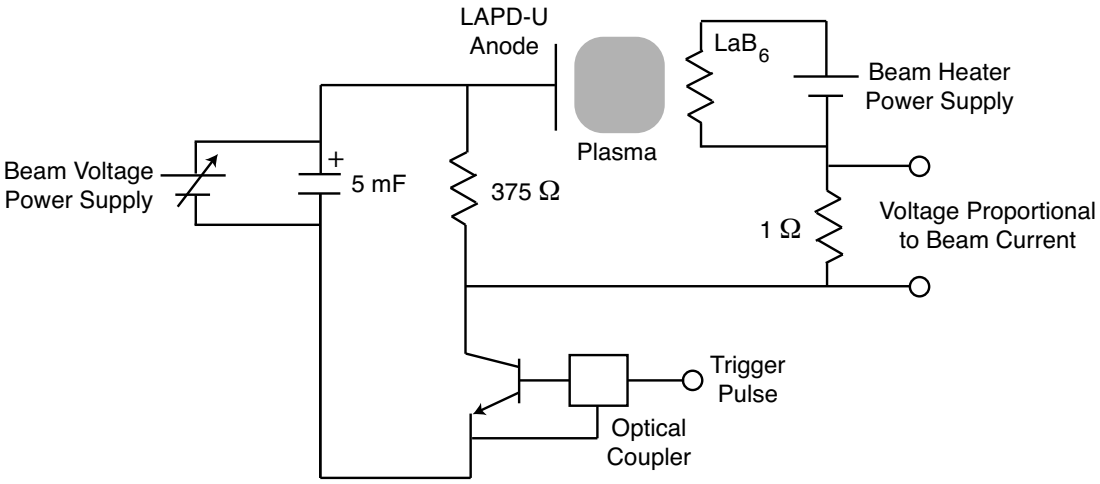

Figure 2.5: Circuit diagram of the electron beam heat source. Beam current is driven between the LaB_6 crystal and the LAPD-U anode through the afterglow plasma.

Figure 2.6 shows the heated crystal embedded in a plasma discharge. The distance between the yellow magnet coils is approximately 32 cm.

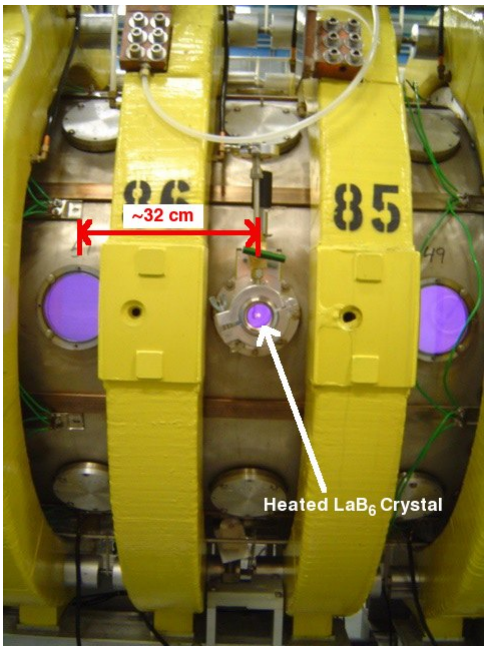

Figure 2.6: The LaB_6 crystal is seen glowing white hot (center) during a discharge pulse in the LAPD-U. The purple background seen inside the small windows is the typical LAPD-U helium plasma.

2.2.4 Diagnostics

The length of the LAPD-U plasma along the applied background magnetic field is approximately 16.6 m. Diagnostic ports are placed every 32 cm along this entire length, allowing for excellent axial resolution in this transport experiment.

Langmuir probes are used because they provide excellent spatial resolution (determined by the size of the probe) and time resolution (limited by the acquisition electronics). Furthermore, probes made out of nearly any metal can withstand the 5 eV plasma temperature throughout an entire experimental run while accessing the entire plasma volume of the device. The probes utilized in this study are made of either tantalum or nickel. Spatial access is provided by

probe drives that move the probes in a full two-dimensional plane at any one axial position. Further details of Langmuir probe usage will be presented immediately preceding the display of results so that the method used to obtain the measurement may be explained in context.

In addition to the fundamental quantities of temperature, density, and flow velocity, the Langmuir probes are used to measure ion saturation current, I_{sat}. Ion saturation current is related to electron temperature and density by $I_{\text{sat}} \propto n_e\sqrt{T_e}$, meaning that fluctuations in these quantities are mixed by an I_{sat} diagnostic. It is shown later that the coherent modes are accurately represented by an I_{sat} measurement in situations where pure density or temperature measurements are not possible.

2.2.5 Measuring Electron Temperature

2.2.5.1 Swept Probe Technique

Electron temperature measurements using Langmuir probes most commonly employ the sweep method. Varying the applied voltage to a probe, V, while recording the current collected, I, results in a current versus voltage characteristic, the I-V curve, that can be fit to determine the electron temperature, electron density and plasma potential. This method is widely known and has been explained in the plasma physics literature (see Ch. 2 of Hutchinson [2002]).

One problem in applying the swept probe method in fluctuation studies is that the parameters obtained represent averages over the time of the complete voltage sweep. A useful measurement of any wave requires the sweep to be performed at well over twice the frequency of the wave so that the Nyquist frequency of the resulting data also remains above that of the wave. A reproducible and

established system for producing such a sweep (with frequency > 50 kHz) is difficult to build due to capacitive effects. An alternate method for measuring electron temperature using the I-V curve is developed.

From I_{sat} measurements it is apparent that the plasma discharge and resulting temperature filament are highly reproducible. This technique involves maintaining a fixed probe voltage for a series of 20 discharges and then incrementing the voltage for the next 20 discharge series. After repeating this procedure for 100 voltages, an ensemble of 2000 discharges is used to construct an I-V characteristic corresponding to every time point of the acquisition. These characteristics allow for the calculation of plasma parameters with time resolution equivalent to that of the common I_{sat} data sets.

Sample I-V traces are shown in Fig. 2.7. Traces from four different time periods are plotted because the voltage range over which the collected current is exponential (i.e., the range over which a fit is inversely proportional to the electron temperature) is found to vary with time. In order to automate the analysis of thousands of data signals it is necessary to determine the voltage range over which the temperature fits should be performed. This required manually examining selected traces from each probe position. The relevant voltage range is different for each region: main LAPD-U discharge (black), early afterglow without beam heating (red), beam heating (green), and late afterglow after the beam is shut off (blue). Electron temperature is calculated through linear fitting of the types of curves shown here, generally within the range $-15 \leq V_{\text{probe}} \leq 5$ V.

Calculation of the temperature is not possible in the late afterglow because the exponential range falls between two of the recorded voltages. There is no possibility of an accurate linear fit since the voltage range is smaller than the voltage resolution of the sweep.

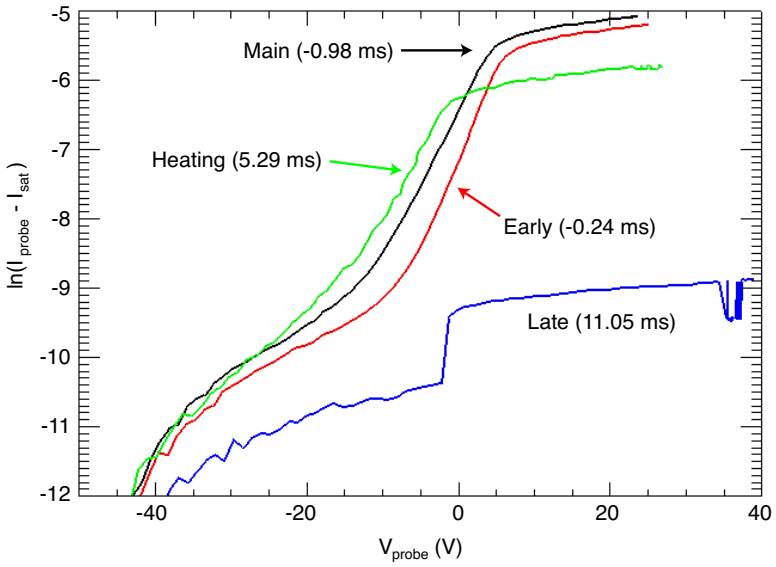

Figure 2.7: Traces of the I-V characteristic are presented from the four distinct regions of plasma heating. The main discharge (black) represents the standard LAPD-U plasma as generated by the cathode-anode system. The early afterglow (red) occurs after the main discharge has ended, but before the beam heating begins. The heating stage (green) represents the primary experiment during which the temperature filament is maintained. Finally, the late afterglow (blue) represents the stage occurring after the beam heating has ended.

An electron temperature measurement acquired from the swept probe technique is shown in Fig. 2.8 for the radial center of the filament. There is no direct filtering of this trace, though fluctuations are reduced by the ensemble nature of the data collection. The steady-state temperature reached in the later half of the time series is also observed with the companion technique for measuring electron temperature, the triple probe technique.

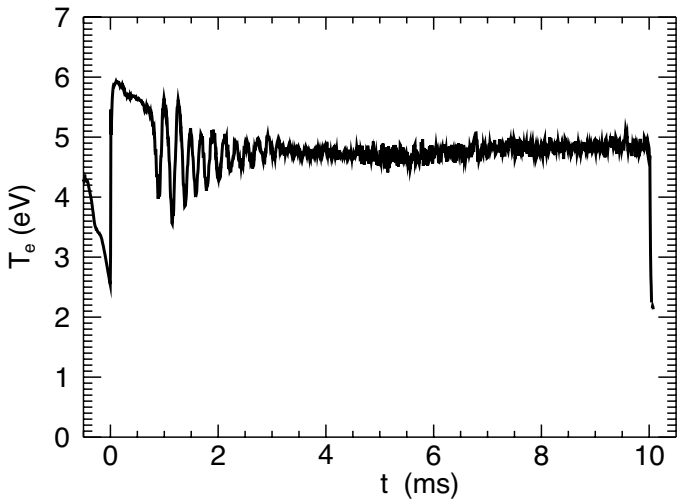

Figure 2.8: Electron temperature in the radial center of the filament and axial position $z = 224$ cm as measured using the swept probe technique.

2.2.5.2 Triple Probe Technique

Electron temperature measurements are also made with triple probes in this thesis. The triple probe technique [Chen and Sekiguchi, 1965] uses three probe tips to simultaneously observe different regions of the I-V characteristic. This provides a continuous measure of temperature, floating potential and ion saturation current. Figure 2.9 shows the three tips of one of the triple probes used. These are 1 mm diameter discs embedded in a low-outgassing epoxy that is plasma facing.

Figure 2.9: Head of a two-sided triple probe placed against a ruler (cm scale). Three disc tips are visible, with another set of three on the other side.

Figure 2.10 is a circuit diagram illustrating the connections between the tips. Tips 1 and 2 are connected in fashion typical of $I_{\rm sat}$ measurements. A fixed bias is applied between them and the voltage across a resistor in series is acquired. The unique aspect of the triple probe is that tip 3 is used to measure floating potential, $V_{\rm f}$. The potential between the tip measuring $V_{\rm f}$ and the electron collecting tip (2) is labeled as $V_{T_{\rm e}}$ and is related to the temperature according to,

$$T_{\rm e} \;=\; \frac{V_{T_{\rm e}}}{\ln(2)}\;, \tag{2.1}$$

which is also derived from Chen and Sekiguchi [1965].

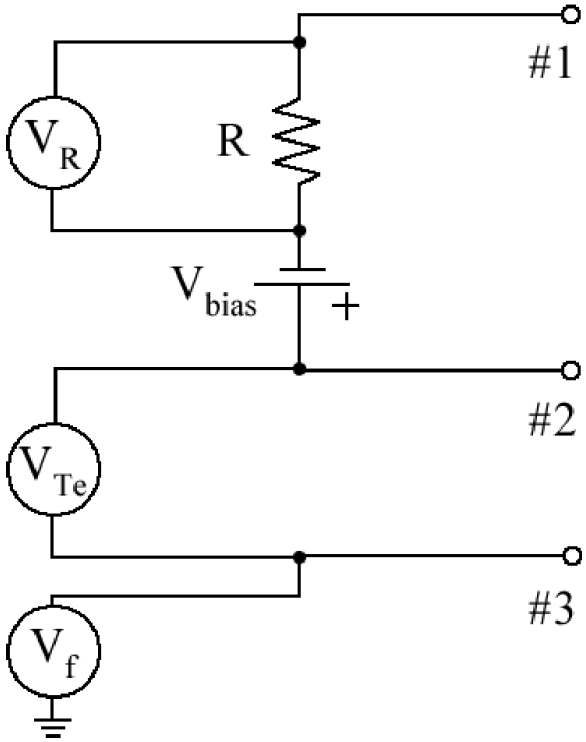

Figure 2.10: Circuit diagram of the triple probe system. The probe tips are numbered and the measurement points are labeled according to whether they record electron temperature (V_{T_e}), floating potential (V_f), or the voltage across the resistor corresponding to ion saturation current (V_R).

An example temperature trace from a triple probe measurement is presented in Fig. 2.11. This result is in qualitative agreement with the swept probe result of Fig. 2.8, even though the measurements are performed in different parameter regimes within different experimental run days. Both temperature traces identify the low frequency, coherent oscillations of the thermal wave (seen at $t = 5$ ms in Fig. 2.11) and a nearly steady-state temperature during the latter half of the heating cycle. Differences between these two results stem from the different background parameters (neutral fill pressure, axial position, heating power, etc.).

The agreement between these very different methods suggests that both are valid in studying the filamentary system.

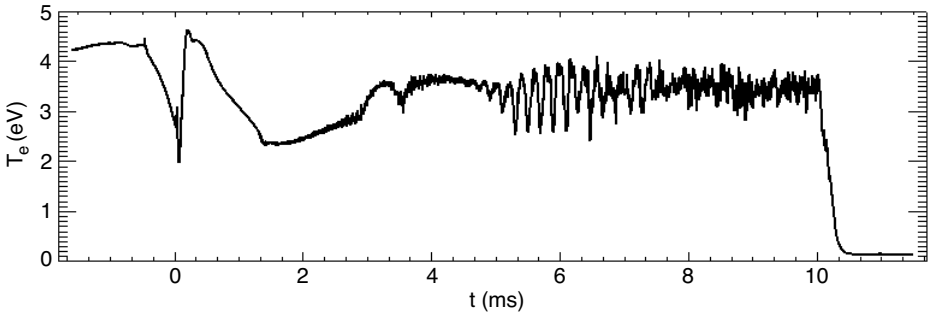

Figure 2.11: Electron temperature as measured using the triple probe technique at the filament center and axial position $z = 384$ cm. While this is a different parameter regime compared to the swept probe measurement of Fig. 2.8, the result is qualitatively similar with respect to the detection of thermal waves and a steady-state temperature at the end of the heating cycle.

2.2.6 Measuring Parallel Flow

The plasma flow measurements employ the Mach probe method of comparing $I_{\rm sat}$ collection on probe faces oriented in opposite directions. That is, the surface normals of the two probe collection areas point in opposite directions. For two such probe faces, the parallel flow Mach number, $M_{\|}$, is (see page 85 of Hutchinson [2002]),

$$M_{\|} \;=\; 0.45 \ln\left(\frac{I_{\rm sat,1}}{I_{\rm sat,2}}\right) \;, \tag{2.2}$$

where 1 and 2 denote the probe faces and the Mach number is defined as $M = v/C_{\rm s}$ where $C_{\rm s}$ is the ion sound speed,

$$C_{\rm s} \;=\; 9.79 \times 10^5 \left(\frac{\gamma Z T_{\rm e}}{\mu}\right)^{-1/2} \;\; {\rm cm/s} \;, \tag{2.3}$$

in which γ is the adiabatic index, Z is the charge factor, and μ is the ion mass factor.

It should be noted that parallel flow results presented here are likely to be underestimates of the actual value. The factor of 0.45 given in Eq. 2.2 may be further modified due to the small size of the Langmuir probe tips compared to the ion gyroradius [Shikama et al., 2005]. Errors associated with probe measurements due to calculation of the effective collection area and pitch-angle with respect to the background magnetic field prevent a significant improvement in the accuracy of the reported flow Mach numbers. Regardless, the qualitative behavior of these results serves as a useful motivation for future efforts.

This analysis can be applied to probe faces with any orientation to the magnetic field, though the parallel orientation is the simplest theoretically. Perpendicular flows are difficult to measure in the temperature filament experiment through the Mach probe method because a probe with full radial and azimuthal diagnostic capability is also large enough to cause a disruptive perturbation. Parallel velocity measurements are made with Langmuir probes featuring the smallest possible surface area. In most cases this is a one millimeter diameter disk or a rectangular tip with the largest dimension on the order of one millimeter.

A limitation of this measurement is that it provides scaled information about the flow velocity with respect to the ion sound speed instead of the absolute velocity. In some instances a temperature measurement is available for the same set of discharges and the calculation of an absolute velocity is possible. In most cases presented in this thesis, however, the Mach probe measurement is performed without an auxiliary temperature measurement and the study focuses on the presence of supersonic flows and their relation to the other processes of the system.

Figure 2.12 demonstrates the calculation of plasma flows using I_{sat} measure-

ments from a double sided, or Janus, probe. These measurements are made at $(r, z) = (0, 64)$ cm, which places the probe within the heating region of beam. Recall that the heating source of this experiment is modeled as a one meter long, three millimeter wide cylindrical plasma made hot by the electrons emitted from the LaB_6 crystal. The orientation of the probe tips in the figure is labeled according to which end of the LAPD-U they face. One tip, the I_{sat} Beam Facing tip, faces the LaB_6 crystal. The other tip, the I_{sat} Anode Facing tip, faces the main anode of the LAPD-U. Flow analysis is performed with the anode facing signal in the denominator of Eq. 2.2, meaning that positive flow values correspond to plasma flowing toward the main LAPD-U anode. This convention is chosen because we expect the flow to dominate in this direction since the pressure gradient source is located at the opposite end of the device.

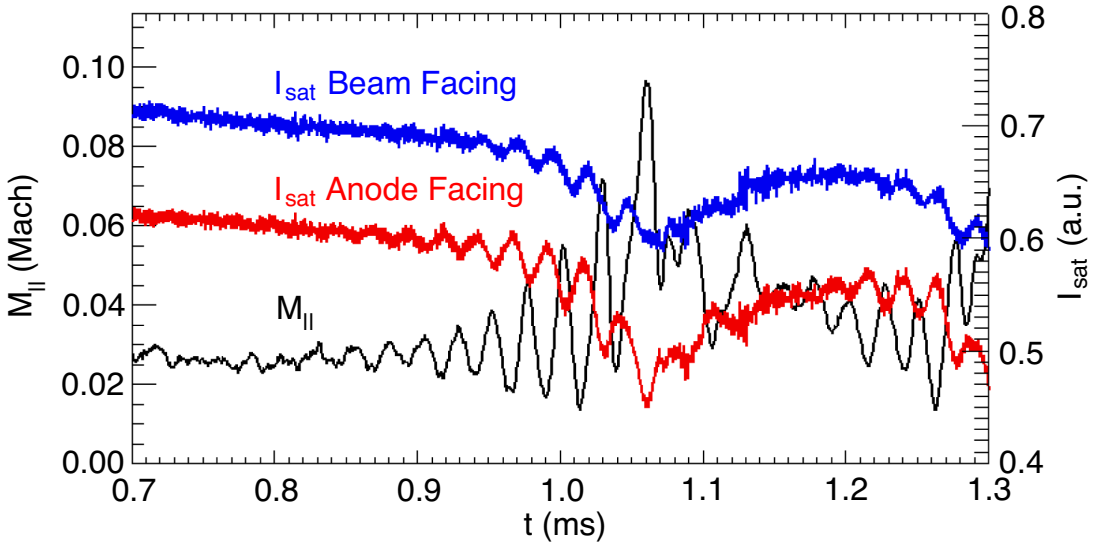

Figure 2.12: $(r, z) = (0, 64)$ cm, $B_o = 900$ G. The I_{sat} traces from both sides of a Janus probe (red and blue) are plotted in comparison to the parallel flow (black) calculated from them.

Coherent oscillations in the parallel flow are observed in Fig. 2.12. From the

raw I_{sat} traces it can be seen that the flow oscillations do not simply mirror the I_{sat} measurements. In particular, the pulse-like event at $t = 1.06$ ms results from the large dip in I_{sat} measured on the anode facing tip and the lack of a similar reduction at the beam facing tip. Later in time at $t = 1.18$ ms a coherent oscillation appears on the anode face and is delayed on the beam face. This behavior results in the calculation of another oscillating flow.

2.2.7 Transport Modeling

The previous work using this experimental geometry to verify the existence of classical heat transport compared measured results with those of a code that modeled classical transport (see Section IV. of Burke et al. [2000b]). A similar effort is incorporated into this thesis.

A thesis in plasma theory by Shi [2008] is a companion to this experimental treatment. The transport code is implemented by Shi is based on the equations of Braginskii [1965]. This set of equations includes the plasma continuity equation, the momentum equation, and the power balance equations. After applying the restraints of quasi-neutrality and cylindrical geometry along with the boundary conditions of the present experiment, these equations reduce to,

$$\partial_{\mathrm{t}} n + \partial\left(n V_{\mathrm{z}}\right) = 0 \,, \tag{2.4}$$

$$\left(m_{\mathrm{i}} + m_{\mathrm{e}}\right) n \left(\partial_{\mathrm{t}} V_{\mathrm{z}} + V_{\mathrm{z}} \partial_{\mathrm{z}} V_{\mathrm{z}}\right) = -\partial_{\mathrm{z}}\left(T_{\mathrm{e}} n + T_{\mathrm{i}} n\right) - R_{\mathrm{in}} \,, \tag{2.5}$$

$$\begin{aligned} \frac{3}{2} n \left(\partial_{\mathrm{t}} T_{\mathrm{e}} + V_{\mathrm{z}} \partial_{\mathrm{z}} T_{\mathrm{e}}\right) + n T_{\mathrm{e}} \partial_{\mathrm{z}} V_{\mathrm{z}} = {} & \frac{1}{r} \partial_{\mathrm{r}}\left(r \kappa_{\perp}^{\mathrm{e}} \partial_{\mathrm{r}} T_{\mathrm{e}}\right) + \partial_{\mathrm{z}}\left(\kappa_{\parallel}^{\mathrm{e}} \partial_{\mathrm{z}} T_{\mathrm{e}}\right) \\ & - 3 \frac{m_{\mathrm{e}} n}{m_{\mathrm{i}} \tau_e} \left(T_{\mathrm{e}} - T_{\mathrm{i}}\right) + Q_{\mathrm{b}} \,, \end{aligned} \tag{2.6}$$

$$\frac{3}{2} n \partial_{\mathrm{t}} T_{\mathrm{i}} = 3 \frac{m_{\mathrm{e}} n}{m_{\mathrm{i}} \tau_e} \left(T_{\mathrm{e}} - T_{\mathrm{i}}\right) - 3 \left(T_{\mathrm{i}} - T_{\mathrm{n}}\right) n \sigma_{\mathrm{n}} \left(\frac{T_{\mathrm{i}}}{m_{\mathrm{i}}}\right)^{1/2} \,, \tag{2.7}$$

where V_{z} is the flow velocity parallel to the background magnetic field, R_{in} is a collision operator for ion-neutral collisions, Q_{b} is the heat input from the electron beam, τ_e is the electron collision period, and σ_{n} is the ion-neutral collision cross-section. The model provides expected classical behavior for the density, electron temperature, and parallel flow evolution. This thesis is concerned with the experimental aspects of the temperature filament environment. The thesis written by Shi is concerned with the theoretical issues of the temperature filament, including heat transport and non-linear interactions between drift-Alfvén waves. Various figures within this thesis will compare measurements with Shi's model results.

2.3 Filament Behavior

2.3.1 Temporal Behavior

The control circuit of the electron beam allows both the heating start time and its duration to be adjusted. The temporal evolution of the temperature filament exhibits three stages, as illustrated by Fig. 2.13. The solid black curve in Fig. 2.13

corresponds to the electron temperature measured, using a small triple probe, at an axial distance 384 cm from the beam injector at the radial center of the filament. For this figure the strength of the confinement magnetic field is 900 G.

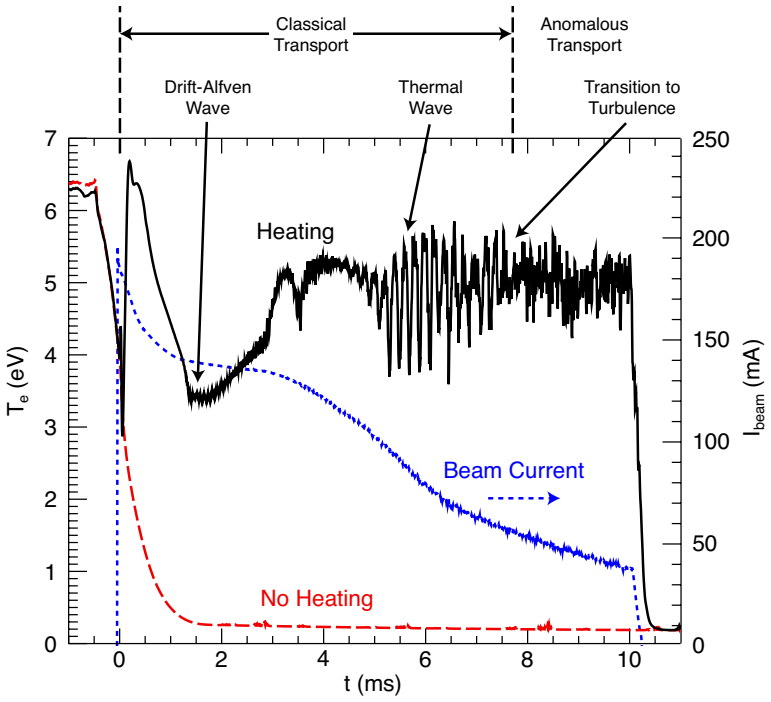

Figure 2.13: Electron temperature and beam current at $(r, z) = (0, 384)$ cm. For the heating case (solid black), the electron beam is activated 0.5 μs after the LAPD-U discharge ends. The heated filament reaches temperatures comparable to that of the main plasma and is much hotter than the background afterglow plasma (dashed red). In this representation the beam current (dotted blue) is an ensemble trace while the heating is from a single shot.

The injected beam current is represented in Fig. 2.13 by the dotted blue curve, with $t = 0$ corresponding to the time when beam injection starts. The dashed red curve shows the decay of the electron temperature in the absence of

beam injection, i.e., during the afterglow. It is seen that the heat source supplied by the beam causes a significant increase in temperature. For an interval of about 2 ms after the beam injection begins, a quiescent temperature evolution is observed. This behavior corresponds quantitatively to that predicted by the classical theory of heat transport based on Coulomb collisions [Braginskii, 1965; Spitzer and Härm, 1953b], as has been documented extensively in previous work [Burke et al., 2000b, 1998]. A second stage can be identified approximately 2 ms after beam injection when high-frequency oscillations become apparent in the electron temperature. These oscillations correspond to coherent drift-Alfvén waves driven unstable by the electron temperature gradient [Peñano et al., 2000] and have been described in detail in a previous publication [Burke et al., 2000a]. A third stage appears after 5 ms of beam injection. At this later time, low-frequency oscillations mixed with incoherent high-frequency oscillations are observed.

Figure 2.14 provides a useful summary of the individual characteristics of the low frequency thermal waves and the higher-frequency drift-Alfvén waves. The time range sampled overlaps between the second and third stages identified in Fig. 2.13, before the broadband develops. The center panel is a two-dimensional (across the magnetic field) spatial domain that covers the full radial extent of the filament. The color contour represents the cross-covariance between I_{sat} signals from Langmuir probes separated by an axial distance of $\Delta z = 160$ cm. One probe is fixed at a position $z = 384$ cm away from the beam injector and at a radial position within the region of measurable drift-Alfvén wave activity. The other probe is placed at $z = 544$ cm and it scans a two-dimensional plane across the confinement magnetic field. Measured signals are digitally band-pass filtered to isolate oscillations due to the drift-Alfvén modes. The cross-covariance is calculated at zero time delay for each plasma discharge over a restricted time interval that captures the largest drift-Alfvén wave. The resulting signal is averaged over

20 independent discharge pulses at every spatial location sampled. The result is an amplitude-dependent measurement of the phase difference between the signals of the two probes, and therefore contains an imprint of the spatial structure of the coherent drift-Alfvén wave at one time in the plasma discharge. The light circular region at the center of the drift-Alfvén wave depicts the highly localized thermal oscillation. The trace in the top panel of Fig. 2.14 shows the time evolution of the ion saturation current at a location $r = 5$ mm, i.e., within the gradient region. It shows the coherent oscillations associated with the two-dimensional snapshot seen in the center panel. These oscillations have typical frequencies in the range of $25 - 40$ kHz. The bottom panel shows the temporal evolution of the ion saturation current at the center of the filament. It is clear that the oscillations here have much lower frequency (by a factor of $5-8$) than those in the gradient region. A cross-modulation that shows the faint presence of the drift-Alfvén mode can be seen in portions of the trace.

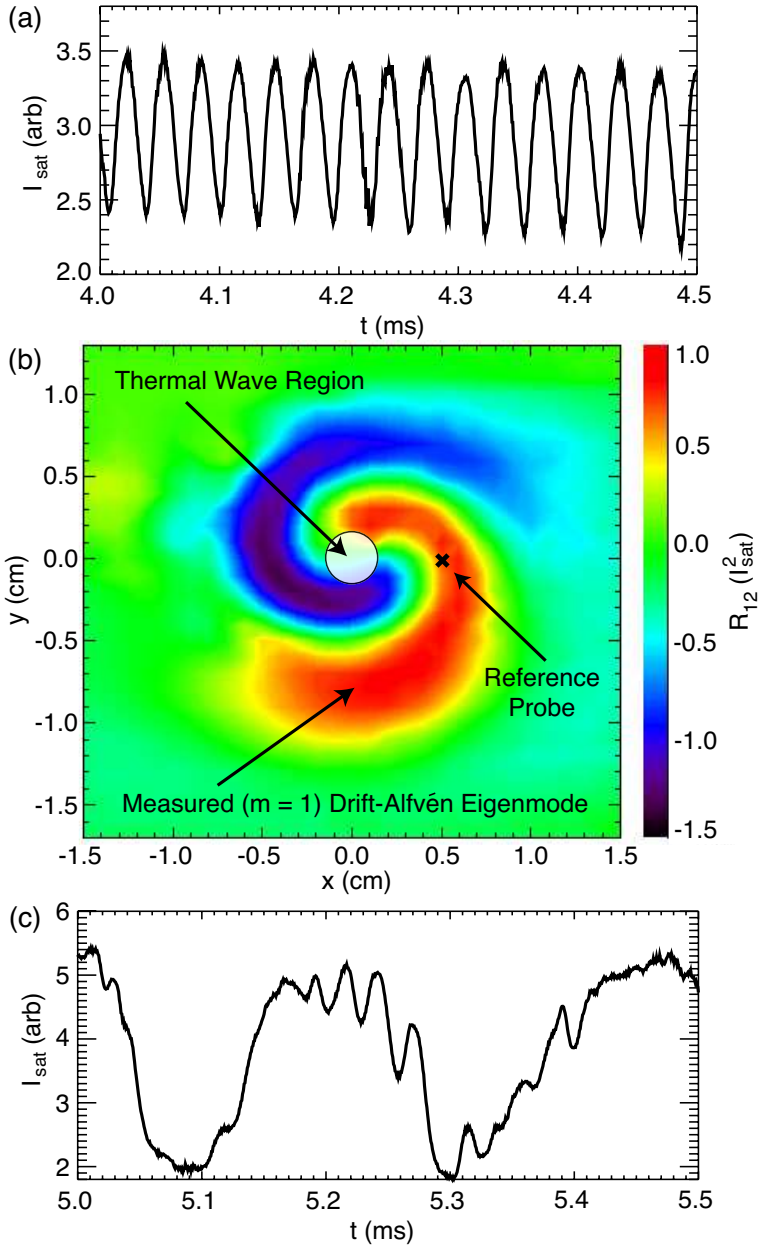

Figure 2.14: Oscillations in ion saturation current due to (a) coherent drift-Alfvén mode and (c) thermal wave. (b) Two-dimensional contour of the cross-covariance, R_{12}, between two probes with axial separation $\Delta z = 160$ cm.

Finally, at the latest times of the beam heating, $8 \leq t \leq 10$ ms, the fluctuations become turbulent and there are no observable coherent modes in the spectra. Figure 2.13 illustrates that the amplitude of these fluctuations is large, exhibiting $\delta T_e/T_e \approx 50\%$. Transport is enhanced above classical levels, or "anomalous", during this turbulent phase of the filament's evolution.

2.3.2 Spatial Behavior

Radial profiles at $z = 384$ cm are shown in Fig. 2.15. Panel (a) presents a profile at $t = 3.0$ ms during the classical transport stage. Within only 0.5 cm the filament has nearly reached a uniform temperature. Panel (b) is a two-dimensional contour of I_{sat} that highlights the symmetric nature of the filament. This result is taken from $t = 1.0$ ms, also during the classical transport stage. Comparisons between the radial profiles during classical and anomalous transport regimes elucidate the difference between classical and anomalous thermal transport.

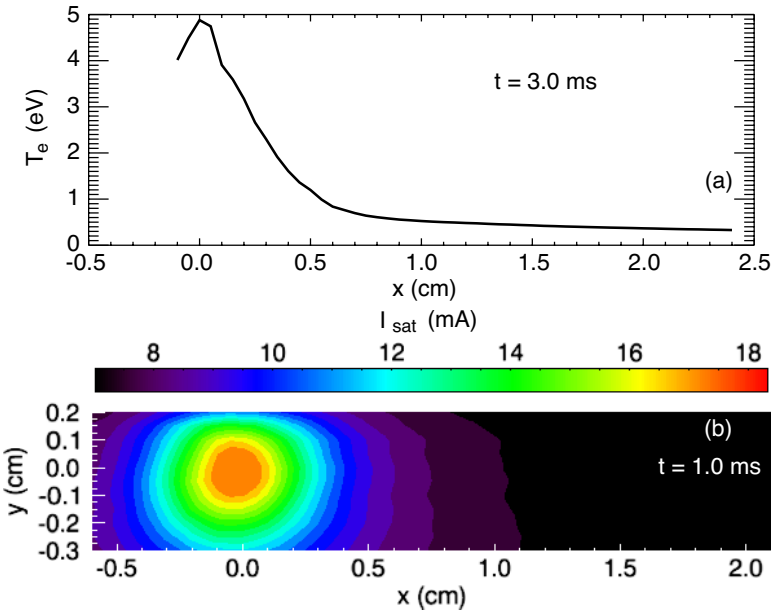

Figure 2.15: $z = 384$ cm (a) Radial temperature profile of the filament at $t = 3.0$ ms. (b) Two-dimensional contour of I_{sat} illustrating the symmetric nature of the filament during early times.

The radial symmetry shown in Fig. 2.15 is observed at all axial positions. This regularity during the early time evolution of the filament allows for the summary drawing given in Fig. 2.16. In this figure, a mapping of fluctuation behavior is given in terms of a typical radial temperature profile. The LaB_6 crystal is shown for perspective. The thermal wave is strictly confined to the center of the filament, though it does overlap with the global structure of the drift-Alfvén eigenmode. In Fig. 2.16 the gradient region is labeled as the location of the drift-Alfvén wave because that is where it exhibits its largest amplitude.

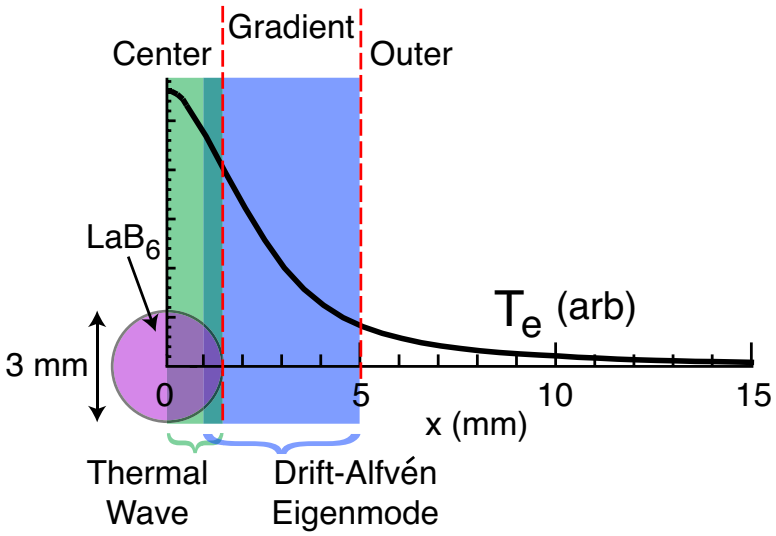

Figure 2.16: Diagram highlighting the different spatial regimes in the radial profile of temperature. The thermal wave is confined to the center of the filament while the drift-Alfvén eigenmode is an extended structure. The drift-Alfvén mode exists as a global feature, but its amplitude peaks in the gradient region.

2.3.3 Spatiotemporal Evolution

Figure 2.17 illustrates the marked difference in the filament profile before and after the transition to anomalous transport. In panel (a) a cylindrically symmetric profile is observed at $t = 1$ ms. Well after the transition away from this classical regime, panel (b) presents the resulting profile at a time of $t = 8$ ms. Both of these contours are actually ensemble results over a few thousand discharges.

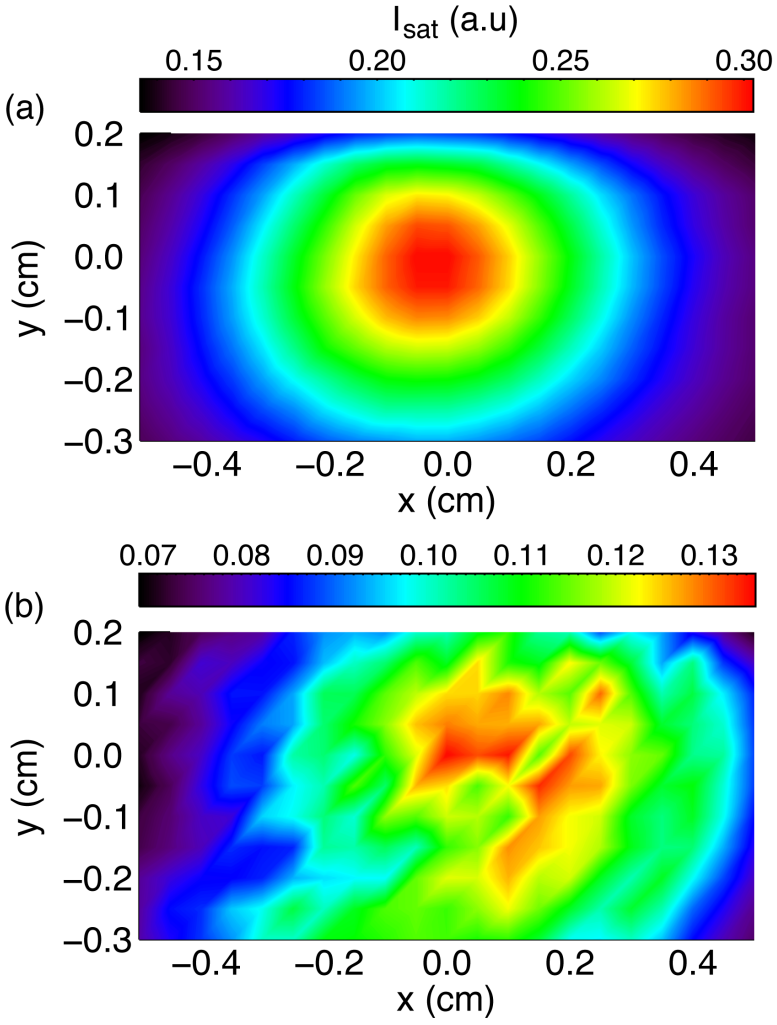

Figure 2.17: I_{sat} contours at $z = 544$ cm (a) The $t = 1.0$ ms time is the standard used to experimentally determine the filament center. (f) At $t = 8$ ms the filament has transitioned to a turbulent state in which both classical transport and cylindrical symmetry are no longer present.

2.4 Relationships Between Physics Results and Filament Behavior

2.4.1 Thermal Waves Appear in the Filament Center

The thermal waves discussed in Chapter 3 are only observed in the radial center of the filament. This is a result required by the nature of thermal waves because their drive source must be a heating source. While presently unknown, the heating source for the thermal waves must reside within the filament because the only energy source for all heating is the beam itself (the thermal wave may be excited by a heat source located axially away from the beam and does not have to be driven by the beam directly). Thermal waves are observed to initially appear at different times in the filament's evolution.

2.4.2 Exponential Spectra Occur in the Anomalous Transport Regime

The Lorentzian pulses and the resulting exponential spectra of Chapter 4 are observed at all spatial locations, but only late in time after the transition from classical to anomalous transport has occurred. This turbulent behavior is observed in many plasma devices, in all cases it appears driven by the pressure gradients existing in plasma boundaries (e.g., tokamak scrape-off layers and edge regions of linear devices).

CHAPTER 3

Identification of a Spontaneous Thermal Wave

In recent years the venerable topic of thermal (diffusion) waves [Ångström, 1862] has received increased attention [Mandelis, 2000], primarily in the context of modern methodologies for diagnosing the properties of condensed and gaseous matter. Advances in experimental techniques and in the understanding of the mathematical properties of diffusion equations driven by sinusoidally, time-varying sources have resulted in the concept of thermal-wave resonators [Shen and Mandelis, 1995]. The frequency dependence of driven resonators is currently used to measure the properties of liquids [Balderas-López et al., 2000], gases [Bertolotti et al., 1998] and liquid-gas mixtures [Azmi et al., 2005]. Although thermal waves have not been as extensively studied in the plasma state [Gentle, 1988; Jacchia et al., 1991], some of their features have been effectively used to deduce subtle issues of the anomalous cross-field transport in tokamak devices [Mantica et al., 2006; Casati et al., 2007]. A complexity of thermal waves in magnetized plasmas is that the thermal conductivity along the magnetic field, $\kappa_{\|}$, is several orders of magnitude larger than across, $\kappa_{\perp}$. In addition, the numerical value of $\kappa_{\|}$ can be quite large. This makes the study of thermal waves in plasmas considerably more difficult than in the undergraduate "Angstrom modulation" experiment [Bryant, 1963]. The plasma systems must accommodate a long, and spatially isolated, heated region whose length along the magnetic field is much larger than the cross-field dimension. The configuration of this thesis experiment provides an

environment akin to the thermal-resonators developed for other states of matter, but, in addition, the free energy available is found to spontaneously generate a highly-coherent thermal resonant cavity mode. A coherent mode of frequency lower than the drift-Alfvén mode frequency has been observed in previous work within this geometry, see Section IV of Burke et al. [2000a]. The identification of this mode as a thermal wave is presented in this Chapter.

3.1 Observations of a Thermal Wave

Figure 3.1 is a power spectrum averaged over the entire heating period of all of the shots acquired in the center of the filament. One of these shots was previously plotted in Fig. 2.13. From the power spectrum it is possible to identify multiple distinct modes. The broad peak just below 50 kHz represents the drift-Alfvén mode (an $m = 1$ eigenmode as shown in Fig. 2.14b). In this case, the peak is broadened due to the time averaging of the spectral analysis across the frequency evolution of the mode. Several harmonics of this wave are also identified in the plot. The thermal wave peak is identified near $f = 5$ kHz.

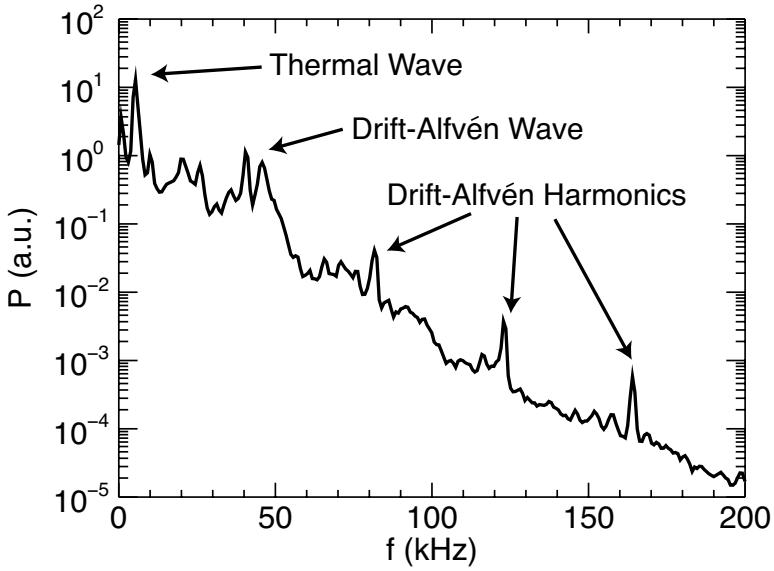

Figure 3.1: Power spectrum of electron temperature measurements averaged over the entire heating period and all shots acquired at the filament center. The axial position is $z = 384$ cm. The thermal wave is the largest amplitude oscillation, though some power from the drift-Alfvén mode and its harmonics is present.

Figure 3.2 illustrates the nature of the temperature fluctuations that correspond to the thermal wave. Coherent low frequency (< 10 kHz) oscillations are seen from $1 \leq t \leq 3$ ms in the measured trace. It is important to note that during this time there are no oscillations in the injected current of the electron beam as shown in the bottom trace. The agreement between the mean measured electron temperature and that of the theoretical model shows that heat transport remains classical during observations of the thermal wave that occur early in the filament evolution.

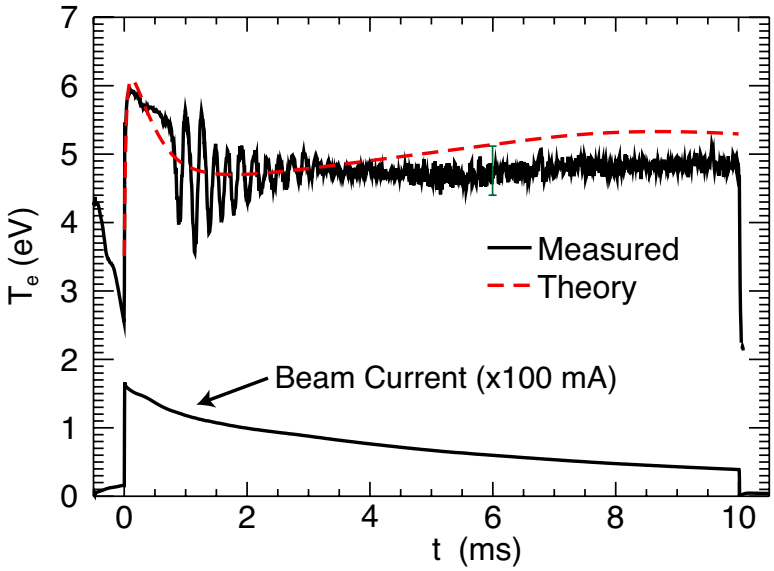

Figure 3.2: The top traces are the measured (solid black) and theoretical (dashed red) results for the electron temperature at an axial distance of $z = 224$ cm at the center of the filament. An error bar (solid dark green) is placed at $t = 6$ ms and represents the typical error across all the measurements. No oscillations are included in the theory trace, which represents classical heat transport. The bottom trace is the injected current of the electron beam.

Figure 3.3 shows thermal wave oscillations observed well beyond the $t = 3$ ms point of Fig. 3.2. The current collected by the probe, I_{probe}, is plotted for the fixed probe bias value of $V_{\text{probe}} \approx -40$ V. The amplitude of the low frequency mode decreases in time, but is still visible beyond the 4 ms mark. The decay of this trace is once again due to the background density decay of the afterglow plasma. Panel (a) presents the entire time series while panel (b) is a zoomed in view highlighting the oscillations within the $2 \leq t \leq 6$ ms range. The data has also been digitally low-pass filtered at 20 kHz for the presentation in (b).

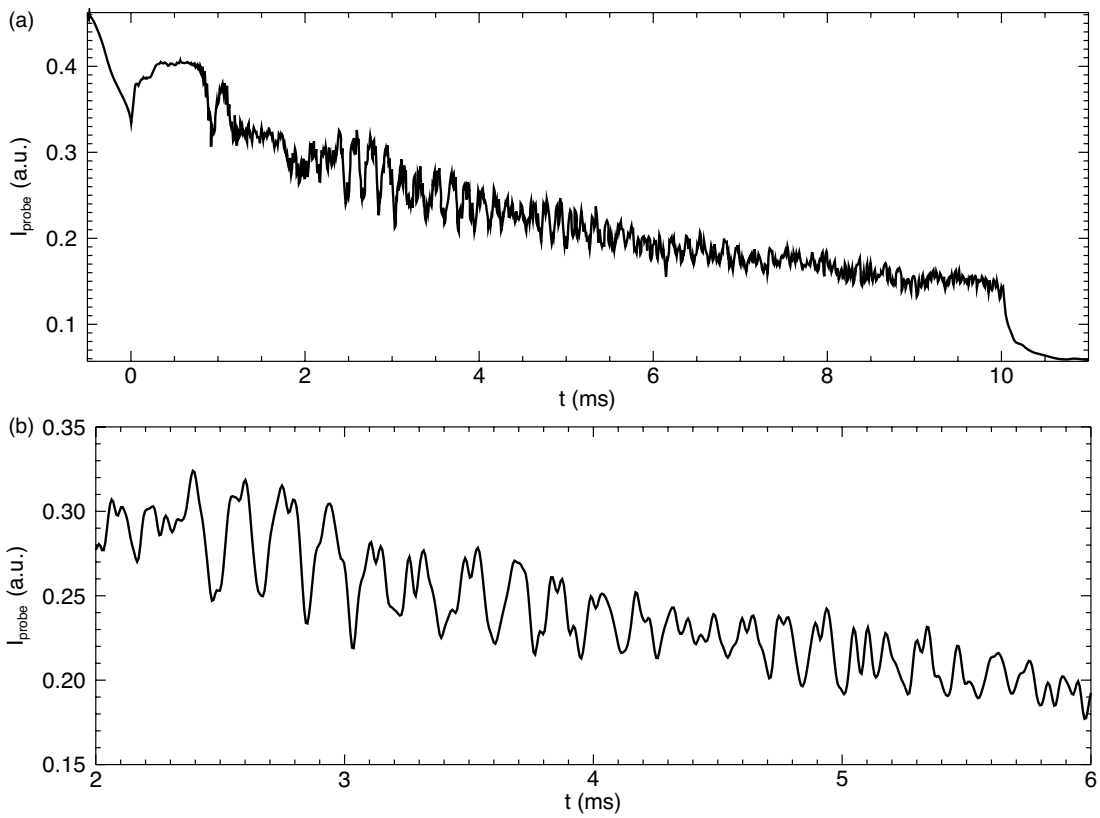

Figure 3.3: Time series of current collected by the biased probe for a fixed value of the bias. (a) Full time series without filtering. (b) Narrow time series that has been low-pass filtered at 20 kHz and then minimally smoothed for plotting.

3.2 Theory

Thermal waves were first detailed by Ångström over one hundred years ago [Ångström, 1862]. Ångström solved the equations for diffusive heat transport in scalar media and obtained the dispersion relation of the thermal wave, the propagation of heat fronts through materials. They are studied in undergraduate physics labs [Bryant, 1963]. Students apply and remove a heat source (blow torch)

to one end of a metallic rod and then record the temperature along the rod as a function of time. The period and wavelength calculated from these measurements allow for the determination of the thermal conductivity of the metal. Advanced applications of this method allow for the measurement of material properties in liquids [Balderas-López et al., 2000], gases [Bertolotti et al., 1998], and liquid-gas mixtures [Azmi et al., 2005]. A similar result is obtained for the plasma experiment and motivates the design of diagnostics that utilize thermal wave properties to measure plasma thermal conductivities.

The dispersion relation of a thermal wave in a magnetized plasma is more involved than that of other media because the confining magnetic field breaks spatial symmetry. Furthermore, the thermal conductivity of the plasma parallel to the magnetic field, $\kappa_{\parallel}$, is orders of magnitude larger than that across the field, $\kappa_{\perp}$, which constrains the experimental geometry capable of studying these waves. The large difference in thermal conductivities requires that the plasma device be capable of containing a plasma structure that is approximately 900 times longer along the magnetic field than it is across. The heated filament in this experiment can serve as a resonant cavity for the thermal wave due to its extended axial geometry and the sharp boundaries resulting from the difference in thermal conductivity between the heated filamentary plasma and the cold background plasma.

The heat diffusion equation in this case is,

$$\frac{3}{2}n\frac{\partial}{\partial t}T_{\mathrm{e}} - \vec{\nabla}\cdot\left(\overleftrightarrow{\kappa}\cdot\vec{\nabla}T_{\mathrm{e}}\right) \;=\; Q\left(\vec{r}\right)e^{-i\omega t}\,, \tag{3.1}$$

where $\overleftrightarrow{\kappa}$ is the thermal conductivity tensor and $Q\left(\vec{r}\right)$ is the heat source. Linearizing this expression allows for the determination of the complex wave numbers,

$$k_{\parallel} = (1+i)\sqrt{\frac{3\omega n}{4\kappa_{\parallel}}} \qquad , \qquad k_{\perp} = (1+i)\sqrt{\frac{3\omega n}{4\kappa_{\perp}}}\,, \tag{3.2}$$

where the thermal conductivities are given by,

$$\kappa_{\parallel} = \frac{3.2 n T_{\mathrm{e}} \tau_{\mathrm{e}}}{m_{\mathrm{e}}} \quad , \quad \kappa_{\perp} = \frac{1.47 \kappa_{\parallel}}{\omega_{\mathrm{ce}}^2 \tau_{\mathrm{e}}^2} \ . \tag{3.3}$$

In Eq. (3.3), m_{e} is the mass of an electron, ω_{ce} is the electron cyclotron frequency, and τ_{e} is the electron collision period. The electron collision period is given by $\tau_{\mathrm{e}} = 3.44 \times 10^5 T_e^{3/2}/(n\lambda)$, where λ is the Coulomb logarithm. These relations allow for the calculation of the electron collision frequency of the plasma to be calculated from the measured wave numbers of the thermal wave.

The finite length of the temperature filament, coupled with the high parallel thermal conductivity of the plasma, results in an environment akin to the thermal wave resonators mentioned in the beginning of this Chapter. As such, it is possible to leverage the properties of the thermal wave resonator to further study the filament. One particular advantage of this situation is that the quarter-wavelength cavity condition provides a new avenue through which to study the axial length of the filament.

Theoretical work regarding the axial properties of this system indicates that the quarter-wavelength condition is met [Shi, 2008]. Figure 3.4 compares the axial temperature profile from the model with the theoretical phase results. The condition of phase $\theta = \pi/2$ corresponds to the quarter-wavelength cavity length. Axial temperature profiles are taken from the model because time constraints in experimental runs prevent a detailed measurement. The model is known to be accurate during the regime of classical transport, so its usage is warranted in this situation.

Figure 3.4 shows that the cavity condition is met for a filament length of less than nine meters. Such a length is in agreement with exploratory measurements taken during the setup of experiments. More importantly, this length fits within the LAPD-U.

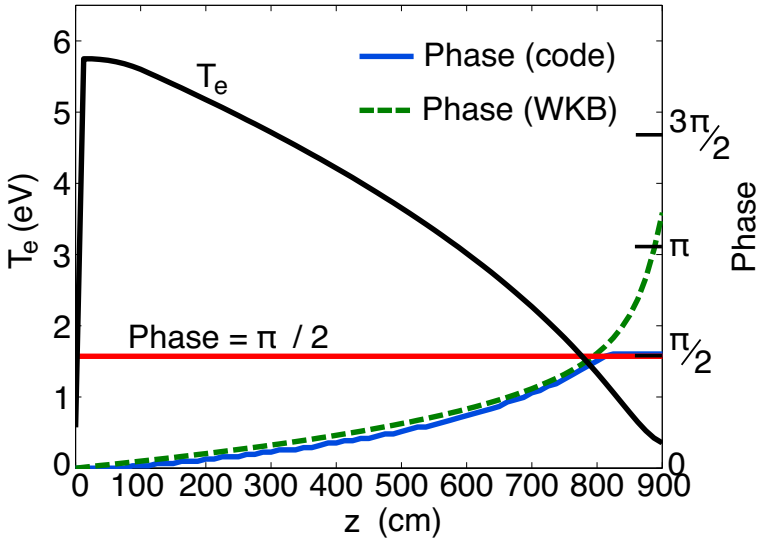

Figure 3.4: Axial dependence of T_e (solid black) compared to predictions of the cavity length necessary to sustain the thermal wave as a resonant mode. The code phase (solid blue) is taken from the model of a thermal wave with $f = 5.1$ kHz. The WKB phase (dashed green) is the Wentzel-Kramers-Brillouin phase determined from (3.2). The horizontal (solid red) line represents a phase value of $\pi/2$ and its intersection with the other curves is the length at which the quarter-wavelength resonance condition is met.

While measurements of the axial temperature profiles and the axial dependence of thermal wave fluctuation power are not possible in this instance, further theoretical development allows for a prediction of the cavity length based on the frequency of oscillations. Combining the quarter-wave resonator requirement with (3.2) leads to a relationship between the length of the cavity, L, and the resonant frequency of the thermal wave, f_R,

$$f_R = \frac{\pi \kappa_\parallel}{6nL^2} . \tag{3.4}$$

Equation (3.4) is solved using the measured plasma parameters to calculate

$\kappa_\parallel$. The result is $L = 940$ cm, in agreement with the result of Fig. 3.4. Some discrepancy between the values is expected since the background plasma density decays during the experiment and causes the temperature filament to evolve in size. The thermal wave frequency evolves in time, a result that is shown in Fig. 3.5.

The changing thermal wave frequency is illustrated by Fig. 3.5. The figure presents a close-up view of the coherent oscillations visible in Fig. 3.2. The measured trace (solid black) exhibits a slippage in phase difference compared to a fixed frequency model (dashed red). In this instance, the model is a simple, sinusoidal temperature oscillation source ($Q_\mathrm{b} \propto \sin(\omega t)$ in Eq. 2.6), i.e., it is not self-consistent and cannot predict a spontaneous wave. As mentioned previously, there is a constant decay in the background plasma density that is part of the normal evolution of the LAPD-U afterglow. Manual determination of the frequency (measuring the period of individual oscillations) shows that the highest value of 5.2 kHz occurs early in the signal and then the frequency decreases until it reaches 3.9 kHz. From the inversely proportional relationship between thermal wave frequency and the filament length given in (3.4), the behavior in Fig. 3.5 suggests that the filament length increases as time progresses.

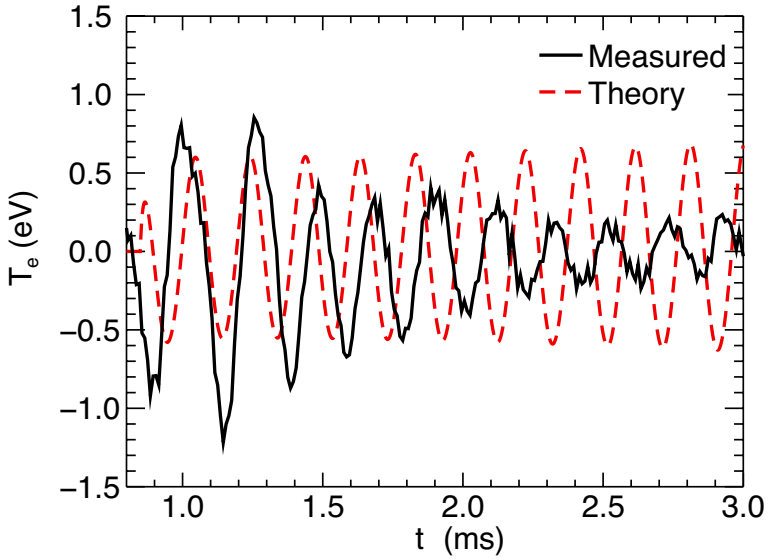

Figure 3.5: Zoomed in view of oscillations due to the thermal wave as shown in Fig. 3.2. The measured (solid black) result shows a frequency change over time as the phase is observed to deviate from the fixed frequency wave utilized in the model (dashed red).

3.3 Calculating Electron Collision Frequency based on Thermal Wave Properties

The electron collision frequency is related to the wave numbers of the thermal wave according the following expression derived from (3.2),

$$\frac{\mathrm{Im}\,(k_\perp)}{\mathrm{Re}\,(k_\parallel)} \;=\; \sqrt{\frac{\kappa_\parallel}{\kappa_\perp}} \;=\; \frac{\Omega_\mathrm{e}\tau_\mathrm{e}}{1.21}\,, \tag{3.5}$$

where Im and Re represent the imaginary and real parts of their arguments, respectively. The imaginary part of the perpendicular wave number is calculated using the measured radial decay length. The real part of the parallel wave number is calculated from the measured parallel phase velocity. The electron

gyrofrequency is set by the applied magnetic field, leaving the electron collision time as the only undetermined variable.

The radial decay length is related to the imaginary part of the perpendicular wave number, $\mathrm{Im}(k_\perp)$, by the expression,

$$\delta_r \;=\; \frac{1}{\mathrm{Im}\,(k_\perp)}\;. \tag{3.6}$$

Figure 3.6 plots the radial profiles of the filament temperature and the amplitude of the thermal wave fluctuations. The amplitude is calculated by integrating the power in the T_e time signal over the frequency range $f = 3.7{-}6$ kHz. The thermal wave is contained within a narrow region of the filament and its measured radial decay length is $\delta_r = 1$ mm. Since the diameter of the probe is also 1 mm, this can be considered to be the smallest possible decay length that can be measured. Useful information is obtained because the theoretical model (dashed red curve in Fig. 3.6) predicts a decay length of $\delta_\mathrm{th} = 0.9$ mm and the measurement confirms the actual decay length cannot be much larger that prediction. The upper bound provided by the measurement of the decay rate translates into a lower bound for the imaginary part of the perpendicular wave number.

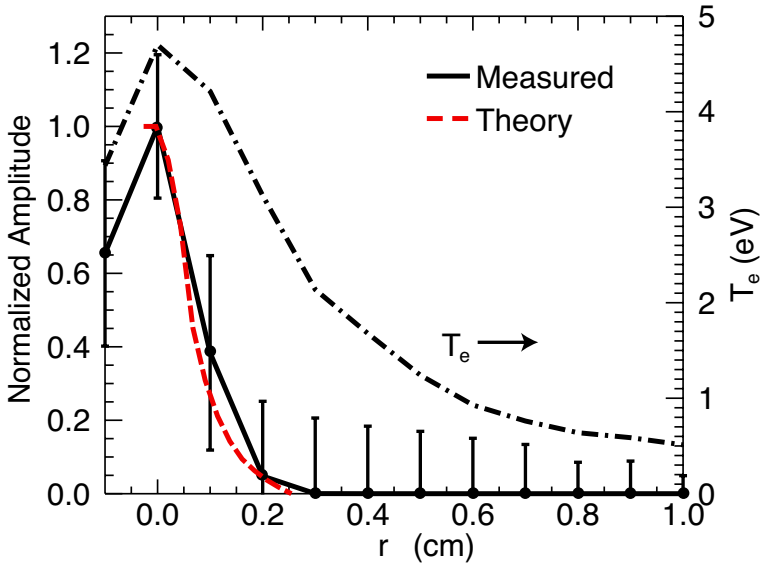

Figure 3.6: Top curve (dash-dot black) is a radial profile of the electron temperature at axial position $z = 544$ cm. The other curves represent the radial extent of the thermal wave fluctuations. The normalized amplitude of T_e fluctuations (solid black) at $z = 544$ cm is the integrated value over the frequency range $f = 3.7 - 6$ kHz. The theoretical result (dashed red) is the amplitude as generated by the theoretical model.

The real part of the parallel wave number is related to the parallel phase velocity, $v_\parallel$, through the expression $\omega/k_\parallel = v_\parallel$. The angular frequency is known from the time series. The power spectrum of the T_e signal peaks at $f = 5.1$ kHz in this case. Parallel phase velocity is measured using a cross-spectral technique.

Two probes are placed axially apart a distance of $\Delta z = 384$ cm. One probe is fixed at $r \approx 0.15$ cm to ensure that it observes low frequency oscillations due to the thermal wave. This probe cannot be placed at the direct center of the filament because it will perturb the system and reduce the accuracy of the measurement. When placed at the center of the filament, even a small probe tip may serve as a

physical barrier that sets the axial length of the filament. Since the filament acts as a resonant cavity for the thermal wave, forcibly altering its dimensions will either change or eliminate the wave. The second probe acquires data at every point throughout a two-dimensional plane. The cross-phase, Θ, between these signals is calculated for the thermal wave frequency [Bendat and Piersol, 2000] when the second probe is positioned at the center. From the cross-phase the time delay between the signals, Δt, is given by $\Delta t = \Theta/2\pi f$. This time delay, coupled with the distance between the probes allows for the calculation of the parallel phase velocity, $v_{\parallel} = \Delta z/\Delta t$.

The measured phase velocity is $v_{\parallel} = 1.9 \times 10^7$ cm/s. Comparison with the result from the theoretical model, $v_{\parallel,\mathrm{th}} = 2.2 \times 10^7$ cm/s shows excellent agreement.

Equation (3.5) can now be solved for the electron collision time. The result is $\tau_\mathrm{e} = 5.93 \times 10^{-7}$ s. Using standard parameters of the filamentary plasma ($T_\mathrm{e} = 5$ eV, $n = 10^{12}$ cm^{-3}, $\lambda = 10$) leads to a value of $\tau_\mathrm{e} = 3.87 \times 10^{-7}$ s. The values are comparable and suggest that a diagnostic based on driven thermal wave oscillations can provide a measurement of electron collision frequency.

3.4 Summary

Thermal waves are commonly studied in non-plasma states of matter. Driven thermal waves allow for the precise calculation of the thermal conductivity of a material. Magnetized plasmas are a more difficult medium in which to observe these waves due to the large difference in thermal conductivity along the magnetic field compared to that across it. The extended geometry of the temperature filament provides an excellent environment for studying these waves because it

develops into a resonance cavity in which a thermal wave is spontaneously generated.

Throughout the experiments performed with the filamentary geometry, low-frequency oscillations that do not correspond to drift-Alfvén behavior have been observed. These are oscillations in electron temperature and are not directly driven by similar oscillations in the beam heating. The drive mechanism remains to be determined. Consideration of the resulting wave as part of a thermal wave resonance cavity allows for the calculation of the filament length based on measurements of the wave's frequency. This result is in agreement with direct measurements near the axial end of the filament.

Furthermore, the properties of the thermal wave are set by the thermal conductivity of the plasma. Measurements of the parallel and perpendicular wave vectors provide for an additional calculation of the thermal conductivity, which is presented here as the calculated electron collision period.

These large amplitude fluctuations of the thermal wave modulate the drift-Alfvén eigenmodes that are generated by the pressure gradient of the filament. It is useful to study the behavior of the thermal wave in order to determine its complete role in the turbulence resulting from drift-Alfvén interactions, which is the subject of the following Chapter.

CHAPTER 4

Exponential Frequency Spectrum and Lorentzian Pulses

During the early evolution of the temperature filament a pressure gradient forms in response to input heating from an electron beam. At these early times, the transport of thermal energy is observed to be in agreement with classical theory. This Chapter is concerned with the behavior of the system once this classical regime is ended. The transition into an enhanced, or anomalous, transport regime, and away from the classical regime, was shown in Fig. 1.3. That spectrogram clearly indicates a stark difference in the power spectra of each regime. Investigation into the character of the enhanced transport spectra finds that these spectra feature an exponential dependence in frequency. Review of the measured signals finds that the exponential spectra are only observed during times when solitary pulses are present. The pulses are of Lorentzian shape, which allows for an analytic relationship between them and the exponential spectra. Reports of exponential power spectra from other laboratory plasma devices suggests that the existence of exponential power spectra due to Lorentzian pulses in time series measurements is a universal feature of plasma turbulence, with direct relation to anomalous transport.

4.1 Observations of Exponential Spectra and Pulse Structures

A single trace of electron temperature is presented in Fig. 4.1. Panel (a) is the complete time series acquired at $(r, z) = (0.8, 384)$ cm while panel (b) focuses on the time region in which fluctuation activity is observed. This is the same data set as the measurement shown in Fig. 2.13. The radial position is in the outer region (as defined in Fig. 2.16). The semi-transparent, colored rectangles are used to indicate the windows used for the calculation of FFT power spectra to be shown in the following figure. Time labels within the rectangles indicate the central time of the FFT window.

Figure 4.1a illustrates that little thermal energy reaches this outer radial position. The temperature is nearly the same as for the unheated afterglow plasma. A brief temperature increase is noted at $t = 0.55$ ms, though the only noticeable effects occur after 6 ms. Panel (b) provides a perspective for these later time fluctuations. The first set of fluctuations corresponds to the coherent drift-Alfvén mode. These oscillations are dominant until approximately $t = 8.8$ ms, at which time the fluctuations become turbulent and no coherent mode is observed. Even with a lack of coherent modes, there are solitary structures, or pulses, evident in the time series. One large amplitude event occurs at $t = 9.82$ ms in Fig. 4.1b.

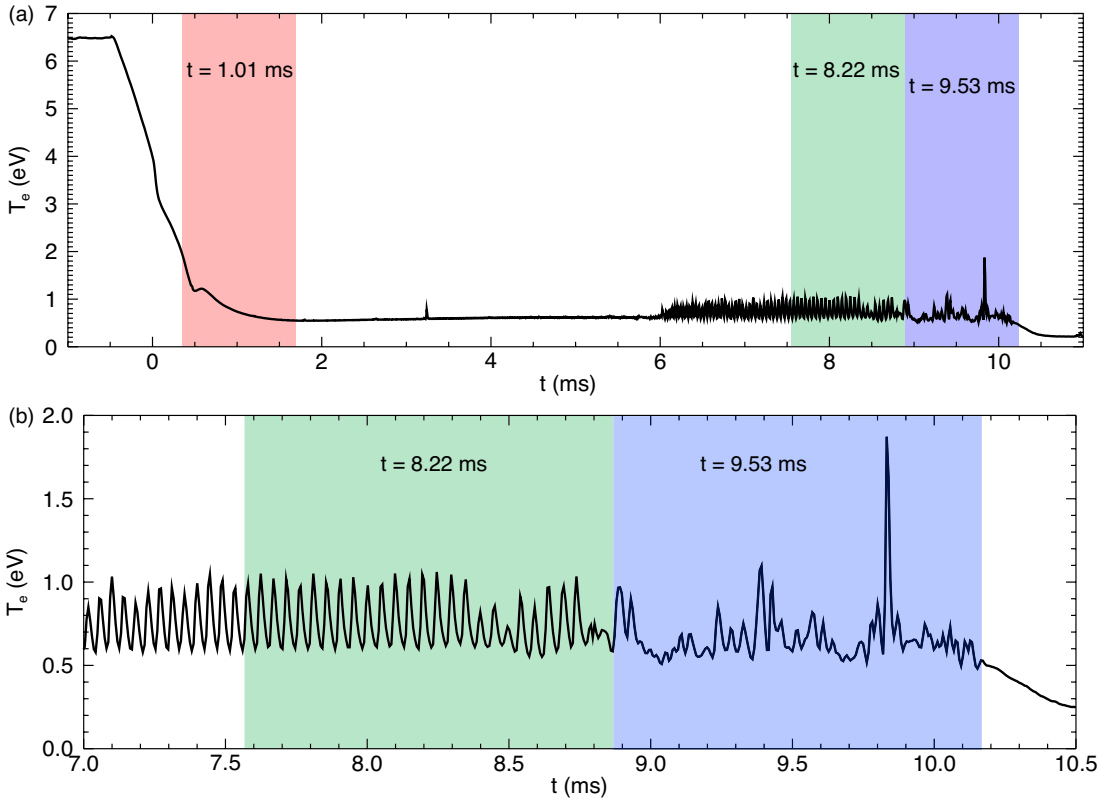

Figure 4.1: Electron temperature time series at $(r, z) = (0.8, 384)$ cm. Semi-transparent rectangles indicate the time windows used to calculate FFT power spectra shown in Fig. 4.2. The time labels represent the center time of the FFT window. (a) Little heating reaches this outer radial position, though activity is noticeable after $t = 6$ ms. (b) Zoomed in view of the activity from (a).

Figure 4.2 plots the FFT power spectra corresponding to each of the three regions highlighted in Fig. 4.1. The spectra from the earliest time window (solid red), centered on $t = 1.01$ ms, displays no coherent modes. Above $f = 10$ kHz this spectra is below the noise level of the system. This is an expected result since the measurement shown in the previous figure suggests there are no fluctuations during this time. The spectra centered on $t = 8.22$ ms (dotted green) shows

many peaks corresponding to coherent modes. These are the drift-Alfvén mode and its harmonics. The spectra centered on $t = 9.53$ ms is completely different from the other two. In the semi-log presentation of the plot, the behavior of the 9.53 ms spectra appears linear across 20 - 100 kHz. An exponential dependence on frequency produces straight-line plots in the semi-log format. The difference between the latest time spectra, $t = 9.53$ ms, and those from the two earlier times is that it is the only one to feature an exponential character.

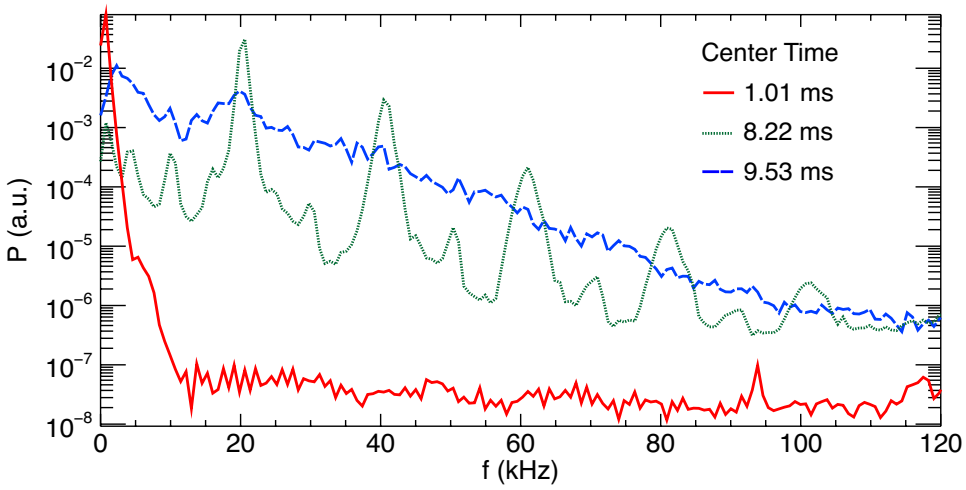

Figure 4.2: Electron temperature power spectra corresponding to the indicated regions of Fig. 4.1. While the regions are labeled on the measured trace, the FFT analysis is only performed on the fluctuating component of the time series.

Observations of exponential spectra and pulse structures are made throughout the experimental range of this system. In all cases the exponential spectra appear only during the anomalous transport phase of the experiment. This Chapter details the observations of such spectra and their related pulses. A model relating the characteristics of the pulses to the spectra is presented.

4.2 Exponential Spectra in the Temperature Filament Environment

4.2.1 Spatial Details

Exponential spectra are measured for positions within the temperature filament experiment where individual time traces display Lorentzian pulses. Figure 4.3 presents a diagram outlining where Lorentzian pulses of positive polarity are observed within the radial profile of the filament. A typical electron temperature profile (solid black) is shown to provide perspective for the three regions of unique behavior: center, gradient, and outer. The center region corresponds to the radius of the LaB_6 heating source (drawn as the purple circle in the lower-left of the figure). This region is where the thermal wave of Chapter 3 is observed. Lorentzian pulses of negative polarity, similar to the one shown in Fig. 4.11 are found exclusively within this region.

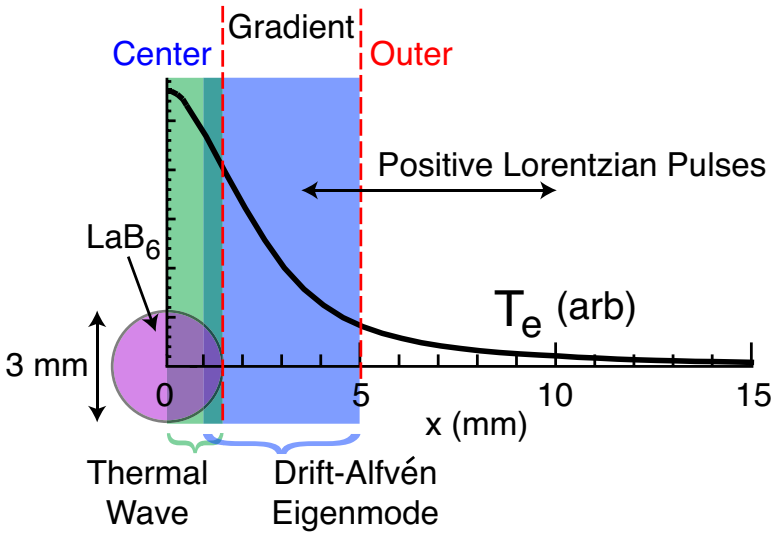

Figure 4.3: A diagram of the regions of interest within the radial temperature profile of the filament. The LaB_6 crystal is shown to provide perspective. The fluctuations in the filament can be classified according to three regions: Center, Gradient, and Outer. The thermal wave is confined to the center while the drift-Alfvén eigenmode peaks in amplitude within the gradient region. There is some overlap between these waves. Lorentzian pulses of positive polarity are primarily observed in the outer region, though some are identified within the gradient region. Negative polarity Lorentzian pulses are observed in the center region.

The gradient region is where the amplitude of the temperature gradient is largest. This results in the largest amplitude for the drift-Alfvén eigenmode. As an eigenmode, the drift-Alfvén wave extends throughout the entire radial dimension, however, the diagram of Fig. 4.3 emphasizes the location of this maximum amplitude because that is where the wave is most readily observed.

The outer region of the filament is where the more dramatic examples of Lorentzian pulses (positive polarity) are observed. As illustrated by Fig. 4.10,

the low amplitude of the filament and background plasma fluctuations allows for the easy detection of pulses with large relative amplitudes. Such pulses are measured at radial positions of $r > 0.75$ cm.

4.2.2 Temporal Details

Exponential spectra are observed at times after the filament has transitioned from a classical transport phase into an anomalous transport phase. This behavior is clearly illustrated by Fig. 4.4 in which the time evolution of the power spectra (color contour) displays a sharp transition to broadband spectra at the same time, $t \approx 5.5$ ms, as the I_{sat} signal (solid white, upper half of the contour) begins to display large amplitude pulses. The spectra are computed using the Continuous Wavelet Transform (CWT) method in order to achieve a balance between temporal and frequency resolution. A comparison between CWT and FFT methods is presented in Appendix A.

The I_{sat} trace is the fluctuating component of the raw measured signal, $\tilde{I}_{\text{sat}}$. For the "early" times prior to $t = 5.5$ ms there is a coherent drift-Alfvén wave seen as the solid band in the $25 \leq f \leq 45$ kHz range. During the time period of drift-Alfvén eigenmode activity the plasma transport is classical and agrees with the theoretical model.

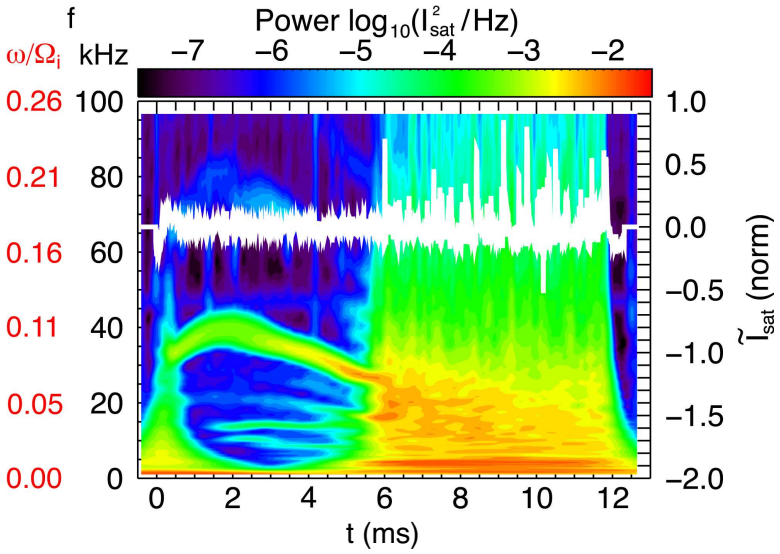

Figure 4.4: Time evolution of the power spectrum (color contour) with an overplot of the fluctuating component of an $I_{\rm sat}$ signal (solid white) from the same spatial position ($r = 9$ mm, $z = 544$ cm). Coherent fluctuations of the drift-Alfvén eigenmode are visible for $t \leq 5.5$ ms. After 5.5 ms there is a sharp transition to broadband (exponential) spectra that correlates with the appearance of Lorentzian pulses. The Lorentzian pulses are visible as the large upward-going spikes in the overplotted $\tilde{I}_{\rm sat}$ white trace.

Figure 4.5 plots two spectra that have been extracted from Fig. 4.4. The trace from the classical regime (solid black, $t = 2.21$ ms) features peaks due to the drift-Alfvén eigenmode at $f \approx 37$ and 74 kHz. At a time after the transition to anomalous transport has occurred (dashed red at $t = 10.73$ ms) there are no coherent mode peaks. This does not conclusively demonstrate that the drift-Alfvén mode has decayed, rather, it means that the amplitude of the exponential spectrum is at least as large as that of the coherent mode.

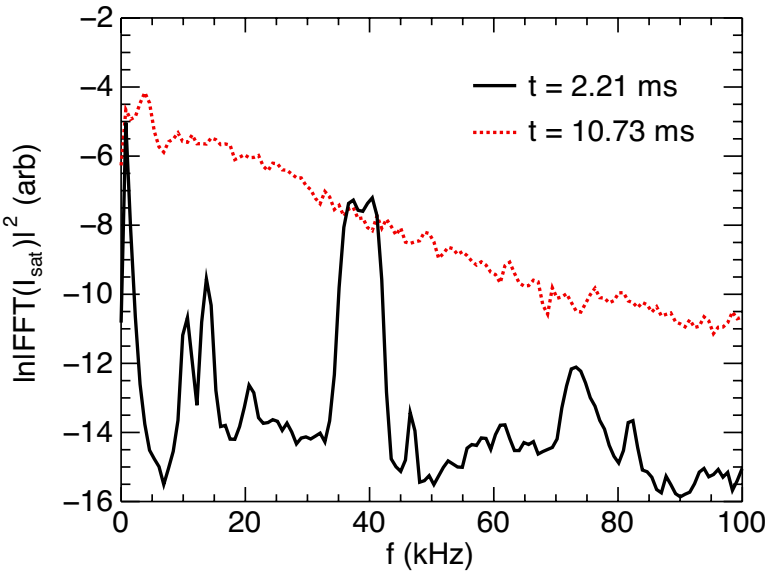

Figure 4.5: Extracted spectra from Fig. 4.4 demonstrating the character of the spectra before (solid black) and after (dotted red) the transition to anomalous transport. The amplitude of the exponential spectrum is well above the minimal levels observed for the early time trace.

4.2.3 Interaction Between Thermal Wave and Drift-Alfvén Mode

The discussion of the late-time turbulent environment of the temperature filament must include some features of the wave interactions and modulations preceding the transition to anomalous transport. It is clear that the large amplitude temperature oscillations associated with the thermal wave affect the radial temperature gradient, thereby modulating the amplitude of the drift-Alfvén mode.

4.2.3.1 Drift-Alfvén Modulation by Thermal Wave

An example of drift-Alfvén modulation by thermal wave fluctuations is observed by performing a simultaneous measurement with three probes. Each probe

measures I_{sat} at a different axial and radial location for the same plasma discharge. Two of these probes are fixed in their respective radial positions while the third probe performs a two-dimensional position scan. The scanning probe is placed at $z = 64$ cm and the fixed probes are at $(r, z) = (0.2, 224)$ cm and $(r, z) = (0.15, 448)$ cm. Perturbations of the filament by the fixed probes are minimized by placing them in nearly up-down symmetric positions opposite each other. Figure 4.6 is a contour of the I_{sat} signal measured by the scanning probe at $t = 1$ ms. The positions of the downstream probes are labeled with a dark blue "x" and text noting their axial position.

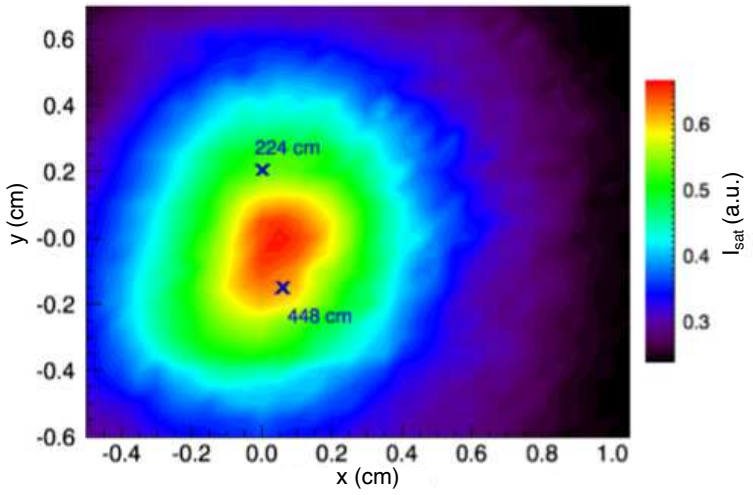

Figure 4.6: Contour of I_{sat} at $z = 64$ cm and $t = 1$ ms. Two downstream probes featuring a fixed radial position are indicated.

Figure 4.7 presents measurements from all three probes during a single shot. The scanning probe signal (black, top) is acquired at $r = 0.65$ cm, in the outer region of the filament. Both panels feature offsets in the traces that have been added to clarify the presentation. The vertical orientation of the traces are the same in each panel. Panel (a) presents the full time series for this discharge.

Panel (b) focuses on a narrow time region early in the filament evolution during which temporal correlation between the signals is apparent.

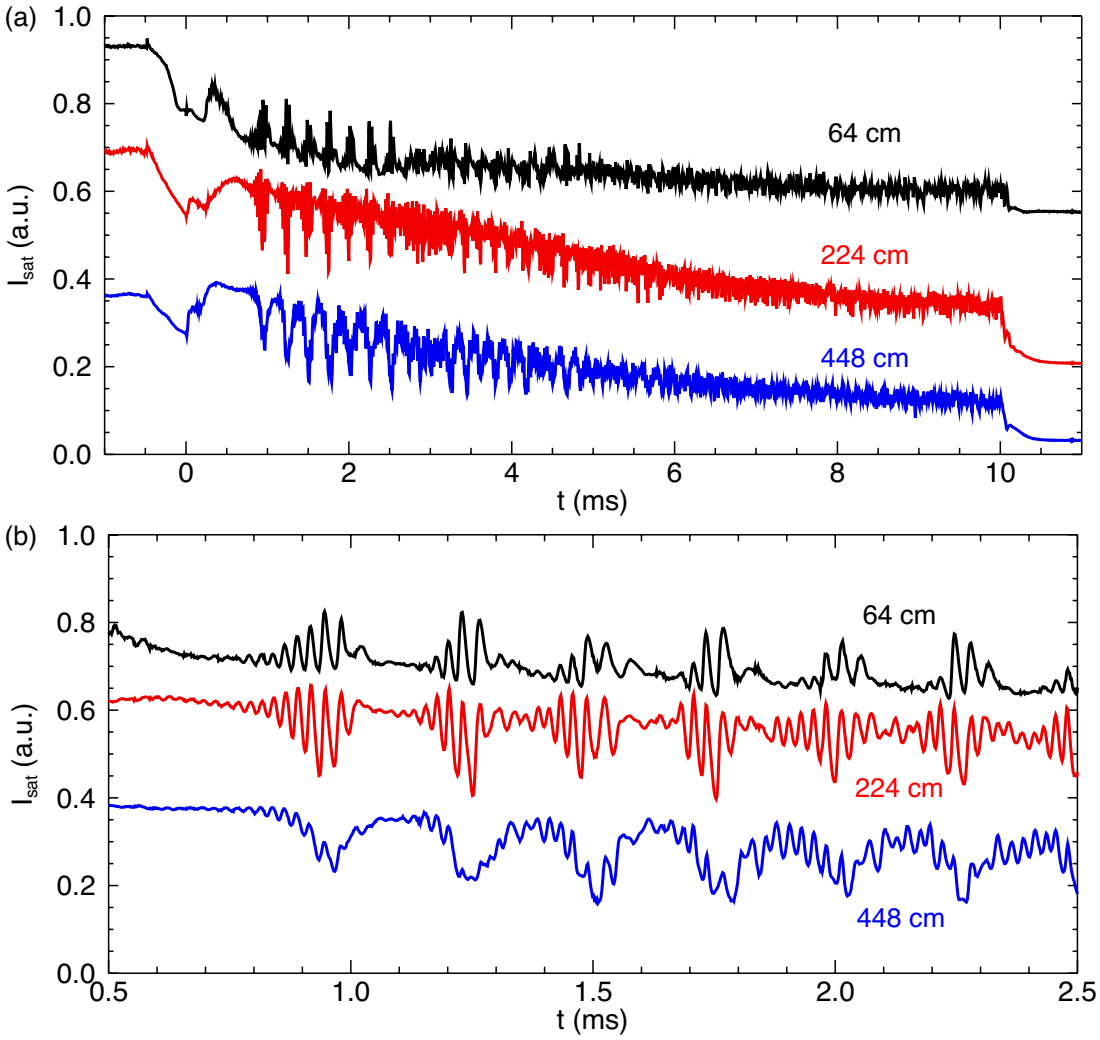

Figure 4.7: I_{sat} measurements at three different axial positions. The 64 cm measurement is acquired at a radial position of $r = 0.65$ cm, within the outer region of the filament. (a) Full time series (b) Narrow time series highlighting correlation between signals.

The $z = 448$ cm trace (blue, bottom) of Fig. 4.7 shown in panel (b) exhibits

low frequency oscillations due to the thermal wave. As expected, the trace at $z =$ 224 cm (red, center), which is only an additional 0.05 cm radially outward, does not feature these oscillations. Instead, the $z = 224$ cm trace exhibits behavior similar to wave-packet phenomena in that brief sections of coherent and growing amplitude fluctuations are observed. The first of these is found at $0.8 \leq t \leq 1.0$ ms. The trace at the $z = 64$ cm position (black, top) is also at the furthest radial position, $r = 0.65$ cm. The fluctuations in this signal appear rectified and are reminiscent of the pulses featured in Fig. 4.1.

The I_{sat} fluctuations in the 224 cm ($r = 0.2$ cm) trace of Fig. 4.7b begin to grow in amplitude as the low frequency component of the 448 cm ($r = 0.15$ cm) trace decreases. Activity is always observed on the 224 cm trace prior to observation on the 64 cm ($r = 0.65$ cm). Due to the axial separation between these probes it is not possible to conclusively determine whether these delays pertain to a radial propagation velocity. However, it is clear that thermal wave oscillations near the center of the filament are correlated to changes in amplitude of the drift-Alfvén mode in the gradient and outer regions.

4.2.3.2 Correlation Between Outer Region Pulses and Profile Relaxation

The "threshold method" of pulse identification selectively identifies events of considerably large amplitude. Details are presented in Sec. B.3. Setting the threshold value to a larger value improves the accuracy of the detection. In this section the large amplitude pulses detected on a fixed probe are used to define a "pulse time" by which the measurements of another probe are averaged. The detection of a pulse sets the condition for generating this average from the other, downstream measurement. The data first shown in Fig. B.5 is used for this

example.

Using the signal from the reference probe as a temporal trigger, a portion of the signal acquired by the moving probes is extracted. Figure 4.8 shows that a smaller number of pulses are detected in the I_{sat} signal (solid black) when the threshold level (horizontal dashed blue line) is set to 5. The peaks of these pulses are used to define a new time axis, the "pulse time" axis in which $t_{\mathrm{pulse}} = 0$ μs represents the time of a given peak's center. An array of such times are obtained. For each of these times, a portion of the signal from the other probe is considered. This segmented data represents the behavior of the plasma at this secondary position when a sufficiently large pulse is observed on the static probe.

One such time window is shown by the partially transparent green area in Fig. 4.8. The pulse peak near $t = 9.0$ ms serves as the center of the pulse time axis. A width of 100 μs is taken on each side of the center. The data falling within this time window is then extracted from the V_{f} trace acquired using the moving probe. This process is repeated for each pulse detected above the threshold value. For example, a second 200 μs series is taken from the data shown in Fig. 4.8. This series is centered on $t = 8.77$ ms. If these were the only pulses detected, then the average of these two regions would be the ensemble result for the V_{f} signal.

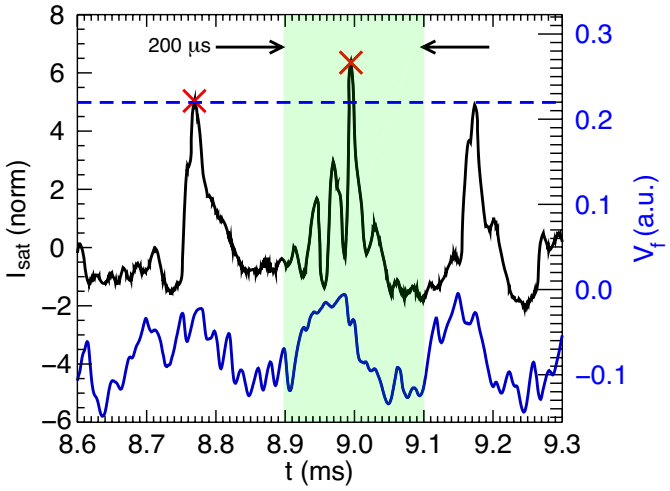

Figure 4.8: Amplitude threshold pulse detection from I_{sat} fluctuations (solid black, top trace) defines a 200 μs region from which the signal on a fixed V_{f} measurement (solid blue, bottom trace) is extracted.

The process of extracting data from the measurements of the moving probe results in a short time series for every position of the moving probe's transit. The number of records that comprise this ensemble result varies depending on the number of large pulses sampled by the fixed trigger probe. Since this probe is purposely fixed in a region known to exhibit pulses, however, the variation in the number of detected pulses is generally minimal.

Figure 4.9 illustrates the usefulness of this technique for studying profile modification. Panel (a) is a plot of radial I_{sat} profiles according to three different pulse times. The trace representing $t_{\mathrm{pulse}} = -100$ μs (black) is the ensemble profile as it appears 100 μs before the center of a pulse detected on the fixed probe. This profile matches the typical temperature filament profile observed during the classical transport stage. It is also very similar to the trace that represents $t_{\mathrm{pulse}} = 100$ μs (blue), which is the ensemble profile that is observed 100 μs after the time center

of the pulse. A major difference between these profiles and the one corresponding to $t_{\text{pulse}} = -10$ μs (red) is observed. This profile represents the ensemble result observed only 10 μs prior to the center of the pulse. It is considerably wider and features a lower amplitude than the other profiles. This difference is highlighted by the normalized representation of panel (b).

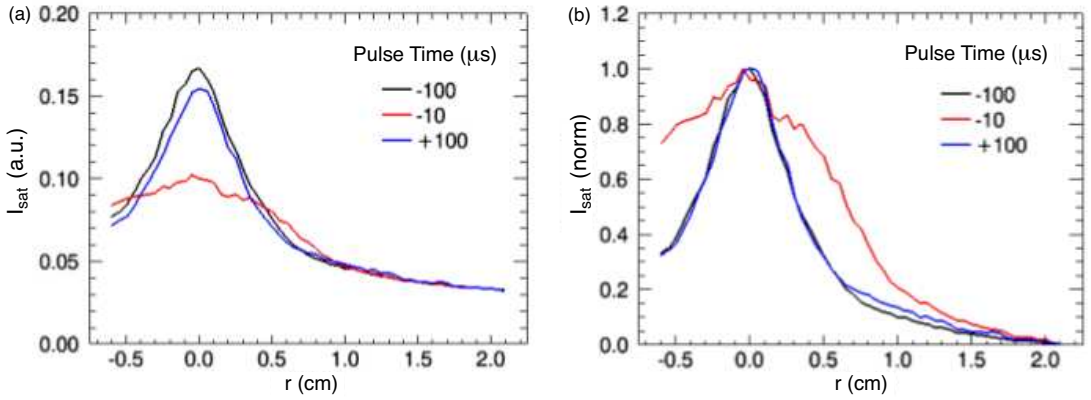

Figure 4.9: (a) Radial profiles of I_{sat} relative to the time evolution of pulses detected in the outer region of the temperature filament. (b) Normalized versions of the data presented in (a).

The profiles of Fig. 4.9 suggest that the observation of pulses in the outer region of the temperature filament is associated with considerable radial transport.

Profile modification as treated in this Section, along with coherent mode modulation as treated in Sec. 4.2.3.1, provides context for reviewing the temporal shape of the pulse events identified in the temperature filament. As shown in the following Section, the pulses in this experiment feature Lorentzian shapes. Given the strong interaction between coherent modes, coupled with the sharp transition to an anomalous transport regime, the appearance of nonlinear structures is not surprising. The relationship between these structures and the observed exponential spectra is discussed throughout the rest of this Chapter.

4.3 Lorentzian Pulses

The normalized form of a temporal Lorentzian pulse, $L(t)$, is,

$$L(t) \;=\; \frac{\tau^2}{(t-t_{\rm o})^2+\tau^2}\;, \tag{4.1}$$

where the pulse is centered at time $t_{\rm o}$ and has width τ. In (4.1), the time width is equal to one-half of the full width at half maximum (FWHM), $\tau = 1/2\,(\text{FWHM})$. This relationship is highlighted because many experimental studies of pulse-like behavior report the FWHM as the quantitative property of the events under study.

The Fourier transform of a Lorentzian pulse, $\tilde{L}(\omega)$, is given by,

$$\tilde{L}(\omega) \;=\; \pi\tau\exp\left(-\omega\tau+i\omega t_{\rm o}\right)\;. \tag{4.2}$$

The power (frequency) spectrum is given by,

$$\left|\tilde{L}(\omega)\right|^2 \;=\; \left|\tilde{L}(\omega)\tilde{L}^*(\omega)\right| \;=\; \pi^2\tau^2\exp\left(\frac{-2f}{f_{\rm s}}\right)\;, \tag{4.3}$$

where it is now possible to define $f_{\rm s} = 1/(2\pi\tau)$. This relates Lorentzian pulses to exponential spectra, it remains to find such pulses in the measured time series.

Individual pulses must be examined on a single shot basis. Due to their possibly random distribution of time centers any averaging of a data set could exhibit a strong cancellation of pulses. A further difficulty is that the pulse events can be confused with partial cycles of the drift-Alfvén waves. Any removal of the coherent drift-Alfvén mode signal from the time trace can significantly reduce the amplitude of a Lorentzian pulse present in the time trace. While several methods were employed to identify the pulses within thousands of recorded plasma discharges (see Appendix B), a relatively simple "brute force" method was found to be sufficient. By brute force, it is meant that a curve corresponding to a

Lorentzian pulse is slid through the data record. Any location that results in a good match is kept as a Lorentzian pulse. One drawback of this method is the long computing time necessary to process large data sets. A major benefit of this method is that it detects pulses without setting an amplitude threshold, thereby allowing even relatively low-amplitude events to be captured.

In this method, the functional form of a Lorentzian pulse is fit along the entire time record obtained for a single discharge. The functional form has a time width based on the input value of τ. The resulting time window is slid through the entire data record. Sections of the signal that return a good fit are kept as pulses. A good fit is defined manually after reviewing the results from a limited selection of records. The quality control factors are the standard deviation of the width and the convergence of the fit. After defining a fit pulse, several passes are made through the data set with Lorentzians of different width. In practice, due to the limited variability of the measured widths it is usually sufficient to perform the fitting once. The initial width is set by calculating the exponential decay of the power spectrum and then solving for τ.

Figure 4.10 illustrates a Lorentzian pulse featuring positive polarity. These pulses are predominantly observed in the outer regions of the filament. The background fluctuations decrease in amplitude as radial distance from the filament increases. Positive polarity pulses are often easily observed by virtue of their relatively large amplitude. Even so, the same Lorentzian fitting technique, rather than an amplitude threshold, is used to properly identify them as Lorentzian pulses.

A slight deviation from a pure Lorentzian is seen in Fig. 4.10. A modified Lorentzian pulse expression will be used in Section 4.5 to better fit this type of pulse. The following section provides a detailed analysis of pulses and spectra for

two different axial positions within the same set of plasma discharges.

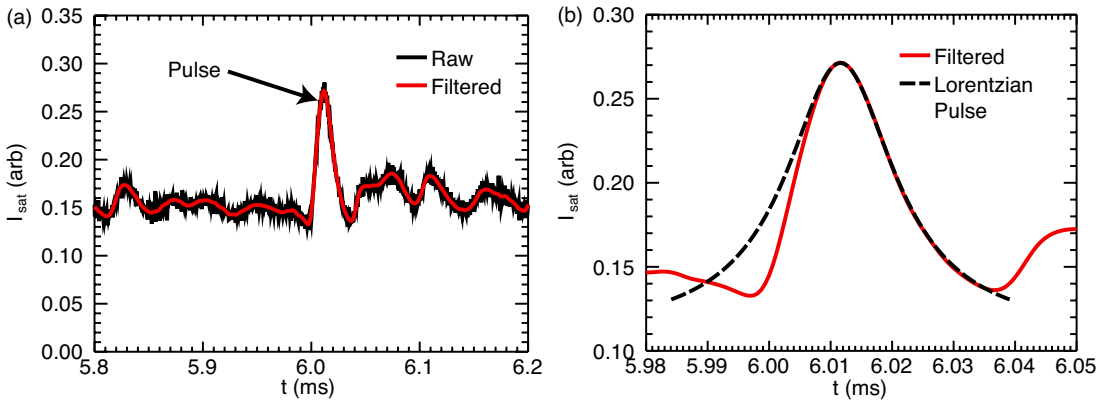

Figure 4.10: (a) Raw I_{sat} data (black) with an overlay of a low-pass filtered result (red). A Lorentzian pulse of positive polarity is indicated by an arrow. (b) Detailed view of the positive polarity pulse (solid red), with a negative polarity Lorentzian fit (dashed black).

An example of an I_{sat} pulse with negative polarity is given in Fig. 4.11. Panel (a) shows both raw I_{sat} signal (black) and a low-pass filtered trace (red). The filtering, while unable to isolate the Lorentzian features, improves the accuracy of the fitting routine by removing higher frequency (> 100 kHz) noise that can reduce the fit quality. The pulse indicated by the arrow in (a) is not particularly large amplitude. Pulses with negative polarity are observed in the center of the filament where the large amplitude thermal wave is also present. Amplitude is therefore an unreliable quantity to use as a method to search for pulses.

Figure 4.11(b) provides a closer view of the pulse event (solid red) and shows that it is well represented by a Lorentzian function (dashed black). Deviation from a pure Lorentzian is expected because the pulses are embedded in a stream of other fluctuations from both coherent modes and turbulent effects. Distortions to pulses and slight deviations from pure Lorentzians do not destroy the exponential

nature of the resulting power spectrum, as is shown in Sec. 4.5.

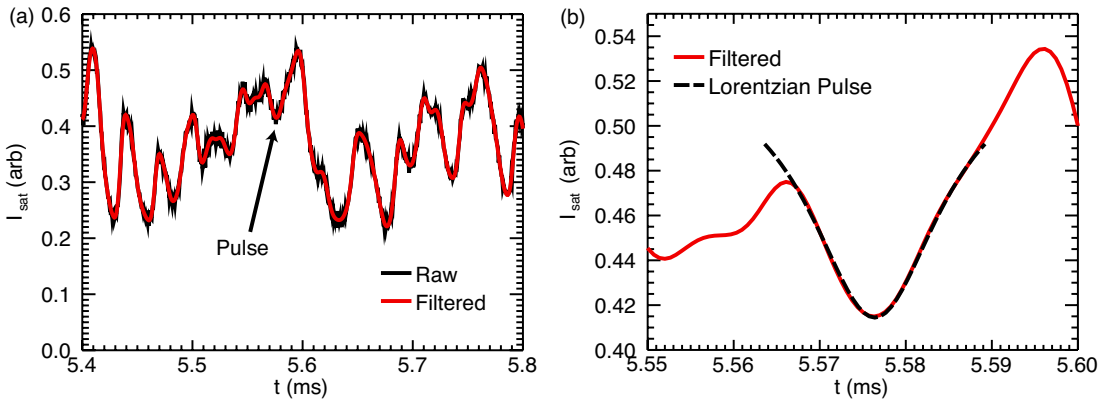

Figure 4.11: (a) Raw I_{sat} data (black) with an overlay of a low-pass filtered result (red). A Lorentzian pulse of negative polarity is indicated by an arrow. (b) Detailed view of the negative polarity pulse (solid red), with a negative polarity Lorentzian fit (dashed black).

4.4 Comparison Between Spectra and Pulses at Different Axial Positions

In this section a detailed comparison is made between pulse widths calculated from fitting power spectra and those calculated from fitting pulses directly. Figure 4.12 is a plot of the full I_{sat} time traces from the same shot within the data set examined. In this set, two Langmuir probes are placed within the outer region of the radial profile. One probe is positioned at $(r, z) = (0.7, 544)$ cm, while the other is located at $(r, z) = (0.5, 192)$ cm. At these radial positions, the transition to broadband fluctuations occurs very late in time, near $t = 11$ ms. Power spectra and pulse searches are performed over the time range $10.0 \leq t \leq 12.7$ ms. The background magnetic field is $B_{\mathrm{o}} = 1000$ G.

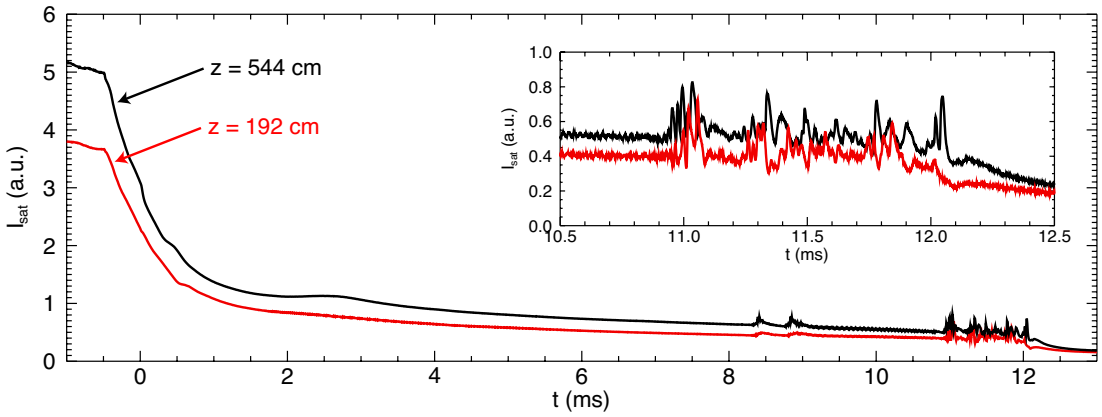

Figure 4.12: Time series of I_{sat} at two different axial positions. The radial position of the trace at $z = 544$ cm is $r = 0.7$ cm. The $z = 192$ cm is at radial position $r = 0.5$ cm.

In Fig. 4.13, pulses detected from the traces of Fig. 4.12 are identified with diamond symbols (all 20 discharges are analyzed for this study). The colors of the diamond markers are the opposite of the trace to clarify the display. The pulse detection technique (see Sec. 4.3) simultaneously identifies positive and negative-polarity pulses by allowing the free variable amplitude to be negative. Along with the positive-polarity and negative-polarity pulses, some false positives are visible within this series. A false positive is indicated by a diamond marker that appears away from an extrema of the measured signal. Ensemble pulse widths are reported with error ranges in order to accommodate the limited number of false events that may be included. Over the complete set of 20 discharges acquired there are 742 events identified at the $z = 544$ cm position, and 771 events identified at the $z = 192$ cm position.

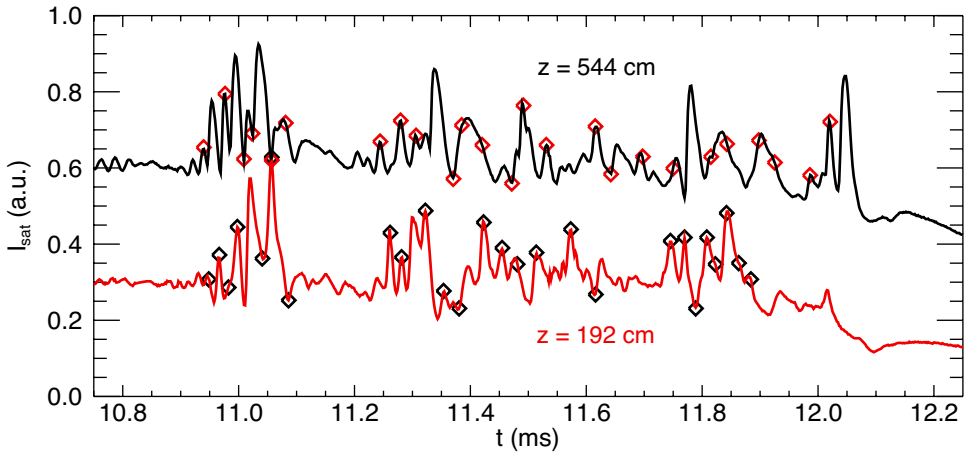

Figure 4.13: Diamond symbols mark the centers of pulses identified within the I_{sat} traces of Fig. 4.12. Black diamonds are placed on the pulses of the $z = 192$ cm (red) trace. Red diamonds identify the pulse centers of the $z = 544$ cm (black) trace. An offset has been added to clarify the display.

The characteristic time widths of the identified pulses are given in Table 4.1. The pulse width at the $z = 544$ cm position is $\tau = 8.9 \pm 2.4$ μs, slightly larger than that of the position $z = 192$ cm, which is $\tau = 7.8 \pm 2.7$ μs. The Table also includes the pulse widths as calculated from the power spectra directly, which is presented below. For both positions, the values calculated from these different methods agree to within the measurement uncertainty.

Power spectra from both axial positions are shown in Fig. 4.14 and plotted according to their natural logarithm. Panel (a) presents both spectra, showing their similarity. Panel (b) singles out the spectrum from the $z = 544$ cm position (solid black) and adds a line (dashed blue) representing the exponential fit over the frequency range $30 \leq f \leq 60$ kHz. This frequency range represents four e-foldings of the power. Spectral behavior at higher frequencies includes noise

contributions and is not included in the analysis.

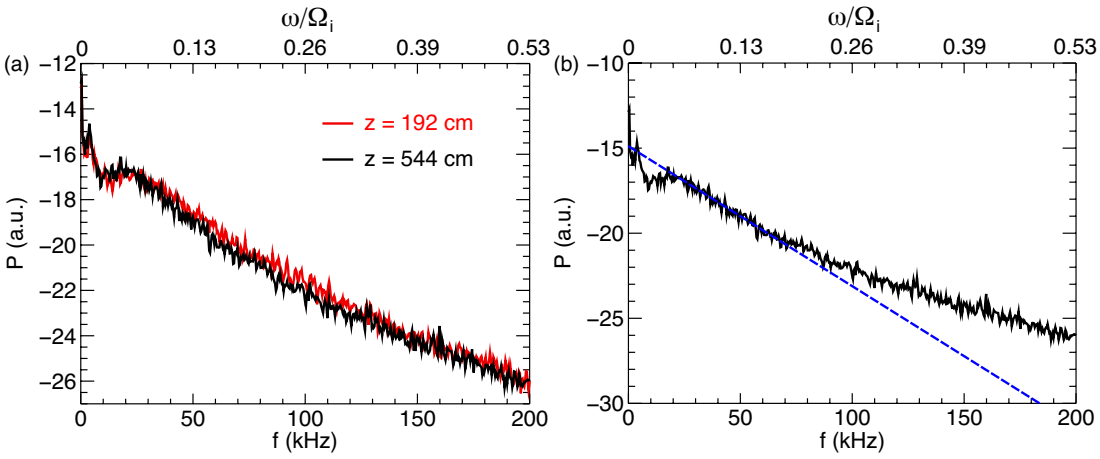

Figure 4.14: Power spectra plotted in terms of their natural logarithm. (a) Power spectra from the data set represented in Fig. 4.12. (b) Power spectra from $z = 544$ cm (solid black) with a fit to the exponential (dashed blue) calculated over the frequency range $30 \leq f \leq 60$ kHz (the peak near 5 kHz is not part of the fit).

The expected pulse time widths calculated from the power spectra are shown in Table 4.1. For the axial position of $z = 192$ cm the time width is $\tau = 5.9$ μs. At $z = 544$ cm the calculated time width is $\tau = 6.5$ μs. At both positions, the time widths calculated from power spectra and the measured pulses agree to within the uncertainty of the pulse detection method. Furthermore, during the same plasma discharges there is an agreement between the pulses and power spectra at different axial positions.

The pulse detection and the fitting technique yield a time width that is greater than that calculated from fitting power spectra. This is seen in the results presented in Table 4.1 in which the spectral time width calculations are lower than those from the raw measured pulses. Figure 4.15 displays two extracted pulses

Parameter	Value
τ, Pulses at $z = 192$ cm	7.8 ± 2.7 μs
τ, Spectrum at $z = 192$ cm	5.9 μs
τ, Pulses at $z = 544$ cm	8.9 ± 2.4 μs
τ, Spectrum at $z = 544$ cm	6.5 μs

Table 4.1: Calculated Pulse Widths

and their corresponding Lorentzian fits. In Fig. 4.15a it is clear that the measured pulse (solid black) is fit well by a Lorentzian function (dashed red). The time width of this fit pulse is $\tau = 6.2$ μs, compared to the spectral fit value of 6.5 μs. Panel (b) displays a poor fit from the identification analysis. The time width of this fit is $\tau = 11.7$ μs, larger than that of the good fit shown in panel (a). The offset between the pulse centers in Fig. 4.15b is a result of the poor fit. This is the result of numerical issues within the routine. The automated detection of pulses is necessary in order to process the voluminous set of data, though manual review remains the most accurate method of calculating pulse widths. Issues with the detection technique may be reduced through further refinement of the numerical procedure.

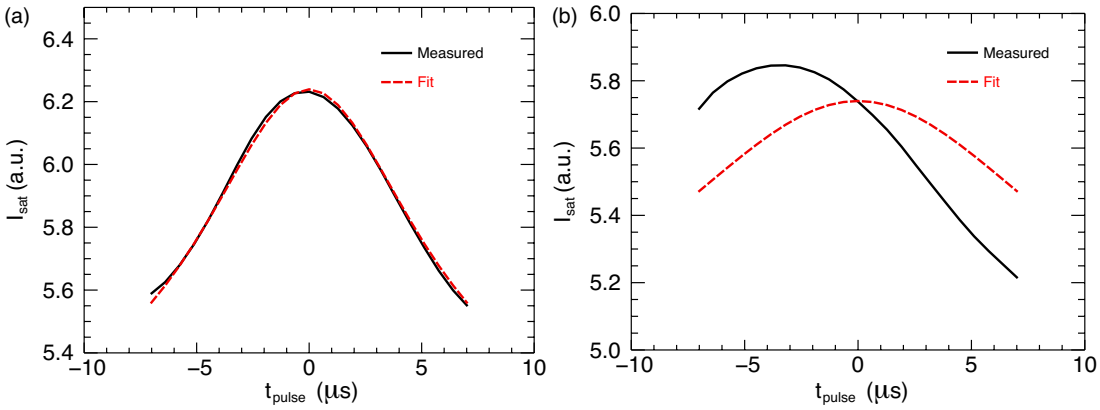

Figure 4.15: Measured pulses (solid black) and corresponding Lorentzian fits (dashed red) for the position $z = 544$ cm. (a) A good fit for which the pulse time width is $\tau = 6.2$ μs. (b) A poor fit for which the pulse time width is $\tau = 11.7$ μs. The pulse time width from fitting the power spectrum is $\tau = 6.5$ μs.

The treatment of Lorentzian pulses presented thus far assumes that a series of discrete pulses results in an exponential power spectrum. This is shown in Eq. (4.3) for a single Lorentzian pulse. A similar analytic expression is not possible for a series of pulses. The following section treats this issue by way of a model consisting of such a series of Lorentzian pulses.

4.5 Modeling Exponential Power Spectra

The expression in Eq. (4.3) illustrates that the power spectrum of a single Lorentzian pulse is exponential, but it does not immediately follow that the spectrum of a series of Lorentzians is also exponential. All of the measured spectra are the result of performing Fourier transforms on time records of such length that they contain many Lorentzian pulses. The random distribution of time centers and

widths may easily result in a non-exponential spectrum.

The resulting time series, $p(t)$, from a collection of Lorentzian pulses is given by,

$$p(t) \;=\; \sum_{i=0}^{N} L_i(t) \;=\; \frac{A_i}{1+\left(\left(t-t_{oi}\right)/t_{ci}\right)^2}\;, \tag{4.4}$$

where the pulses have different amplitudes, A_i, and different widths, t_{ci}, while being centered at different times, t_{oi}.

The Fourier transform of (4.4) is,

$$\tilde{p}(\omega) \;=\; \sum_{i=0}^{N} \pi A_i t_{ci} \exp\left(i\omega t_{oi}\right) \exp\left(-\omega t_{ci}\right)\;, \tag{4.5}$$

which is a sum of exponential terms. At this point it is no longer evident that a semi-log representation of the power of (4.5) results in a linear region. A numerical model [Shi, 2008] is used to further this investigation.

Figure 4.16 compares the measured spectrum (solid black trace) previously seen in Fig. 1.4 to a model result (dashed red) computed from an ensemble of generated signals. The model accurately reproduces the exponential character of the measured result.

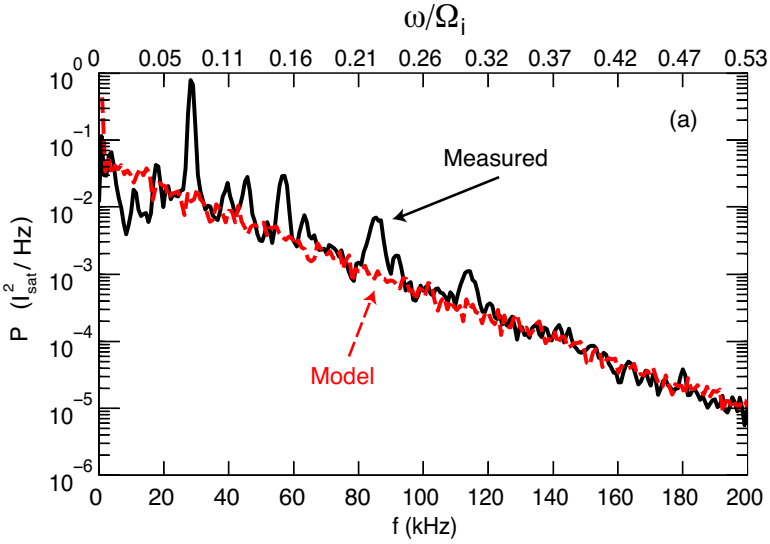

Figure 4.16: The power spectrum of Fig. 1.4 (solid black) is compared to an exponential spectrum generated by the model (dashed red). The model accurately reproduces the exponential component of the experimental spectrum, even in the presence of line spectra associated with the drift-Alfvén mode and its harmonics.

The model signals are based on Eq. (4.4). Ten Lorentzian pulses ($N = 10$) are placed into each of 100 time series. Each time series is 1 ms in total length. The center times, t_{oi}, are randomly distributed throughout the 1 ms duration. These model traces are normalized in amplitude so the values of A_i are assigned a random distribution between 0.75 and 1.25 to give an average amplitude of unity. Time widths, t_{ci}, are distributed between 2.5 and 4.5 μs, consistent with the measured values. The average time width of the model is $\langle t_{ci} \rangle = 3.5$ μs and this value results in the excellent agreement shown in Fig. 4.16. Additionally, this value agrees with the average time width computed from fitting measured pulses, $\langle t_{ci,\mathrm{exp}} \rangle = 4.0$ μs.

4.6 Generation of Lorentzian Pulses

Since the analytic shape of the pulses is observed to be Lorentzian, it is natural to direct the study toward determining the generation mechanism that results in such a particular structure. This research is presently led by the theoretical effort presented in Ch. 7 of Shi [2008]. In that thesis, a model of the $\vec{E} \times \vec{B}$ drift (plasma flow perpendicular to the background magnetic field) behavior is made for the case of two simultaneous drift-Alfvén modes. The model incorporates the combined effects of $m = 1$ and $m = 6$ drift-Alfvén modes. At large amplitude, these waves interact non-linearly and generate non-sinusoidal oscillations in density and temperature. The resulting structures are successfully fit to Lorentzian shapes and reproduce to positive-polarity/negative-polarity behavior that is observed at different radial regions of the experiment. Future work will include efforts to determine the dynamic equation that accurately describes a system that generates Lorentzian pulses, along with corresponding experimental measurements that contribute to this understanding.

4.7 Summary

The temperature filament experiment provides a unique environment in which the level of energy transport transitions from a classical phase into an anomalous phase. The fluctuation power spectra calculated during the anomalous phase exhibit exponential dependency on frequency. These exponential spectra are only observed during times for which the measured time series data features solitary pulses. The pulses are found to fit well to the Lorentzian shape of Eq. 4.1 (deviations from a pure Lorentzian are treated in the following Chapter). Lorentzian pulses are shown to produce exponential spectra, a relationship that allows for

the prediction of pulse widths based on the exponential constant measured from a spectrum. In the experiments it is possible to compare a Lorentzian width calculated from a spectrum to that calculated from an ensemble of events. The resultant time widths are found to be in agreement, further supporting the validity of the Lorentzian claim.

Finally, it is suggested that this situation is a universal feature of plasma turbulence. A listing of exponential spectra already in the research literature is given in Section 1.3.3. An experiment performed at the LAPD-U involving a controlled density gradient, called the Limiter-Edge Experiment in this thesis, presents an opportunity to test the universality of this process. Similar exponential spectra and accompanying Lorentzian pulses are observed. A comparison between the two experiments is presented in the following Chapter.

CHAPTER 5

Comparisons Between Turbulent Features of the Temperature Filament and Limiter-Edge Experiments

5.1 About the Limiter-Edge Experiment

The limiter-edge experiment focuses on properties and generation of intermittent, or bursty, turbulence structures. As with the temperature filament experiment of this thesis, the turbulence study is motivated by the relevance to transport. Intermittent turbulence is one cause of particle transport in tokamaks [D'Ippolito et al., 2002]. The LAPD-U study conducted by Carter allows for an in-depth statistical study of these bursty events, showing that intermittent structures, or "blobs", are detached and radially propagating objects with a dipole potential profile [Carter, 2006].

Figure 5.1 illustrates the geometry of the limiter-edge experiment. An electrically floating aluminum plate is installed on a hinge inside the LAPD-U. Partially closing this plate causes a blockage of primary electrons that are emitted from the cathode during the main plasma phase of a discharge. A strong density gradient results from the blocking, which is shown in Fig. 5.2.

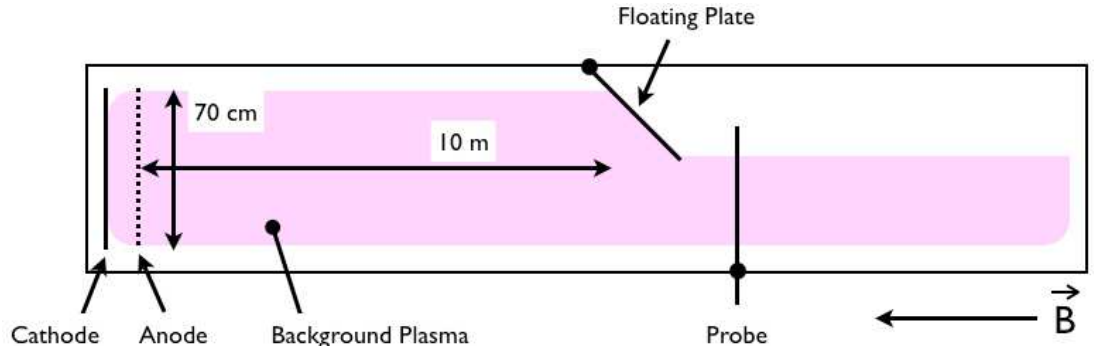

Figure 5.1: Schematic of the setup for the limiter-edge experiment in the LAPD-U. An electrically floating aluminum plate is used to partially block the emission electrons during the main plasma phase. A large density gradient is set up and intermittent structures are observed behind the plate.

5.2 Similarities Between the Limiter-Edge and Temperature Filament Experiments

The density profile shown in Fig. 5.2 is labeled to highlight the similarity between it and the temperature profile of the temperature filament experiment. Three regions are defined in Fig. 5.2: Center, Gradient, and Outer. The Center region is the main plasma column, which features a fairly flat density profile in which the only aberrations are due to asymmetries in the emitting cathode itself. Negative polarity pulses (see Fig. 5.5) are observed in this region. The Gradient region occurs across the radial boundary of the blocking plate. A unique feature within this region is the observation of both negative and positive polarity pulses. The small radial dimension of the temperature filament experiment prevents a definitive measurement of negative and positive pulses in the same region. Finally, the Outer region is behind the plate. Positive polarity pulses, often of very large relative amplitude ($\tilde{I}_{\rm sat}/I_{\rm sat} > 100\%$), are observed in this region, as shown in

Fig. 5.6.

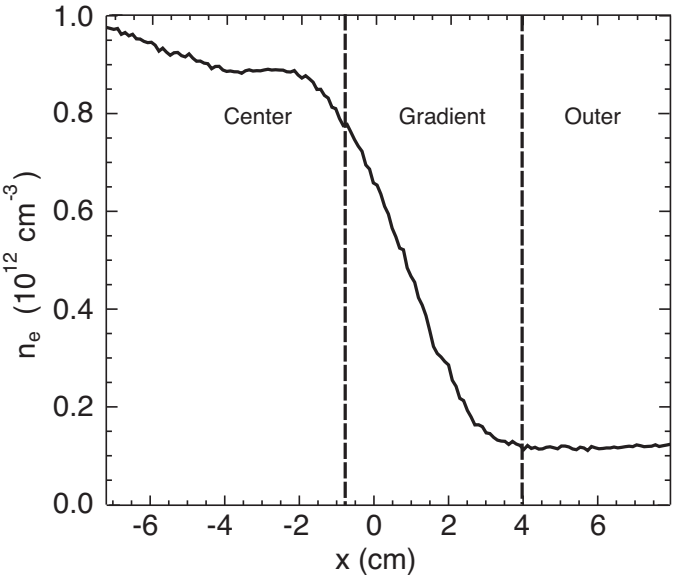

Figure 5.2: Plasma density profile from the limiter-edge experiment. Three distinct regions of behavior analogous to those found in the temperature filament experiment are labeled.

5.3 Exponential Spectra

The limiter-edge experiment exhibits exponential power spectra for I_{sat} measurements in all three regions indicated in Fig. 5.2. An aspect of this experiment is that the turbulence is always fully formed, i.e., there is never a classical transport regime and therefore no transition from classical behavior to broadband turbulence. For this reason, the time series always demonstrate pulse behavior as shown in Fig. 5.3. The gradient panel is a mixture of positive and negative polarity pulses.

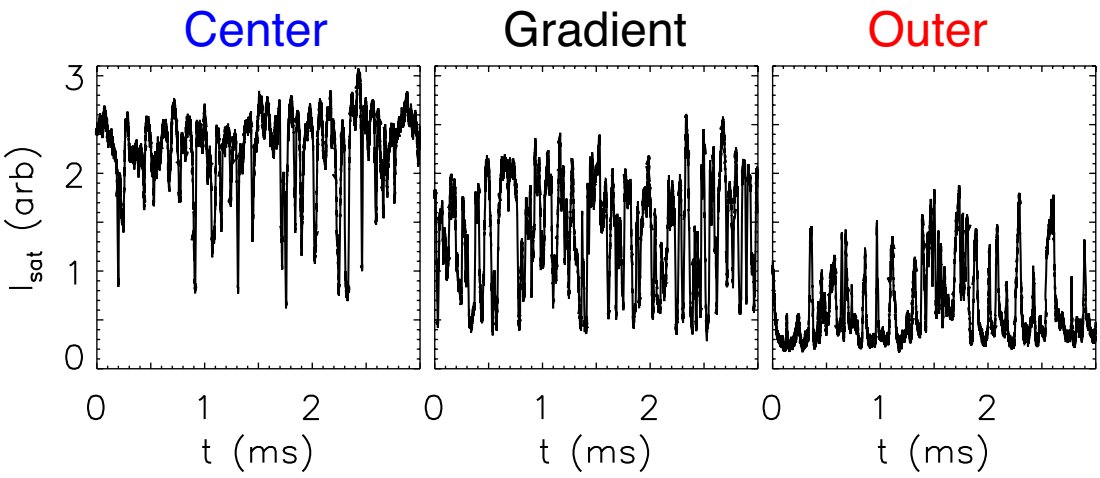

Figure 5.3: Raw I_{sat} traces from each of the limiter-edge regions shows the bursty nature of the pulses. This figure is an adapted form of that appearing in Carter [2006].

The measurements from all three regions exhibit exponential power spectra, as shown in Fig. 5.4. Fits to the exponential behavior of the spectra in this experiment yield a value of $\tau = 7.0$ μs, which compares well to the value of $\tau = 7.2$ μs obtained by measuring the characteristic widths of individual pulses. A model of Lorentzian pulses featuring characteristics consistent with those measured in the experiment also produces a power spectrum with equivalent exponential behavior.

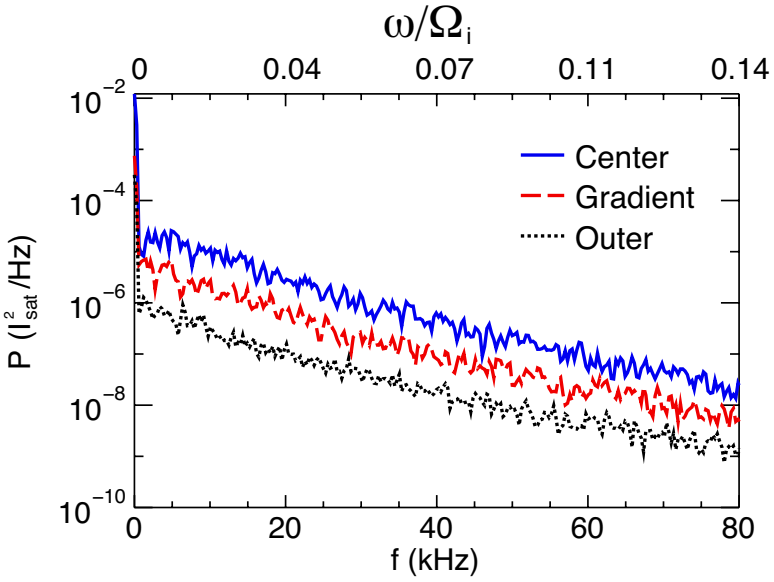

Figure 5.4: Power spectra from I_{sat} measurements in the limiter-edge experiment. The spectra are observed to be exponential from each region of the density profile.

5.4 Lorentzian Pulses

The example pulses of Figs. 5.5 and 5.6 are immediately comparable to Figs. 4.11 and 4.10 from the temperature filament experiment. The pulses themselves are more similar between these experiments than any other parameters. The negative polarity pulses from the limiter-edge are observed at amplitudes much larger than the background fluctuations.

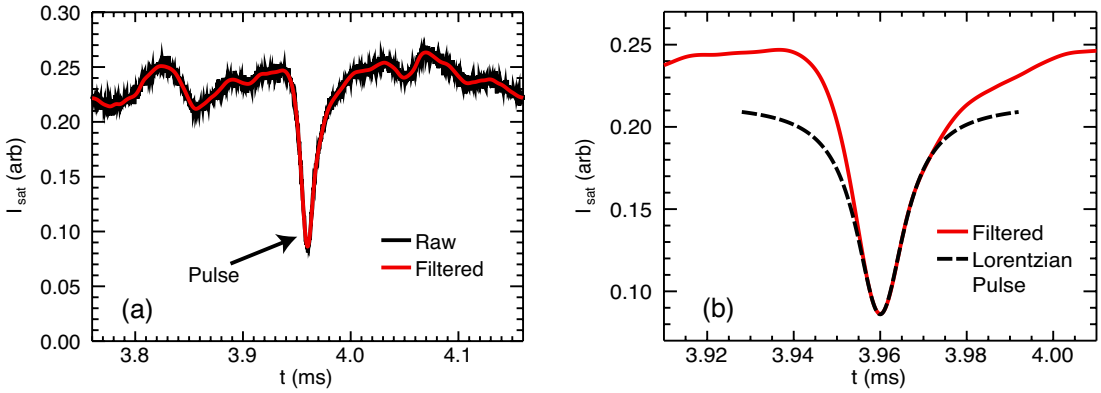

Figure 5.5: I_{sat} measurements from the center region of the limiter-edge experiment. (a) A wide view of a single, negative polarity pulse (solid black) with an overlay of a low-pass filtered signal (solid red). (b) The filtered signal (solid red) is fit with a pure Lorentzian function (dashed black).

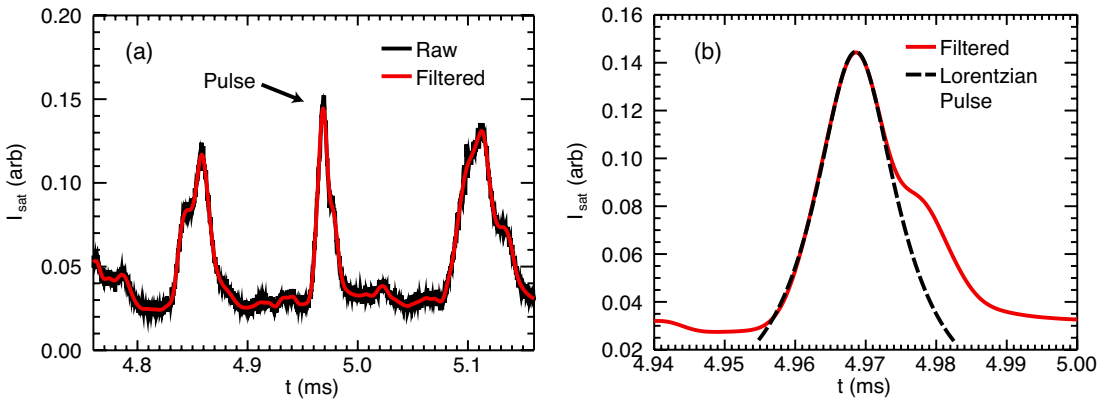

Figure 5.6: I_{sat} measurements from the outer region of the limiter-edge experiment. (a) A wide view of a single, positive polarity pulse (solid black) with an overlay of a low-pass filtered signal (solid red). (b) The filtered signal (solid red) is fit with a pure Lorentzian function (dashed black).

5.5 Distortion of Lorentzian Pulses

Additional work has been performed with regard to the presence of asymmetric pulses. A particular example from the limiter-edge experiment is presented here. The distorted pulse of Fig. 4.10 exhibits a steepened leading edge with a more slowly decaying following edge. This feature is similar to observations that have been made in "blob" studies [Antar et al., 2003; Boedo et al., 2001]. Blob phenomena [Zweben, 1985] are an ongoing area of fusion research focusing on the origination and control of intermittent bursts that are seen in the scrape-off layer and far edge of tokamaks.

An example of an asymmetric pulse measured in the limiter-edge experiment (solid black curve), together with a numerical fit (dashed red curve), is given in Fig. 5.7. This pulse has been previously shown in Fig. 5.5b. A much better fit to these asymmetric pulses can be obtained by multiplying the basic Lorentzian shape, $L(t)$, by a function of the form

$$f(t) = 1 + a\left[1 + b\left(1 + \tanh\left(\left(t - t_1\right)/t_2\right)\right)\right] \ . \tag{5.1}$$

Figure 5.7 illustrates that a very close fit to the measured asymmetric pulse can be obtained using a product fitting function of the form $f(t)L(t)$. The asymmetry of the pulse shape introduced by a function of the type given in Eq. (5.1) has very little effect on the power spectrum, as illustrated in Fig. 5.8 which shows a comparison between the power spectrum of the product fitting function, fL, the power spectrum of the basic Lorentzian, L, and the power spectrum of the individual pulse. The power spectrum of the Lorentzian (solid black line in Fig. 5.8) and the skewed Lorentzian (dashed red line labeled "fit") are almost indistinguishable and both represent the power spectrum of the individual pulse very well, but for a slight deviation at higher frequencies. The exponential nature

is retained over a broad frequency range. This example shows in detail that the asymmetry of pulses observed in the data does not destroy the exponential nature of the power spectrum.

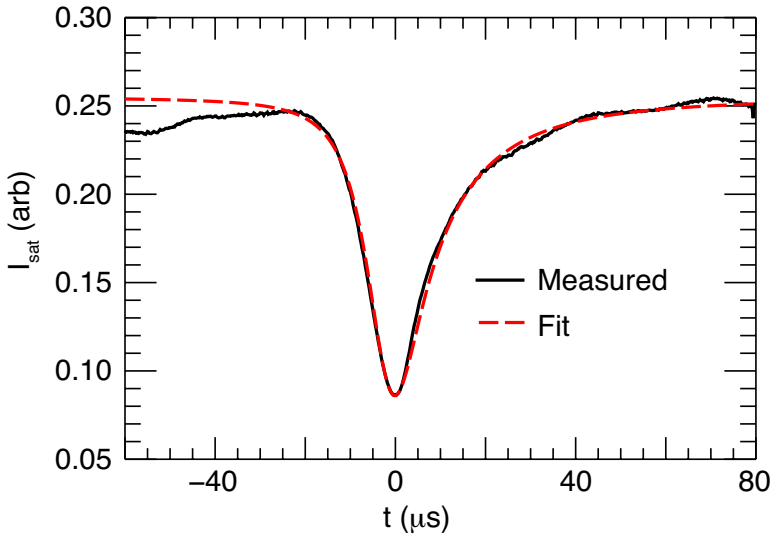

Figure 5.7: Solid black curve is a measured pulse previously shown in bottom right panel of Fig. 5.5b. Dashed red curve is functional fit consisting of a Lorentzian multiplied by a distortion given by Eq. (5.1).

While the particular example given here shows no discernable difference between the power spectrum of the basic Lorentzian fit and the product fitting function, the general case is that the power spectra of the two fits will differ. The differences are found to be small and occur at low frequencies (below 20 kHz). In general, observed asymmetries in individual pulse shape do not alter the exponential nature of the power spectrum.

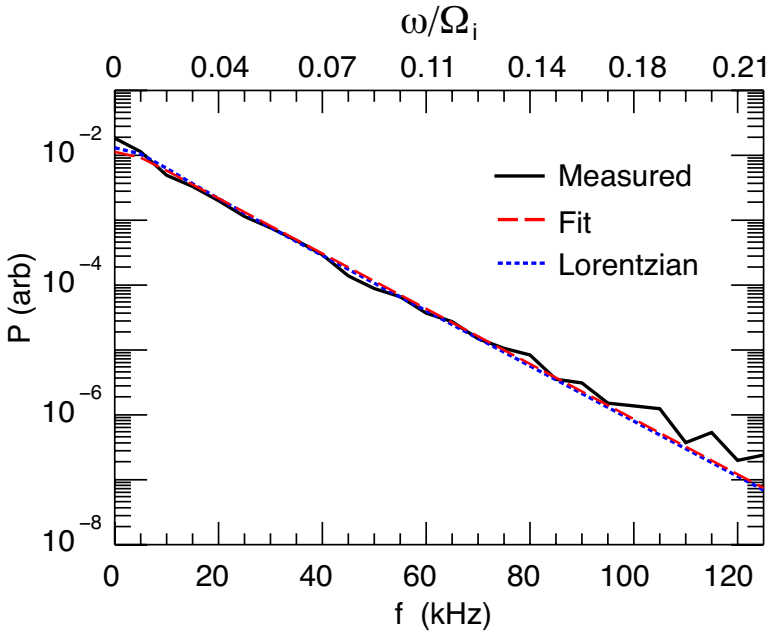

Figure 5.8: Power spectra of the measured pulse (solid black) compared to that of the fit (dashed red) and of the fundamental Lorentzian pulse (dotted blue). The normalized frequency scale corresponds to the limiter-edge experiment in which the pulse is observed.

5.6 Summary

The similar time series and spectral results from the temperature filament and limiter-edge experiments supports the concept of exponential spectra as a universal feature of plasma turbulence. The limiter-edge experiment further supports the universal aspect of the pulses and exponential because of its relationship to intermittent transport in tokamaks. The limiter-edge may be described as a series of filamentary structures. This view applies to the scrape-off layer or outer region of toroidal plasma as well. Similarities between the limiter-edge and temperature filament experiments indicate that the single filament environment produces be-

haviors that are observed in the even more turbulent environments observed in other plasmas.

CHAPTER 6

Plasma Flow Parallel to Background Magnetic Field

Plasma flow is studied in relation to another aspect of this thesis, namely the thermal wave. This section examines describes flows aligned with the applied background magnetic field, i.e., parallel flows.

6.1 Spatiotemporal Behavior and Modeling

A comparison of the time evolution of parallel flow between measurements and a theoretical model is presented in Fig. 6.1. The model is designed using Eqs. (2.4) - (2.7). This analysis is restricted to the early times that correspond to the classical transport regime of the filament. The position of this measurement is $(r, z) = (0, 384)$ cm. The rise in the measured flow velocity immediately after beam heating begins is not captured in the model result. It should be noted that differences in the numerical values between the flow measurements and the code are expected to be larger than those observed for temperature comparisons. The model calculates flow values by solving for the absolute value of the flow and then normalizing it to the sound speed as calculated using its own temperature value. Therefore, any differences present in the absolute flow speed (which cannot be measured by the Janus probe method) are compounded by the differences in

temperature.

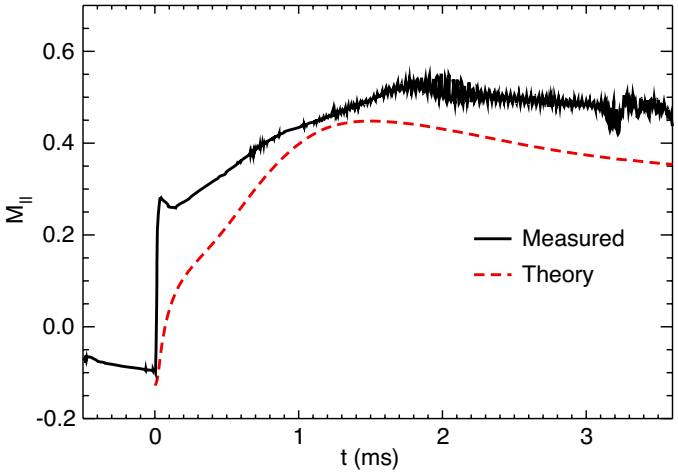

Figure 6.1: Comparison of measured and theoretical parallel flows in the filament center for early time evolution. The model result captures the qualitative behavior of the flow, except for the initial (and possibly transient) increase in magnitude. The measured trace has been smoothed to reduce higher frequency fluctuations.

Figure 6.2 compares two-dimensional flow profiles from the experiment with the results of the fluid code that is also used to compare classical temperature profiles. The result is shown for the axial position $z = 384$ cm. The qualitative agreement is excellent as both results identify a wide radial profile of plasma flow. One difference is the sharp edge that appears just after $t = 1$ ms in the measurement. It is not yet understood why the model would result in a softer edge profile. The direction of the flow also agrees within these two representations. Early in the filament evolution and far into the outer region of the radial profile, the flow is directed toward the LaB_6 beam source. Some time after the heating process has begun, this direction is reversed. Pressure gradients naturally present in the afterglow plasma compete with those generated by the beam heating. This

interaction may explain the sharp boundary observed in the experiment but not entirely reproduced by the model.

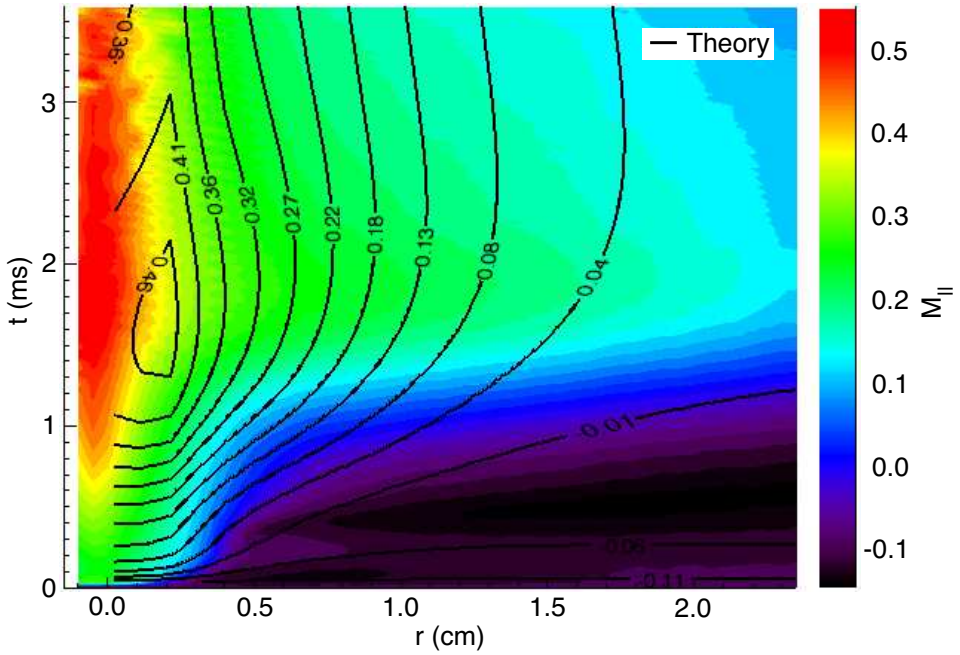

Figure 6.2: Parallel flow velocity as measured (color contour) and as predicted by classical theory (black lines).

Quantitatively, the agreement between the model and the measurements is nearly perfect at the far edges and early times, and better than 20% at the filament center. The gradient region exhibits larger discrepancy between the values (e.g., at $t \approx 2$ ms and $r > 1.5$ cm). The theoretical result places the peak flow just off the center of the filament. It is noteworthy that the largest absolute value of flow is centered on the filament in the model. The off-center feature occurs because the model temperature profiles decrease faster than the absolute velocity. The temperature decline in the radial direction reduces the ion sound speed much faster than the corresponding reduction in absolute flow speed. Similar off-center peaks in Mach number are not observed in the measurements.

Figure 6.3 is a plot of the measured and theoretical electron temperatures and flow profiles corresponding to time $t = 1.3$ ms in Fig. 6.2. This display clarifies the evaluation of that preceding contour. Both radial profiles are broader than typical temperature profiles for the filament. The measured profile exhibits a steady decay of the flow and appears to never reach a lowest level. This contrasts the result from the model in which the profile is still broad but does flatten out near $r = 2$ cm.

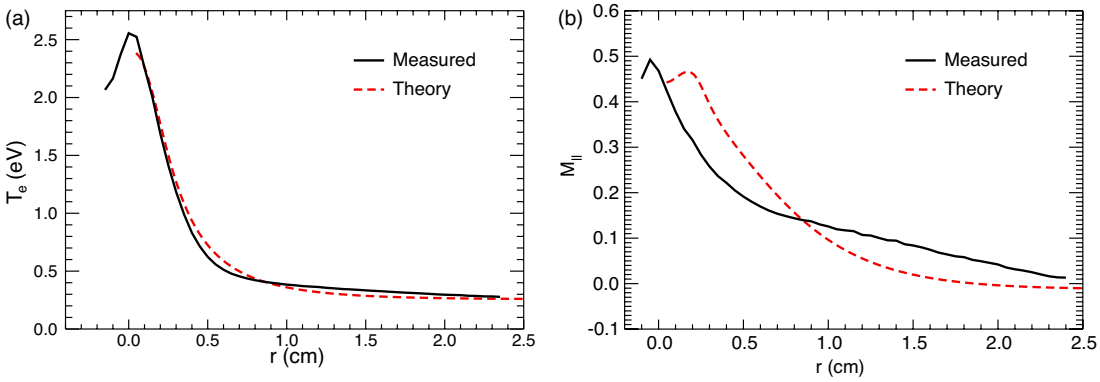

Figure 6.3: Radial profiles taken from time $t = 1.3$ ms for $z = 384$ cm. (a) Electron Temperature (b) Flow

An interesting overview of flow behavior across multiple axial positions is shown in Fig. 6.4, which presents contours of the parallel flow as functions of radial position and early time. Notice that panel (b) was acquired with a radial range that differs from the other two contours. Panel (a) displays the flow from within the heat source region, Q, at $z = 64$ cm. Oscillations arise near $t = 1$ ms that are comparable to those shown in the time trace of Fig. 2.12. These same oscillations are also observed at the other axial positions of $z = 224$ cm in (b) and $z = 448$ cm in (c). The downstream regions demonstrate the coherent fluctuations prior to their appearance in the Q region. Panels (b) and (c) exhibit

striations (which are representative of oscillations in this contour display) before $t = 1$ ms and they do not appear until after this time in (a). This observation suggests that the cause of the oscillations is within the heated filament and not driven by the beam heating directly, i.e., there are no such oscillations in the applied heating power.

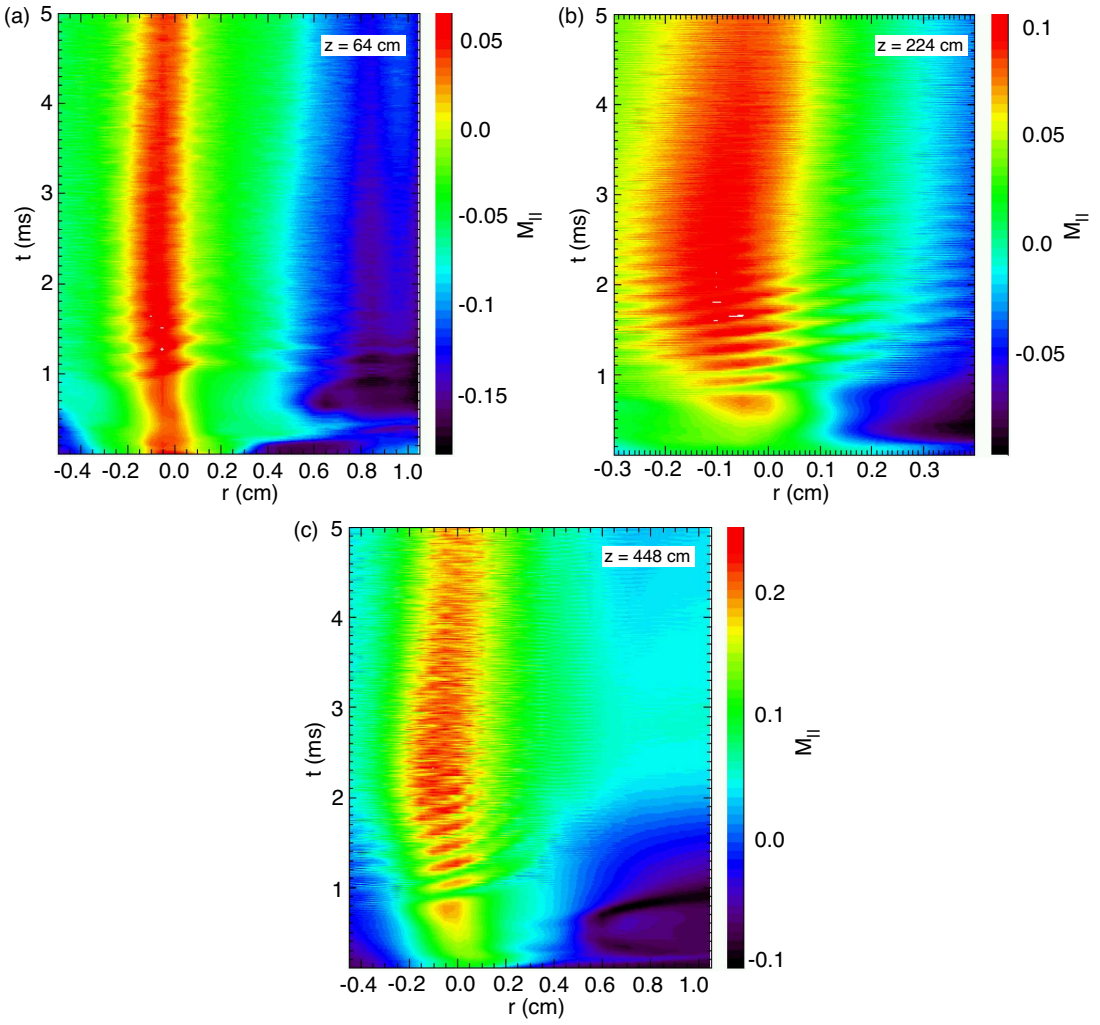

Figure 6.4: Parallel flow contours at different axial positions for the same experimental parameters, $B_o = 900$ G, $V_{beam} = 20$ V. These are not from the same discharge, however, because a number of discharges is necessary to obtain the contour measurement across the radial dimension (note also that (b) is acquired across a narrower radial span than the other panels). (a) $z = 64$ cm (b) $z = 224$ cm (c) $z = 448$.

Figure 6.4 also highlights the time evolution of the broad flow profile. This is determined by the interface of the opposing flows in the $r > 0.1$ cm regions.

The negative flow values of (a) indicate that the plasma is flowing toward the LaB_6 electron beam. Plasma flowing away from the beam is restricted to a region narrower than the beam diameter. At $z = 224$ cm the flow direction changes suddenly near $r = 0.1$ cm and $t = 1$ ms. The profile of flow away from the LaB_6 crystal extends out to $r > 0.2$ cm. Finally, at $z = 448$ cm the flow directed away from the heat source reaches out to $r > 1.0$ cm, far wider than at the other axial positions. Similar profiles are predicted by the code because the parallel gradients are largest away from the LaB_6 crystal. Closer to the LaB_6 source, the parallel pressure is flat and the flow drive is reduced. Furthermore, the background electron temperature is lower farther from the beam, leading to a much lower ion sound speed and greater Mach number even in instances in which the absolute flow speed is constant.

An example of the time evolution of the Mach number at different axial positions is given in Fig. 6.5. The time evolution of the flow at the filament center confirms the larger Mach numbers corresponding to larger z values. Large amplitude fluctuations appear first at the $z = 384$ cm position ($t \approx 4.5$ ms). Similar fluctuations next appear on the $z = 576$ cm trace just after 4.5 ms and then finally appear on the middle axial position near 5.5 ms.

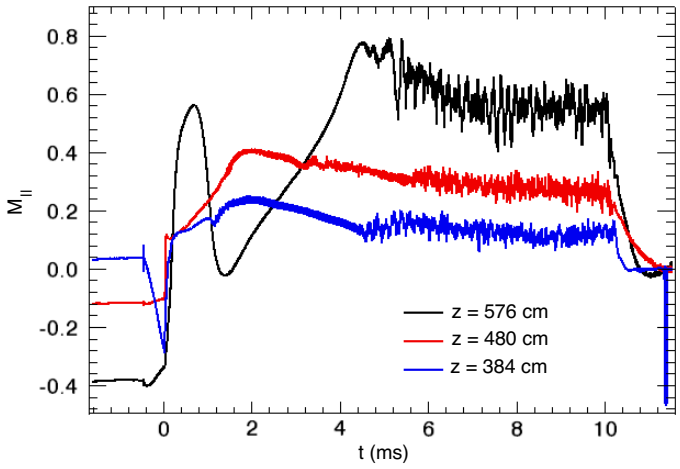

Figure 6.5: Parallel flow at the filament center for three different axial positions. The axial positions are $z = 576$ cm (black, top trace at $t = 8$ ms), $z = 480$ cm (red, middle trace at $t = 8$ ms), and $z = 384$ cm (blue, bottom trace at $t = 8$ ms).

6.2 Relation to Thermal Wave

Measurements of parallel flow in the center of the filament indicate that the thermal wave modulates the flow. Figure 6.6 is a plot of the parallel flow at the filament center in the Q region at $z = 64$ cm. The time separation between the largest peaks in the flow correspond to the period of the thermal wave measured in the same parameter regime (but not in the same discharges).

The higher frequency oscillations in Fig. 6.6 are approximately 35 kHz, placing them within the frequency range of the coherent drift-Alfvén mode. The earliest range of the plot shows growing amplitude for these oscillations with a culmination in the large peak that sets the beginning time for comparison to the thermal wave.

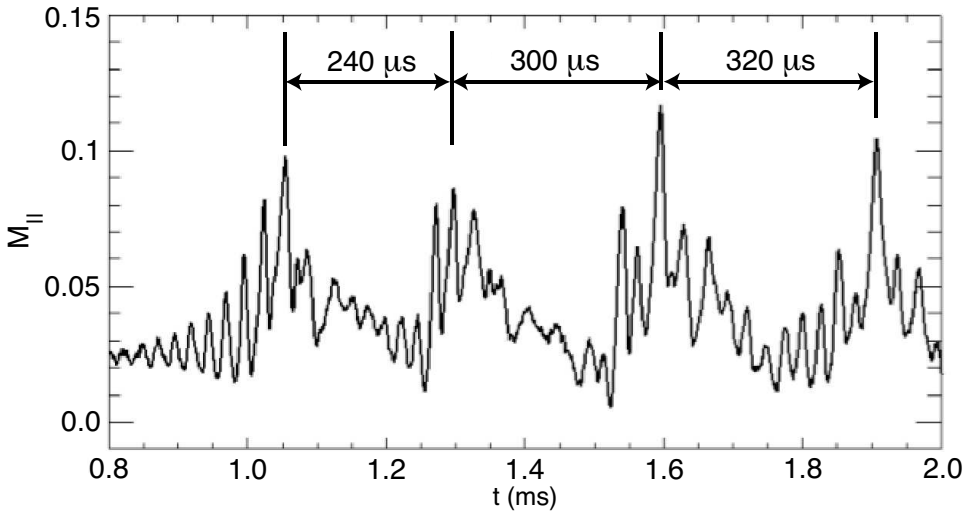

Figure 6.6: Time trace of parallel flow at the filament center in the Q region. The time period between large amplitude peaks is highlighted for comparison to the similar period of the thermal wave. The faster oscillations correspond to the drift-Alfvén wave.

Figure 6.6 represents typical fluctuation behavior of the parallel flow. These oscillations exhibit an amplitude of,

$$\frac{\delta M_{\|}}{\langle M_{\|} \rangle} \leq 50\% \, . \tag{6.1}$$

As seen in the figure, the flow exhibits periodic behavior on both a slower timescale (due to thermal wave modification), and a faster timescale (the higher frequency component unlabeled in the figure). The higher frequency component corresponds to the drift-Alfvén frequency, $f \approx 40$ kHz. Both the thermal wave and the drift-Alfvén wave modulate the parallel flows.

Though the magnitude of the flow fluctuates, it does not change direction. As in Fig. 6.6, the value of the Mach number remains positive throughout the fluctuations. This indicates that the direction of the flow is always toward the

LAPD-U anode (i.e., away from the beam heat source). Flow oscillations therefore represent a decreasing/increasing response, and not a change in the absolute direction of the mass transport. These fluctuations do not alter the mean flow.

6.3 Flow as a Function of Input Power

Figure 6.7 presents time traces of parallel flow for two axial positions and various input heating powers. The nearly steady-state Mach number for 20 V in (a) is approximately 0.3, while that value approaches 0.6 further downstream at $z = 576$ cm in panel (b).

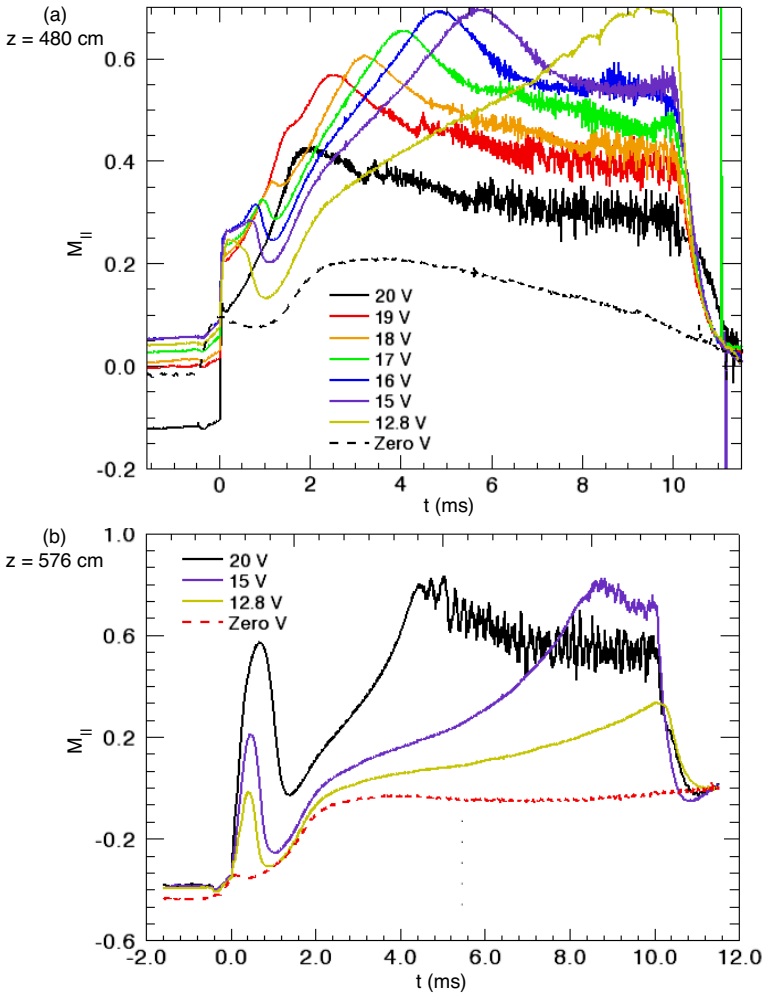

Figure 6.7: Parallel flow for multiple input heating powers (expressed as beam voltage) at (a) $z = 480$ cm and (b) $z = 576$ cm.

Larger Mach numbers for lower values of the heat input also support the model's finding. Lower values of heat input result in a shorter length of the resulting filament. For any fixed axial position within the filament for a 20 V experiment, a lower input heating brings the end of the filament closer to the measurement position (until the point at which the filament no longer extends to that position). Both panels show a maximum Mach number above 0.6, possibly

indicating the end of the filament. In Fig. 6.7b it is possible that the 15 V experiment barely reaches the $z = 576$ cm position within the heating time interval. The 20 V case reaches this same maximum Mach number earlier in time and then features a decrease to a steady-state behavior. In contrast, the 12.8 V situation never reaches this maximum and is still increasing when the input heating is shut off. Perhaps longer heating times would allow this trace to match the behavior of the others.

The theoretical model accompanying this experimental work indicates that the filament length does not change appreciably with increased beam voltage. Furthermore, it suggests, by way of Fig. 6.8, that the end of the filament is well past the measurement locations presented in Fig. 6.7. Figure 6.8 is a plot of the theoretical axial electron temperature profile as a function of beam voltage. This plot represents the maximum length of the resulting filament. For the measurement positions of $z = 480$ cm and $z = 576$ cm, as shown in Fig. 6.7, the temperature filament certainly reaches the probe. Peaks in the parallel Mach flow are observed for beam voltages between 16 and 20 V in Fig. 6.7a. The model result concerning filament length contradicts the interpretation of the measurements that measured peaks in the flow correspond to the axial end of the filament passing through the measurement location. The temperature filament is predicted to extend beyond the axial measurement locations. Though not shown, the model also predicts that the temperature filament reaches its final length in a very short time, on the order of microseconds. The measured peaks in parallel flow occur much later in time compared to the development of the temperature filament.

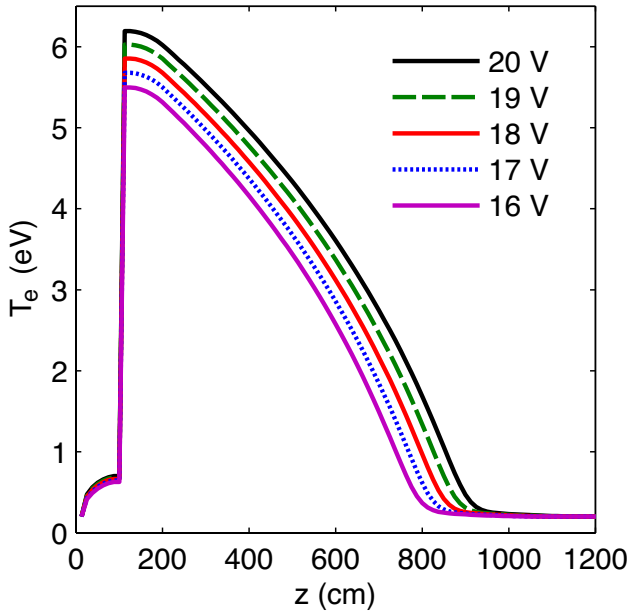

Figure 6.8: Axial electron temperature profiles from a theoretical model for different values of electron beam voltage.

The model also suggests that the parallel flow will reach supersonic levels (i.e., $M_{\parallel} > 1$) near the axial end of the filament. In Fig. 6.9 the parallel Mach number is plotted for a range of electron beam voltages. Comparing this with the theoretical axial electron temperature profiles of Fig. 6.8 shows that supersonic flow occurs near the end of the filament at $z \approx 800$ cm. These results suggest that the axial extent of the filament may be determined by appropriately designed experimental measurements of the parallel flow.

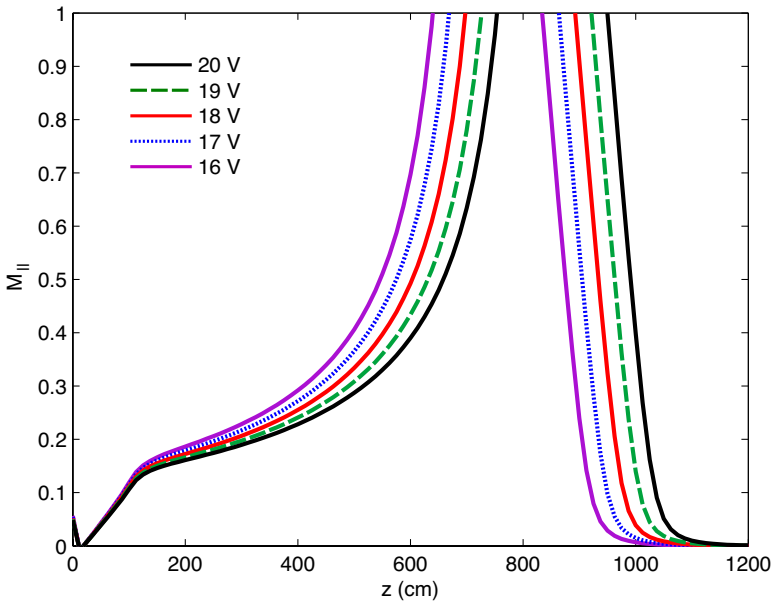

Figure 6.9: Theoretical parallel Mach number for different values of the electron beam voltage.

6.4 Summary

Measurements of plasma flow is thus far limited to determination of the Mach number in the direction parallel to the applied background magnetic field. Heating from the electron beam results in a flow toward the main LAPD-U cathode-anode pair (i.e., away from the source that generates the temperature filament). Profiles of the parallel flow are considerably wider than those of electron temperature. A fluid model, the same one that provides descriptions of the classical temperature profile behavior, reproduces the qualitative behavior of the measured flow, though the quantitative agreement is not as strong as for the temperature comparisons.

The thermal wave modulates the parallel flow. This is observed in the ap-

pearance of flow pulses, or bursts, that occur with a time period corresponding to that of the thermal wave. The amplitude of flow fluctuations reaches values of $\delta M_{\parallel}/M_{\parallel} \leq 50\%$.

The fluid model of Shi produces axial temperature profiles that place the filament length within expectations based on the flow measurements. Furthermore, the model calculates that supersonic flows are achieved at the axial end of the temperature filament. The flows have been measured well short of the $z \approx 800$ cm theoretical temperature filament length, possibly explaining the lack of a supersonic observation.

CHAPTER 7

Conclusions

Studies of filamentary pressure structures are an ongoing work within the LAPD-U laboratory. The work of Burke et al. [1998, 2000a,b] (and [Burke, 1999]) established the ability of this experimental geometry to observe classical transport in magnetically confined plasmas. An increase in transport and the loss of classical confinement for larger pressure gradients and/or longer heating periods naturally provided an opportunity to study turbulence. A reproducible characteristic of power spectra from measurements made during the anomalous transport phase of the experiment led to the identification of Lorentzian pulses in time series data. Large amplitude examples of these pulses emphasized the role of low frequency oscillations and led to the identification of a spontaneous thermal wave.

7.1 Spontaneous Thermal Waves

The temperature filament acts as a resonance cavity for spontaneous thermal waves [Pace et al., 2008b]. Thermal waves result from the diffusive propagation of thermal energy across boundaries that separate regions of largely differing thermal conductivity. In the filament, this wave manifests itself as coherent fluctuations in electron temperature near the filament center. A drive source has not been identified, though it is clear that the input heating does not oscillate in such a manner as to be solely responsible.

The wave number vectors of thermal waves depend on the thermal conductivity of the medium. Wavelength measurements, in the form of phase velocity or amplitude decay measurements, allow for calculation of these plasma parameters. From Eq. 3.5 it is seen that the electron collision frequency can also be calculated based on knowledge of the thermal wave's properties. Given that the measurement of temperature fluctuations due to the presence of a thermal wave can be considerably simpler than measurement or modeling of fundamental plasma parameters, it is natural to suggest that a purposely driven thermal wave may be useful as a diagnostic instrument. Such a wave can be driven by external heating (e.g., electron cyclotron resonance heating) or with an electron beam setup similar to the one used here.

7.2 Exponential Power Spectra Related to Lorentzian Pulses

The power spectra calculated from time series measurements of plasma properties are found to exhibit an exponential dependence in frequency that is the result of Lorentzian shaped pulses in the raw signals [Pace et al., 2008a]. The exponential constant of the spectral shape is found to agree with the time width of the generating pulses, thereby providing support for the relation between the pulses and spectra. In the temperature filament experiment it is observed that the pulses appear only after the system transitions from classical transport into a turbulent regime of enhanced transport. Observations of exponential power spectra from many different plasma experiments suggest that Lorentzian pulses are a universal feature of plasma turbulence driven by cross-field pressure gradients. Comparison with a density gradient experiment of different scale length shows similar observations and demonstrates that this phenomenon is a general consequence of systems featuring pressure gradients.

Coherent drift-Alfvén eigenmodes present in the temperature filament suggest a generation mechanism for the Lorentzian pulses. The pulses appear to result from convective bursts of a nonlinear interaction between two drift-Alfvén modes of different m-number. Work on this topic is detailed in Shi [2008].

7.3 Future Work

Just as this thesis extends the earlier work performed by Burke [1999], it is possible that future thesis projects remain to be completed within this versatile experimental geometry.

7.3.1 Thermal Waves

The initial study of the thermal wave presented here should be expanded. Diagnostic difficulties prevented the complete elucidation of the wave's properties by limiting measurements of the wave vectors. In order to minimize perturbations, an imaging diagnostic should be considered. There is a considerable amount of visible light emanating from the temperature filament and it may be possible to detect oscillations caused by the thermal wave. It is unclear how this may be implemented in a manner that provides axial resolution.

During this study of the thermal wave, multiple attempts were made to forcibly drive the wave by modulating the input beam heating. These attempts were unsuccessful due to the difficulty in modulating the beam current during the afterglow phase. This difficulty might be overcome by building an anode onto the existing beam structure. The LAPD-U anode is 16 m away from the crystal, creating a weak electrical connection even in the presence of the plasma. Finer control of beam emission will likely be achieved by bringing the anode closer to

the crystal. Since the LAPD-U anode cannot be adjusted to this end, a change to the beam structure is warranted. Controlled experiments of driven thermal waves will be useful for further developing the diagnostic capabilities of this wave.

7.3.2 Exponential Spectra

While there is a wide range of theoretical work to be performed with regard to the exponential spectra, there is still a contribution to be made by experiments. The next phase of experimental research will likely focus on spatial measurements of the Lorentzian pulses. Some measurements indicate that these pulses are azimuthally localized, but the lack of a radial or azimuthal array of probes makes it difficult to reach any certain conclusions in this regard. The spatial behavior of the pulses is vital in order to understand their generation. This will also help in determining the similarities and differences between the time series pulses from other types of plasmas. Filamentary structures in fusion devices are generally known to be coherent structures that propagate radially outward. The pulses in the temperature filament experiment do not appear to feature similar behavior and it will be instructive to determine this with certainty.

7.3.3 Filamentary Structures

Nonlinear interactions between drift-Alfvén waves might be studied by the inclusion of a second filament. Experimentally, this is accomplished by adding a second electron beam to the existing setup. The two beams, with an adjustable radial separation, each generate a filamentary structure that supports coherent drift-Alfvén eigenmodes. Adjustments to the amount of overlap of these modes should allow for control over the types and amplitudes of their interactions. The resulting system may begin to accurately model that of the limiter-edge exper-

iment discussed in Ch. 5. The pressure gradient of that experiment creates a full range of drift-Alfvén modes simultaneously. Plasma edges in other devices may have the same quality. As the single temperature filament aids in describing the behavior of these waves and plasma transport in general, so too might the double-filament experiment begin to reproduce the behavior of plasmas in which turbulence is always fully developed.

The temperature filament experiment provides a basic plasma environment that can simulate the situation encountered in other devices. The physics uncovered in this geometry is applicable to space and laboratory plasmas. Many research topics remain to be explored within this experimental setup and a wealth of "future work" will certainly add to the field of plasma physics.

APPENDIX A

Wavelet Analysis to Calculate Power Spectra

A.1 Overview

Wavelet analysis techniques, while not as commonly understood as Fourier analysis, are nonetheless frequently applied to problems in which time and frequency information are desired simultaneously. Analysis suites such as IDL (popular in plasma physics circles) provide complete libraries for easily incorporating these techniques into a research program. One of the best introductory pieces on wavelet analysis [Torrence and Compo, 1998], serves as the foundation for the IDL implementation (see notes in source file wv_cwt.pro, a routine used for the analysis presented here).

It is not the aim of this thesis to reproduce basic introductory material that is readily available, so the details of wavelet analysis are left to the many textbooks and other materials that exist. In simplified terms, a wavelet analysis is the application of a bandpass filter with logarithmic spacing in the frequency domain. The discussion in this Appendix concentrates on comparison to and validation against the more well established Fourier techniques that can be applied to the same data.

A wavelet as a function of time, $\Psi(t)$, is defined as (Eq. 6.1.4 of Debnath

[2002]),

$$\Psi(t) \;=\; \frac{1}{\sqrt{a}}\Psi\left(\frac{t-b}{a}\right)\,, \tag{A.1}$$

where a is a scaling parameter that sets the frequency represented by the wavelet and b determines the time center of the wavelet. The Continuous Wavelet Transform (CWT), $\mathcal{W}$, of a function of time, $f(t)$, is (Eq. 6.2.4 of [Debnath, 2002]),

$$\mathcal{W}(f) \;=\; \int_{-\infty}^{\infty} f(t)\overline{\Psi(t)}dt\,, \tag{A.2}$$

where the scale and time center is still determined by the a and b parameters of the wavelet. The wavelet power spectrum, $P_{\rm w}$, is therefore given by $P_{\rm w} = |\mathcal{W}(f)|^2$.

A full spectrogram is generated through wavelet analysis by setting the scale (a) to a constant value and solving across all time values (b). Repeating this process for all scales that translate to a relevant frequency completes the analysis.

A.2 Parameters of Wavelet Analysis

The description of wavelet analysis as a logarithmically spaced comb filter (i.e., picking out the power in a specific, non-continuous array of frequencies) easily incorporates the concept of basis functions. The basis function is the specific filter used in the analysis. Wavelet basis functions come in a wide variety and it is left to the user to determine the best option for any given analysis. This is a difficulty in wavelet analysis that has no analog in Fourier analysis because that transformation is unique.

Wavelet basis functions can be real or complex valued, discrete or continuous, and orthogonal or non-orthogonal. The turbulence study presented here depends on the availability of phase analysis, which immediately requires that only complex valued basis functions be used. The ability to review specific ranges of

frequencies is also necessary, suggesting the use of continuous bases. These two desired properties are the most important features to consider. The primary difference between the orthogonal property choices of a wavelet basis is that a non-orthogonal basis will "double-count" the power contribution of some frequencies, thereby returning inaccurate absolute amplitudes. The basis ultimately chosen for this work, the Morlet wavelet, is non-orthogonal. The potentially inaccurate amplitudes of the power spectra are overcome by only applying this technique to study the temporal behavior of modes and not their spatial structure or other features that rely on amplitude measures.

The Morlet wavelet, Ψ_{M}, is written as (Eq. 6.2.12 of Debnath [2002]),

$$\Psi_{\mathrm{M}} \;=\; \exp\left(i\omega_o t - \frac{t^2}{2}\right) \;, \tag{A.3}$$

where ω_o is a variable describing the frequency at which the Fourier transform of the Morlet wavelet demonstrates peak amplitude.

To review the behavior of wavelets used in various analyses it is helpful to utilize test signals. Figure A.1 is a plot of pure sine waves of 5 kHz (top) and 50 kHz (bottom). Both signals are centered on zero for the spectral analysis and only offset to provide for clear review in the figure.

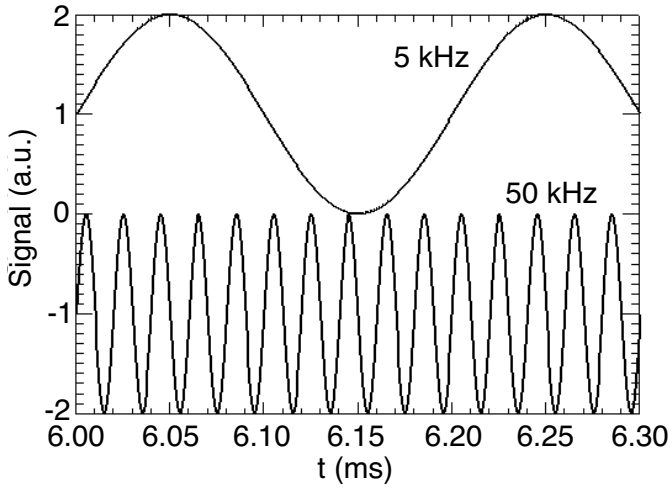

Figure A.1: Pure sine waves of 5 kHz (top) and 50 kHz (bottom) used to demonstrate the resolution of wavelet power spectra.

The 5 kHz test signal is used to highlight the frequency resolution of the Morlet wavelet. Figure A.2 compares the power spectra of the 5 kHz test signal for three wavelet basis functions: Morlet, Gaussian, and Paul. The Gaussian and Paul wavelet return similar results that exhibit poor frequency resolution compared to the Morlet. This early benchmarking of wavelet performance is necessary because of the numerous options in setting the parameters of the analysis. Deciding on the Morlet basis is relatively simple, but it remains to compare the Morlet wavelet results to those computed with standard Fourier methods.

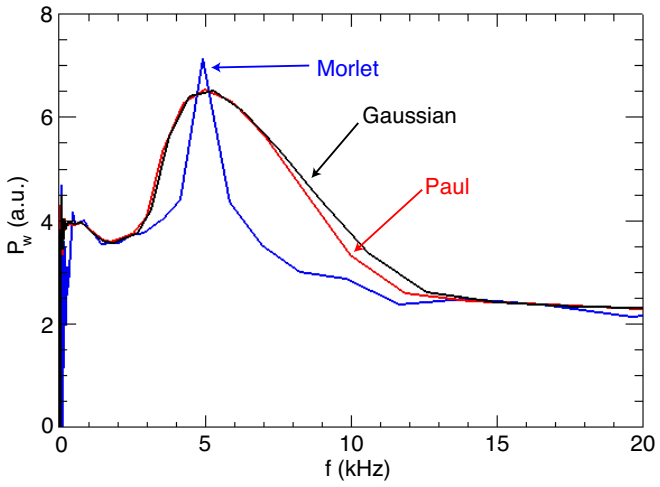

Figure A.2: Wavelet power spectra to identify the test signal's 5 kHz mode using different wavelet basis functions. The Morlet wavelet results in the best frequency resolution.

A.3 Fixed Frequency Test Signals

The most significant difference between a wavelet spectrum and that of an FFT is that the wavelet technique results in a bandwidth that is frequency dependent. The bandwidth, or frequency resolution, of an FFT is determined by the total length of the input, l. The frequency resolution is constant and given by $\Delta f = 1/l$ where l is the time length of the data window over which the FFT is performed. For a time series of N data points, output power spectrum provides a value for every frequency from $f = 0$ to $f = (N/2)(1/l)$.

Wavelet analysis returns spectra in which the value of $\Delta f/f$ is constant [Farge, 1992]. For an FFT, $\Delta f/f$ decreases with increasing frequency because Δf is constant. In a wavelet result, the resolution of higher frequency terms is worse than that of lower frequencies. An illustration of this is shown by analyzing the

test signals of Fig. A.1.

Figure A.3 plots the resulting power spectra from performing transforms using either FFT or Continuous Wavelet Transform (CWT) techniques. Peaks in the FFT spectra accurately identify the center frequencies of the test signals. The peak in the 5 kHz result (green) is just as narrow as the peak corresponding to the 50 kHz result (blue). Peaks from the CWT analysis demonstrate a reduction in frequency resolution for the higher frequency wave. The ratio of the frequency spacing to the center frequency is constant for the CWT result. Figure A.3, can be used to calculate these values,

$$5 \text{ kHz} \qquad \frac{\Delta f}{f} = \frac{2.026}{5} = 0.405 \,, \tag{A.4}$$

$$50 \text{ kHz} \qquad \frac{\Delta f}{f} = \frac{18.91}{50} = 0.378 \,. \tag{A.5}$$

This demonstrates that wavelet techniques are comparable to Fourier techniques for calculating power spectra. In the context of this thesis, wavelet analysis is used to provide a broad picture of the time evolved spectra. Any determination of a particular mode frequency is done with Fourier analysis in order to more precisely determine the value.

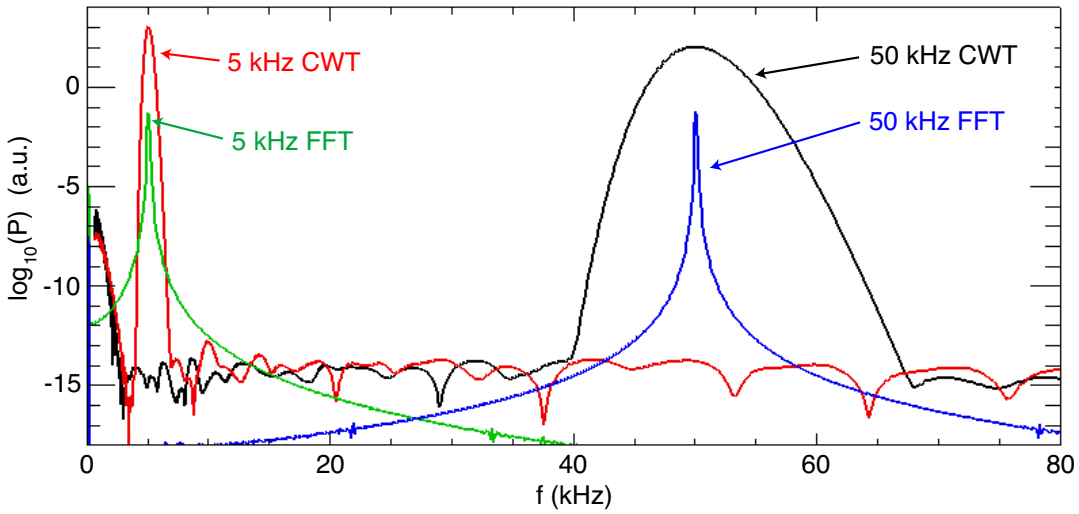

Figure A.3: Power spectra of the test signals. The FFT analysis is clearly peaked at the frequencies of the test signals. The CWT results provide a less clear peak for the higher frequency signal.

A.4 Evolving Frequency Test Signals

Figure A.4 is a narrow time view of the test signal used to demonstrate the ability of the wavelet analysis technique to discern the temporal behavior of coherent modes. This signal is a regular 5 kHz sine wave onto which a 17 kHz sine is added, beginning at $t \approx 5.25$ ms. A spectrogram of this test signal is expected to reveal the constant presence of the 5 kHz and the sudden onset of the 17 kHz oscillation.

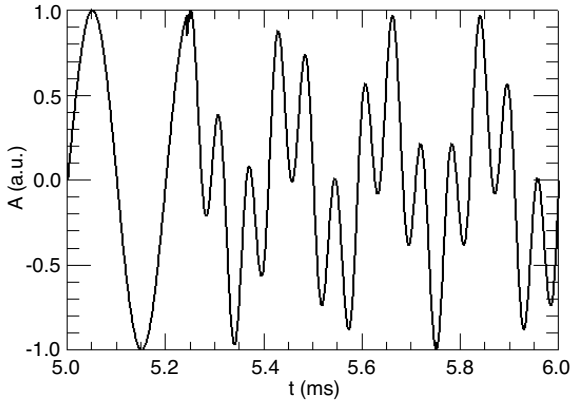

Figure A.4: The amplitude, A, of the test signal featuring a secondary frequency. This narrow time region of the complete signal highlights the activation of a 17 kHz signal at $t \approx 5.25$ ms. The background, constant, oscillation is a 5 kHz wave.

Figure A.5 is a wavelet spectrogram of this test signal. The constant 5 kHz wave is identified throughout the entire time. The exact turn-on of the 17 kHz mode is difficult to discern based on the broad time range returned. It is noteworthy that the time resolved nature of the sudden turn-on is given accurately by the higher frequency behavior. The immediate injection of the 17 kHz signal carries with some type of δ-function influence that causes power to be calculated for all frequencies. In this way, any sudden event in a time series can be determined to reasonable accuracy through the wavelet method, regardless of any particular frequency that may be associated with the phenomenon.

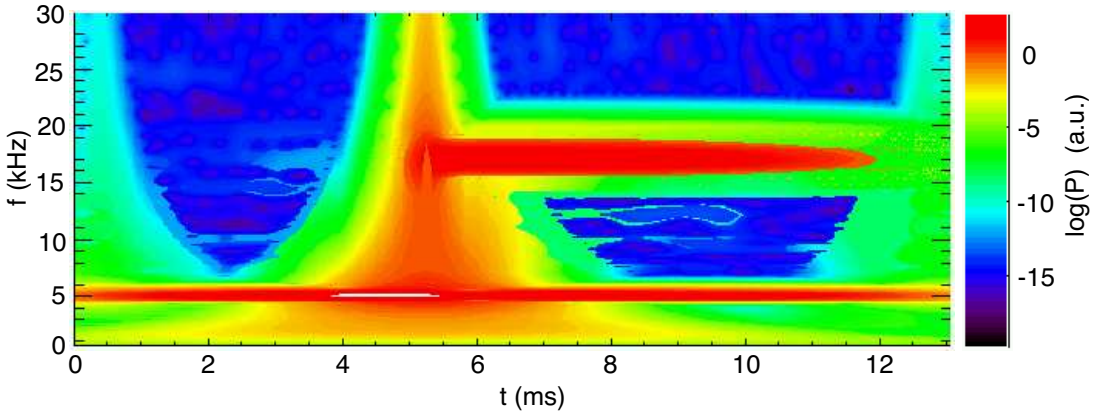

Figure A.5: Spectrogram calculated using the CWT technique on the evolving frequency test signal. The appearance of the 17 kHz oscillation is evident, though the best time resolution for marking this abrupt change comes at higher frequencies.

A.5 Experimental Data

Figure A.6 presents spectrograms (power spectra over time) from the temperature filament experiment that demonstrate the differences between CWT and FFT analyses. These spectra are calculated from measurements of electron temperature in the outer region of the filament in an experiment for which the background magnetic field is $B_o = 900$ G.

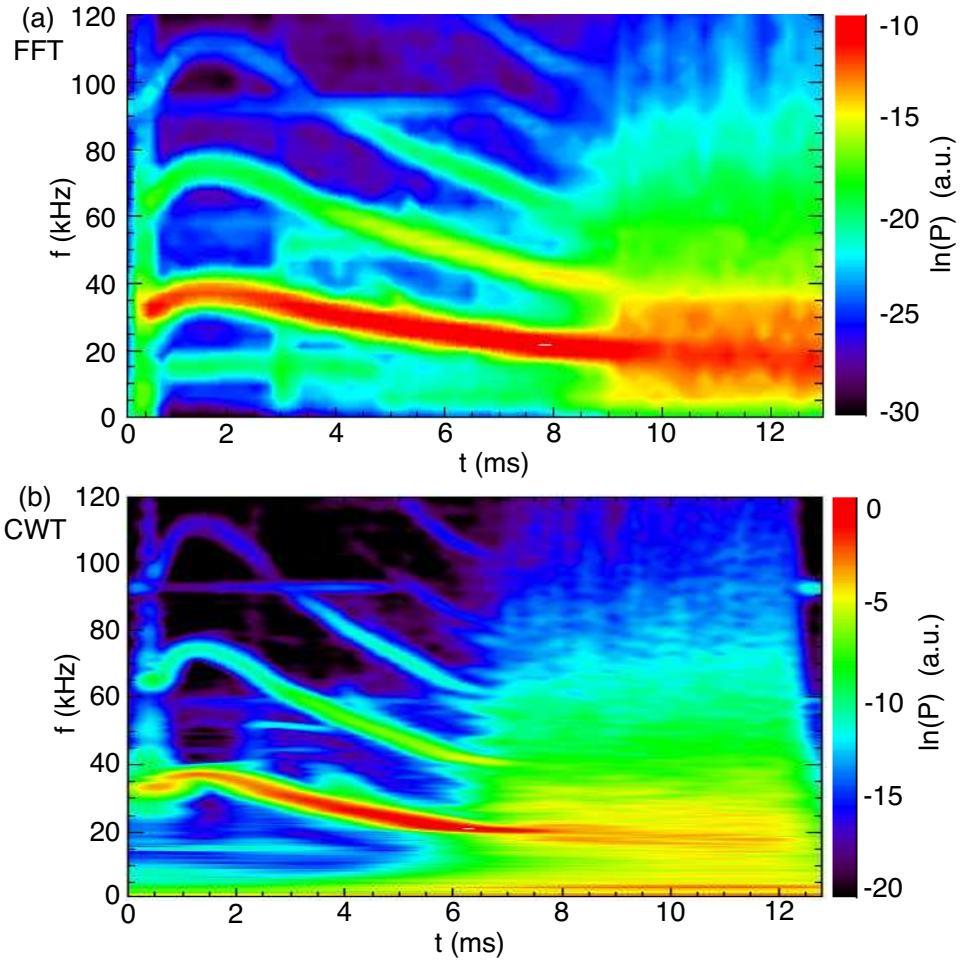

Figure A.6: (a) Spectrogram calculated using a sliding FFT window to compute the spectrum for individual times. The central time of the FFT window is used to position the result. The transition to broadband turbulence appears as a sharp event at $t = 9$ ms. (b) Spectrogram calculated using the CWT method. The transition to turbulence appears as a process beginning near $t = 7$ ms.

In Fig. A.6a a coherent drift-Alfvén mode ($f \approx 30$ kHz) and its harmonics is observed to Doppler shift during the first 9 ms of the temporal evolution. This same mode is clearly visible in the CWT representation of Fig. A.6b. Any

differences in frequency resolution between these methods is insignificant. In fact, the CWT results in a seemingly better identification of mode frequency for the drift-Alfvén wave. The delay between time zero (beginning of beam heating) and the appearance of features within the spectrograms is due to the time it takes for these features to appear at the measurement position 256 cm axially separated from the beam.

The most striking difference between these two results concerns the temporal features of the transition to broadband spectra. The FFT result of Fig. A.6a shows a sharp transition from the coherent mode to a broadband spectra at $t = 9$ ms. The CWT result of A.6b indicates that this transition may not be as dramatic and that it begins earlier than $t = 9$ ms. The sharp transition shown in the FFT spectrogram results from the windowing method employed. The windowed FFT computes a handful of individual spectra over user-defined time regions of the input time series. The larger the time window used, the better the frequency resolution of the spectra according to the Δf relation given earlier. Improved frequency is achieved by reducing temporal resolution. The sharp transition in the FFT spectrogram appears because one window covers none of the broadband fluctuations while the next window is the first one to detect them. The window that first detects them returns a significantly different result from the preceding window. The CWT method does not window across the data and therefore provides a better temporal resolution in this case (the poor frequency resolution at high frequencies is the tradeoff for this method). It is generally the case that a combination of FFT and CWT techniques provides the most complete analysis of spectral features in an experiment.

APPENDIX B

Pulse Detection Techniques

B.1 Overview

The study of exponential spectra and accompanying Lorentzian pulses in time series data requires that the pulses be isolated for determining their characteristic widths. A variety of identification techniques have been applied to the large data set of this experiment, and notes on two of these methods are provided here so that they may be further developed in future studies. The brute force method of sliding a Lorentzian shape through an entire time series is described in Section 4.3. The two other methods described here are the wavelet phase method in which constant phase over all frequencies identifies a pulse event, and the amplitude threshold method in which events of statistically significant amplitude are identified as pulses.

B.2 Wavelet Phase Method

Some aspects of wavelet transform techniques, including a comparison of their power spectra results to those of the more familiar Fourier methods, are discussed in Appendix A. The phase of a time series as calculated with wavelet techniques can be used to identify pulses because any singularity exhibits a constant phase [Farge, 1992] over all frequencies. Lorentzian pulses in this experiment are not

necessarily singularities, and those with larger time widths are less so than narrower pulses. In spite of this difficulty, the wavelet phase method still appears to identify pulses fairly well.

Using the CWT as given in Eq. (A.2), which is a complex valued function for the Morlet wavelet basis, the phase, ϕ, is determined from,

$$\phi \;=\; \tan^{-1}\left(\frac{\mathrm{I}(\mathcal{W})}{\mathrm{R}(\mathcal{W})}\right) \;, \tag{B.1}$$

where I and R signify the imaginary and real parts of the CWT respectively. The value of the phase at any frequency ranges from $-\pi$ to $+\pi$.

B.2.1 Test Lorentzian Pulses

Figure B.1 presents the phase contours of two test signal Lorentzian pulses. One of these is narrower than the other, $\tau = 0.5$ μs compared to $\tau = 4$ μs. Both contours clearly identify a pulse by the symmetry of the phase values. The narrower pulse of the left panel more accurately reproduces the behavior of a singularity and the phase contour is remarkably sharper than that of the wider pulse in the right panel.

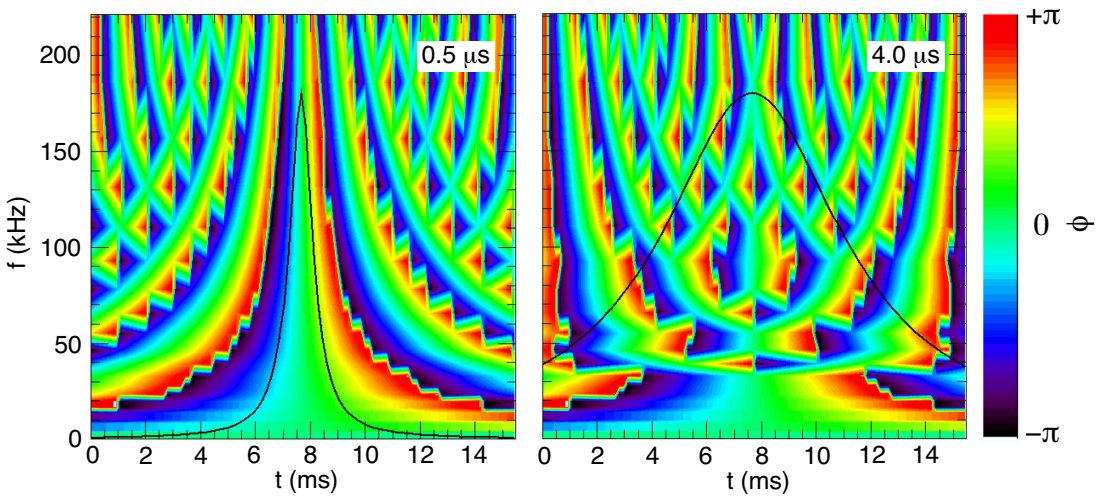

Figure B.1: Phase contours of test signal Lorentzian pulses. The left panel shows the well defined phase pattern of a narrow ($\tau = 0.5$ μs, overplotted) Lorentzian pulse. The right panel shows that wider pulses ($\tau = 4$ μs, overplotted) still exhibit symmetry about the event, but that constant phase as a function of frequency is not as evident as for the narrower pulse.

Phase as a function of frequency for test signal Lorentzian pulses is shown in Fig. B.2. It is observed that narrower pulses demonstrate a more constant phase across the range of frequencies returned.

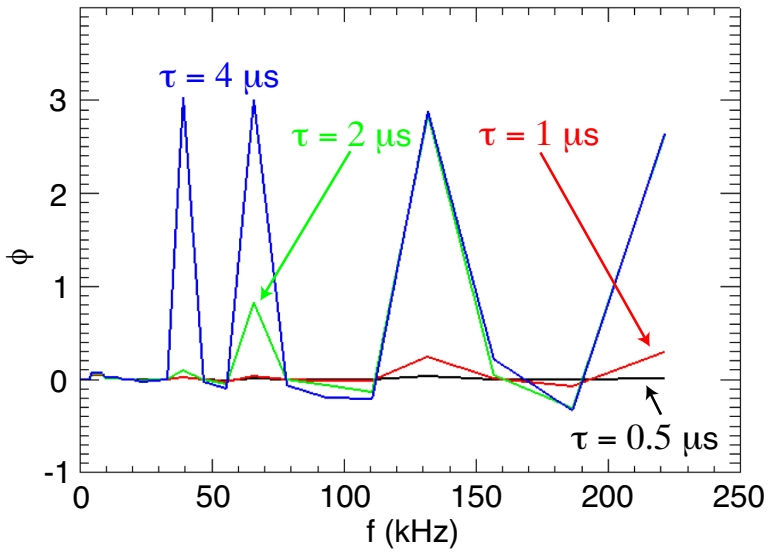

Figure B.2: Phase versus frequency for test signal Lorentzian pulses of varying width. The narrowest pulse, $\tau = 0.5$ μs, results in the most constant value of phase.

Measurements of Lorentzian pulses show that they can be either positive or negative polarity. Figure B.3 compares the phases of test signal Lorentzian pulses for each polarity. Both phase contours exhibit symmetry about the center of the pulse, but the negative polarity pulse features a much narrower region of zero phase. This result suggests that negative polarity pulses can be accurately identified by the wavelet phase technique, and even if this proves prohibitively difficult it is a simple task to invert the raw signals and apply the standards developed to isolate positive polarity events.

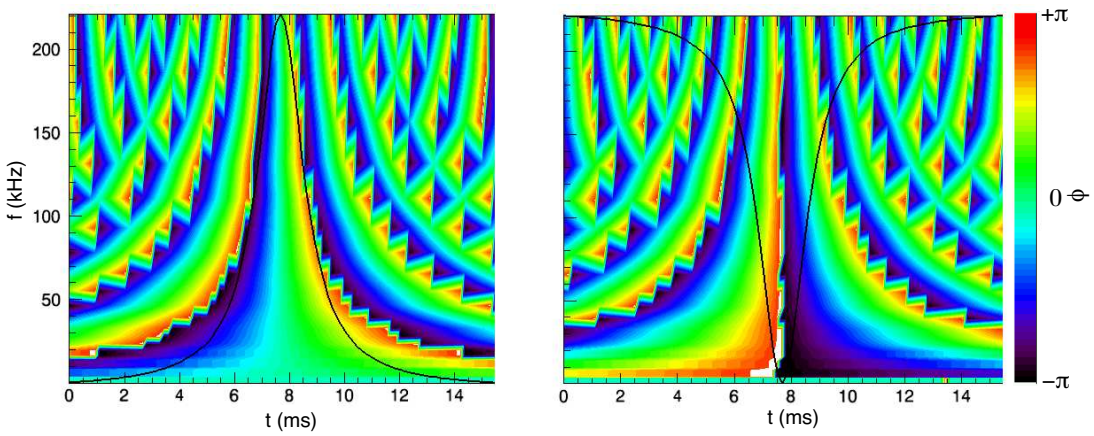

Figure B.3: The wavelet phase is shown for positive (left panel) and negative (right panel) Lorentzian pulses. In both panels the test signal Lorentzian features $\tau = 1$ μs and is overplotted in solid black.

B.2.2 Application to Experimental Results

Figure B.4 presents a measured pulse and its corresponding wavelet phase representation. The measurement is made in the outer region at $r = 0.55$ cm and features a large amplitude positive polarity pulse. The phase contour demonstrates excellent symmetry across the time of $t = 7.17$ ms where the pulse event is centered. This particular pulse exhibits a phase relationship that indicates it is similar to a singularity.

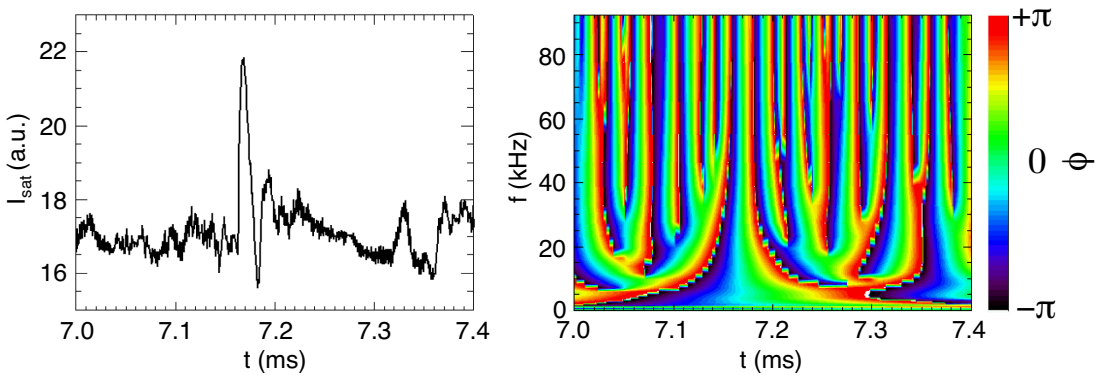

Figure B.4: A pulse event from the experiment (left panel) and its wavelet phase representation (right panel). The pulse is clearly identified in the phase representation at $t = 7.17$ ms.

B.2.3 Limitations of the Wavelet Phase Detection Technique

An immediately apparent limitation of this technique is that it identifies only singularities, not Lorentzian pulses. In a best case scenario, the wavelet phase could be examined to determine the most likely temporal locations of Lorentzian pulses. These events could be extracted and then passed through a secondary analysis to determine whether they have any particular shape. Such a procedure essentially employs the same curve fitting technique as described in Section 4.3. That method simultaneously identifies events and classifies them as Lorentzian or non-Lorentzian, removing the need for the initial wavelet phase calculation. It is possible that the wavelet phase is useful in selecting out events that are embedded in background coherent fluctuations. In this case, the phase may be better suited for identifying a non-coherent mode related pulse which can then be further studied to determine whether it is a Lorentzian. This overcomes a limitation to the curve fitting technique in that fitting errors may incorrectly identify parts of a coherent oscillation as a unique Lorentzian pulse.

B.3 Amplitude Threshold Method

The amplitude threshold method isolates pulse events (again, not necessarily Lorentzian pulses) that exhibit statistically significant large amplitude. This is sometimes called "conditional averaging" in cases where the large amplitude events serve as triggers that set a reference time for another phenomenon.

Figure B.5 presents two raw measurements from the same discharge but different spatial positions. The I_{sat} trace is measured at $(r, z) = (0.5, 192)$ cm and the V_{f} trace is measured at $(r, z) = (0.35, 544)$ cm. With an axial separation of $\Delta z = 352$ cm, the correlation between the turbulent pulse region on both traces is interesting. The amplitude threshold method of pulse detection is used to study such correlations by allowing for the generation of ensemble profiles from a moving probe (in this case, the V_{f} measuring probe) based on the occurrence of similar pulses measured with a fixed I_{sat} probe.

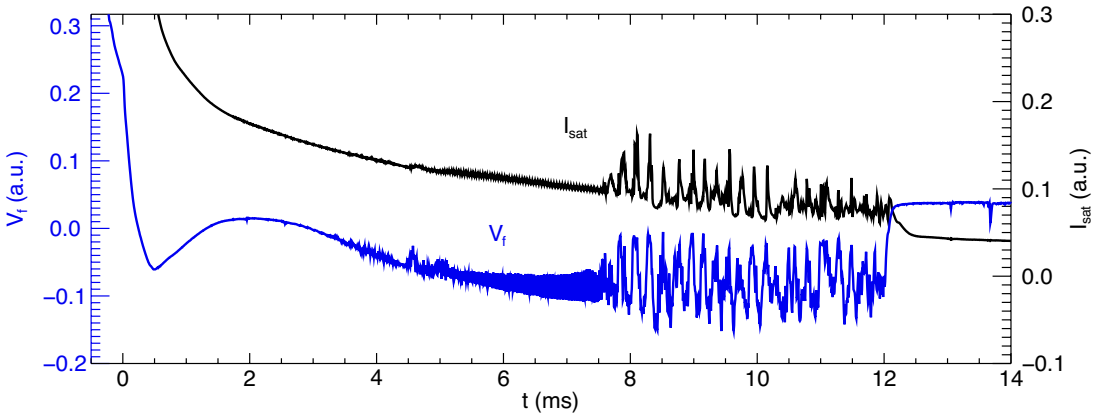

Figure B.5: Same shot time series highlighting the correlation between pulses separated in position. The I_{sat} trace (solid black, top) is placed in the outer region and detects little other than pulses. The V_{f} trace (solid blue, bottom) is placed in the gradient region and measures both coherent modes and turbulent pulses.

The identification of pulse events begins by calculating the standard deviation (σ), or root-mean-square (RMS), of the fluctuations in a signal. Figure B.6 is a plot of both the fluctuating component of the I_{sat} signal (originally seen in Fig. B.5) and the RMS level as computed by a sliding window. The sliding window computes the RMS level for a limited time range of the entire signal and then translates the center of the window to calculate subsequent values. In this example, the RMS trace is useful for determining the likely beginning of the turbulent regime of the system. The increase in fluctuation level just after $t = 7$ ms suggests some type of transition has occurred, though it does not necessarily indicate anything about the presence of Lorentzian pulses.

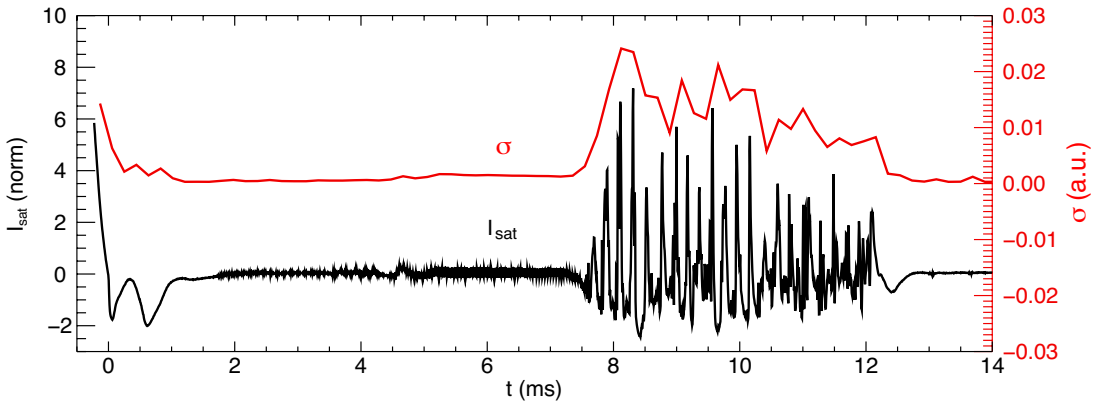

Figure B.6: The fluctuating component of the I_{sat} signal from Fig. B.5 (black, bottom) and the RMS value (red, top) calculated with a sliding window.

An RMS value calculated over the entire time series of a single discharge is used to search for pulses. From a computational perspective, once the threshold has been assigned, any points above that value are collected as possible pulse peaks. For any sets of points that occur in sequence (i.e., any continuous collection of values that are all above the threshold), only points that represent local maxima are returned. This allows for the detection of overlapping pulses so long

as they are minimally distinct.

Figure B.7 shows spikes in the data of Figs. B.5 and B.6 as found by the threshold technique. In this example the threshold level is set at 2.0, meaning that only features extended greater than two standard deviations above the fluctuation level for the entire signal are kept.

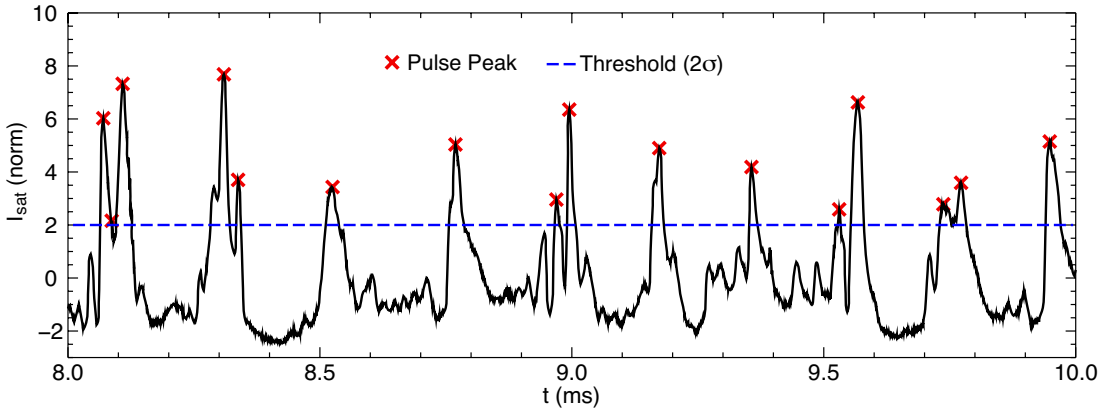

Figure B.7: A narrow time series of the previously shown I_{sat} measurements with pulse peaks identified according to the amplitude threshold method.

Figure B.8 highlights a weakness of the threshold method. If the level is set too low, then common oscillatory features are likely to be branded as pulses. In Fig. B.8 this is seen near the time $t = 8.085$ ms. At that time position there is a small oscillation (similar to those seen in the vicinity of $t = 8.12$ ms) that results in a peak. While the true fluctuation amplitude of this peak is small, by riding on top of the larger oscillation it satisfies the detection criteria and is labeled a pulse peak. Other similar looking features within this time range may appear as peaks, but actually feature flat regions without a singular maxima. The vector representation of the plot trace may result in the appearance of sharp peaks when none are present. In order to minimize erroneous spike detection the threshold should be set as high as possible.

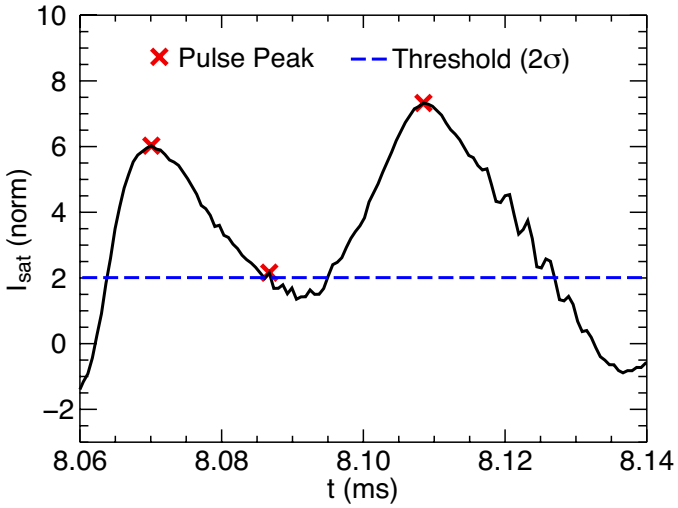

Figure B.8: Zoomed in view of I_{sat} trace highlighting a false positive from the amplitude threshold detection method. The middle pulse peak does not correspond to an actual pulse event.

While the shape of the pulses is not determined by this method, it may be safely assumed that a confirmation of their shape can be coupled with this conditional analysis to begin a study of the transport caused by pulses. At the very least, this type of analysis helps to determine the amount of transport that leads to the generation of outer region pulses.

Bibliography

A. J. Ångström. Neue methode, das wärmeleitungsvermögen der körper zu bestimmen. Ann. Phys. Chem., 190(12):513–530, 1862.

Ghassan Y. Antar, Glenn Counsell, Yang Yu, Brian Labombard, and Pascal Devynck. Universality of intermittent convective transport in the scrape-off layer of magnetically confined devices. Phys. Plasmas, 10(2):419–428, 2003. doi: 10.1063/1.1536166. URL http://link.aip.org/link/?PHP/10/419/1.

B. Z. Azmi, H. S. Liaw, and Z. Abbas. Thermal-wave interferometry of gas-liquid applied to a thermal-wave resonator cavity technique. Rev. Sci. Inst., 76(7): 074901, 2005. doi: 10.1063/1.1946547. URL http://link.aip.org/link/?RSI/76/074901/1.

J. A. Balderas-López, A. Mandelis, and J. A. Garcia. Thermal-wave resonator cavity design and measurements of the thermal diffusivity of liquids. Rev. Sci. Inst., 71(7):2933–2937, 2000. doi: 10.1063/1.1150713. URL http://link.aip.org/link/?RSI/71/2933/1.

S. D. Bale, P. J. Kellogg, F. S. Mozer, T. S. Horbury, and H. Reme. Measurement of the electric fluctuation spectrum of magnetohydrodynamic turbulence. Phys. Rev. Lett., 94(21):215002, 2005. doi: 10.1103/PhysRevLett.94.215002. URL http://link.aps.org/abstract/PRL/v94/e215002.

J. S. Bendat and A. G. Piersol. Random Data: Analysis and Measurement Procedures, page 148. Wiley-Interscience, third edition, 2000.

M. Bertolotti, G. L. Liakhou, R. Li Voti, S. Paoloni, and C. Sibilia. Thermal wave resonator: In situ investigation by photothermal deflection technique.

Int. J. Therm., 19(2):603–613, 1998. doi: 10.1023/A:1022594201473. URL http://www.springerlink.com/content/u000r82364135733.

J. A. Boedo, D. Rudakov, R. Moyer, S. Krasheninnikov, D. Whyte, G. McKee, G. Tynan, M. Schaffer, P. Stangeby, P. West, S. Allen, T. Evans, R. Fonck, E. Hollmann, A. Leonard, A. Mahdavi, G. Porter, M. Tillack, and G. Antar. Transport by intermittent convection in the boundary of the diii-d tokamak. Physics of Plasmas, 8(11):4826–4833, 2001. URL http://link.aip.org/link/?PHP/8/4826/1.

S. I. Braginskii. Reviews of plasma physics. In M. A. Leontovich, editor, Reviews of Plasma Physics, volume 1, page 205. Consultants Bureau, New York, 1965.

Howard C. Bryant. Heat waves and Ångström's method. Am. J. Phys., 31(5): 325–327, 1963. doi: 10.1119/1.1969505. URL http://link.aip.org/link/?AJP/31/325/1.

V. P. Budaev, S. Masuzaki, T. Morisaki, N. Ohno, N. Asakura, S. Takamura, H. Yamada, and A. Komori. Scaling laws of intermittent plasma turbulence in edge of fusion devices. Plasma Fus. Res., 3:S1019, 2008.

A. T. Burke. Classical Heat Transport and Spontaneous Fluctuations associated with a Temperature Filament in a Magnetized Plasma. PhD thesis, University of California, San Diego, 1999.

A. T. Burke, J. E. Maggs, and G. J. Morales. Observation of simultaneous axial and transverse classical heat transport in a magnetized plasma. Phys. Rev. Lett., 81(17):3659–3662, Oct 1998. doi: 10.1103/PhysRevLett.81.3659.

A. T. Burke, J. E. Maggs, and G. J. Morales. Experimental study of fluctuations excited by a narrow temperature filament in a magnetized plasma. Physics of

Plasmas, 7(5):1397–1407, 2000a. URL http://link.aip.org/link/?PHP/7/1397/1.

A. T. Burke, J. E. Maggs, and G. J. Morales. Experimental study of classical heat transport in a magnetized plasma. Physics of Plasmas, 7(2):544–553, 2000b. URL http://link.aip.org/link/?PHP/7/544/1.

B. A. Carreras, R. Balbin, B. van Milligen, M. A. Pedrosa, I. Garcia-Cortes, E. Sanchez, C. Hidalgo, J. Bleuel, M. Endler, H. Thomsen, A. Chankin, S. Davies, K. Erents, and G. F. Matthews. Characterization of the frequency ranges of the plasma edge fluctuation spectra. Phys. Plasmas, 6(12):4615–4621, 1999. doi: 10.1063/1.873748. URL http://link.aip.org/link/?PHP/6/4615/1.

T. A. Carter. Intermittent turbulence and turbulent structures in a linear magnetized plasma. Physics of Plasmas, 13(1):010701, 2006. doi: 10.1063/1.2158929. URL http://link.aip.org/link/?PHP/13/010701/1.

Alessandro Casati, P. Mantica, D. Van Eester, N. Hawkes, F. Imbeaux, E. Joffrin, A. Marinoni, F. Ryter, A. Salmi, T. Tala, and P. De Vries JET EFDA contributors. Critical temperature gradient length signatures in heat wave propagation across internal transport barriers in the joint european torus. Phys. Plasmas, 14(9):092303, 2007. doi: 10.1063/1.2772618. URL http://link.aip.org/link/?PHP/14/092303/1.

Francis F. Chen. Spectrum of low-β plasma turbulence. Phys. Rev. Lett., 15(9):381–383, Aug 1965. doi: 10.1103/PhysRevLett.15.381.

Sin-Li Chen and T. Sekiguchi. Instantaneous direct-display system of plasma parameters by means of triple probe. Journal of Applied Physics, 36(8):2363–2375, 1965. URL http://link.aip.org/link/?JAP/36/2363/1.

Committee on Solar and Space Physics. Plasma Physics of the Local Cosmos. National Research Council, 2004.

L. Debnath. Wavelet transformations and their applications. Birkhäuser Boston, 2002.

D. A. D'Ippolito, J. R. Myra, and S. I. Krasheninnikov. Cross-field blob transport in tokamak scrape-off-layer plasmas. Physics of Plasmas, 9(1):222–233, 2002. doi: 10.1063/1.1426394. URL http://link.aip.org/link/?PHP/9/222/1.

T.E. Evans, M.E. Fenstermacher, R.A. Moyer, T.H. Osborne, J.G. Watkins, P. Gohil, I. Joseph, M.J. Schaffer, L.R. Baylor, M. Bécoulet, J.A. Boedo, K.H. Burrell, J.S. deGrassie, K.H. Finken, T. Jernigan, M.W. Jakubowski, C.J. Lasnier, M. Lehnen, A.W. Leonard, J. Lonnroth, E. Nardon, V. Parail, O. Schmitz, B. Unterberg, and W.P. West. Rmp elm suppression in diii-d plasmas with iter similar shapes and collisionalities. Nuclear Fusion, 48(2):024002 (10pp), 2008. URL http://stacks.iop.org/0029-5515/48/024002.

M. Farge. Wavelet transforms and their applications to turbulence. ANNUAL REVIEW OF FLUID MECHANICS, 24:395–457, 1992. URL http://link.aip.org/link/?PHP/14/052306/1.

G. Fiksel, S. C. Prager, P. Pribyl, R. J. Taylor, and G. R. Tynan. Measurement of magnetic fluctuation induced energy transport in a tokamak. Phys. Rev. Lett., 75(21):3866–3869, Nov 1995. doi: 10.1103/PhysRevLett.75.3866.

D. W. Forslund. Instabilities associated with heat conduction in the solar wind and their consequences. J. Geophys. Res., 75(1):17–28, 1970.

U. Frisch. Turbulence: The Legacy of A. N. Kolmogorov. Cambridge University Press, 1995.

W. Gekelman, H. Pfister, Z. Lucky, J. Bamber, D. Leneman, and J. Maggs. Design, construction, and properties of the large plasma research device - the lapd at ucla. Review of Scientific Instruments, 62(12):2875–2883, 1991. URL http://link.aip.org/link/?RSI/62/2875/1.

K. W. Gentle. Dependence of heat pulse propagation on transport mechanisms: Consequences of nonconstant transport coefficients. Phys. Fluids, 31(5):1105–1110, 1988. doi: 10.1063/1.866790. URL http://link.aip.org/link/?PFL/31/1105/1.

W. Horton. Drift waves and transport. Rev. Mod. Phys., 71(3):735–778, Apr 1999. doi: 10.1103/RevModPhys.71.735.

I. H. Hutchinson. Principles of Plasma Diagnostics, pages 70–72. Cambridge University Press, second edition, 2002.

A. Jacchia, P. Mantica, F. De Luca, and G. Gorini. Determination of diffusive and nondiffusive transport in modulation experiments in plasmas. Phys. Fluids B, 3(11):3033–3040, 1991. doi: 10.1063/1.859781. URL http://link.aip.org/link/?PFB/3/3033/1.

Kunihiro Kamataki, Yoshihiko Nagashima, Shunjiro Shinohara, Yoshinobu Kawai, Masatoshi Yagi, Kimitaka Itoh, and Sanae-I. Itoh. Coexistence of collisional drift and flute wave instabilities in bounded linear ecr plasma. J. Phys. Soc. Jpn., 76:054501, 2007.

U. Kauschke, G. Oelerich-Hill, and A. Piel. Experimental investigation of coherent drift waves in low magnetic fields. Phys. Fluids B, 2(1):38–43, 1990. doi: 10.1063/1.859537. URL http://link.aip.org/link/?PFB/2/38/1.

A.N. Kolmogorov. Dissipation of energy in locally isotropic turbulence. Dokl. Akad. Nauk SSSR, 32:16–18, 1941. (reprinted in Proc. Roy. Soc. Lond. A 434, 15-17 (1991)).

J. A. Krommes. Fundamental statistical descriptions of plasma turbulence in magnetic fields. Phys. Rep., 360(1-4):1–352, 2002. URL http://www.sciencedirect.com/science/article/B6TVP-44B20YF-1/2/a6228f0e751eeadca209858a8b5fe8b5.

F. S. Kuo and S. Y. Chou. The origin of the dual-slope spectrum from intermediate to transitional scale in equatorial spread f. Chinese J. Phys., 39(6): 577–593, 2001.

B Labit, A Diallo, A Fasoli, I Furno, D Iraji, S H Müller, G Plyushchev, M Podestà, F M Poli, P Ricci, C Theiler, and J Horacek. Statistical properties of electrostatic turbulence in toroidal magnetized plasmas. Plasma Phys. Cont. Fus., 49(12B):B281–B290, 2007. URL http://stacks.iop.org/0741-3335/49/B281.

Rolf Landshoff. Transport phenomena in a completely ionized gas in presence of a magnetic field. Phys. Rev., 76(7):904–909, Oct 1949. doi: 10.1103/PhysRev.76.904.

J. E. Maggs and G. J. Morales. Magnetic fluctuations of a large nonuniform plasma column. Phys. Plasmas, 10(6):2267–2277, 2003. doi: 10.1063/1.1572814. URL http://link.aip.org/link/?PHP/10/2267/1.

Andreas Mandelis. Diffusion waves and their uses. Phys. Today, 53(8):29–34, 2000. doi: 10.1063/1.1310118. URL http://link.aip.org/link/?PTO/53/29/1.

P. Mantica, D. Van Eester, X. Garbet, F. Imbeaux, L. Laborde, M. Mantsinen, A. Marinoni, D. Mazon, D. Moreau, N. Hawkes, E. Joffrin, V. Kiptily, S. Pinches, A. Salmi, S. Sharapov, A. Thyagaraja, I. Voitsekhovitch, P. de Vries, and K.-D. Zastrow. Probing internal transport barriers with heat pulses in jet. Phys. Rev. Lett., 96(9):095002, 2006. doi: 10.1103/PhysRevLett.96.095002. URL http://link.aps.org/abstract/PRL/v96/e095002.

L. J. Milano, S. Dasso, W. H. Matthaeus, and C. W. Smith. Spectral distribution of the cross helicity in the solar wind. Phys. Rev. Lett., 93(15):155005, Oct 2004. doi: 10.1103/PhysRevLett.93.155005.

D. C. Pace, M. Shi, J. E. Maggs, G. J. Morales, and T. A. Carter. Exponential frequency spectrum in magnetized plasmas. Phys. Rev. Lett., 101(8):085001, 2008a. doi: 10.1103/PhysRevLett.101.085001. URL http://link.aps.org/abstract/PRL/v101/e085001.

D. C. Pace, M. Shi, J. E. Maggs, G. J. Morales, and T. A. Carter. Spontaneous thermal waves in a magnetized plasma. Phys. Rev. Lett., 101(3):035003, 2008b. doi: 10.1103/PhysRevLett.101.035003. URL http://link.aps.org/abstract/PRL/v101/e035003.

M. A. Pedrosa, C. Hidalgo, B. A. Carreras, R. Balbín, I. García-Cortés, D. Newman, B. van Milligen, E. Sánchez, J. Bleuel, M. Endler, S. Davies, and G. F. Matthews. Empirical similarity of frequency spectra of the edge-plasma fluctuations in toroidal magnetic-confinement systems. Phys. Rev. Lett., 82(18):3621–3624, May 1999. doi: 10.1103/PhysRevLett.82.3621.

J. R. Peñano, G. J. Morales, and J. E. Maggs. Drift-alfvén fluctuations associated with a narrow pressure striation. Physics of Plasmas, 7(1):144–157, 2000. URL http://link.aip.org/link/?PHP/7/144/1.

M. N. Rosenbluth and A. N. Kaufman. Plasma diffusion in a magnetic field. Phys. Rev., 109(1):1–5, Jan 1958. doi: 10.1103/PhysRev.109.1.

Jun Shen and Andreas Mandelis. Thermal-wave resonator cavity. Review of Scientific Instruments, 66(10):4999–5005, 1995. doi: 10.1063/1.1146123. URL http://link.aip.org/link/?RSI/66/4999/1.

M. Shi. PhD thesis, University of California, Los Angeles, 2008.

T. Shikama, S. Kado, A. Okamoto, S. Kajita, and S. Tanaka. Practical formula for mach number probe diagnostics in weakly magnetized plasmas. Physics of Plasmas, 12(4):044504, 2005. doi: 10.1063/1.1872895. URL http://link.aip.org/link/?PHP/12/044504/1.

Lyman Spitzer and Richard Härm. Transport phenomena in a completely ionized gas. Phys. Rev., 89(5):977–981, Mar 1953a. doi: 10.1103/PhysRev.89.977.

Lyman Spitzer and Richard Härm. Transport phenomena in a completely ionized gas. Phys. Rev., 89(5):977–981, Mar 1953b. doi: 10.1103/PhysRev.89.977.

Stanford-Lockheed Institute for Space Research, 2000. URL http://soi.stanford.edu/results/SolPhys200/Schrijver/TRACEpodarchive4.html.

U. Stroth, F. Greiner, C. Lechte, N. Mahdizadeh, K. Rahbarnia, and M. Ramisch. Study of edge turbulence in dimensionally similar laboratory plasmas. In 45th Annual Meeting of the APS Division of Plasma Physics, volume 11, pages 2558–2564. AIP, 2004. doi: 10.1063/1.1688789. URL http://link.aip.org/link/?PHP/11/2558/1.

C. M. Tchen. Turbulent motions in an artificial plasma inhomogeneity released in the ionosphere. Plasma Phys., 15:1193–1196, 1973.

V. T. Tikhonchuk, W. Rozmus, V. Yu. Bychenkov, C. E. Capjack, and E. Epperlein. Return current instability in laser heated plasmas. Phys. Plasmas, 2(11): 4169–4173, 1995. doi: 10.1063/1.871041. URL http://link.aip.org/link/?PHP/2/4169/1.

C. Torrence and G. P. Compo. A practical guide to wavelet analysis. Bull. Amer. Meteor. Soc., 79:61, 1998.

UKAEA. URL http://www.york.ac.uk/depts/phys/gsp/plasma_projs/fusionplasmas.htm.

M. Škorić and M. Rajković. Characterization of intermittency in plasma edge turbulence. Cont. Plasma Phys., 48(1-3):37–41, 2008. doi: 10.1002/ctpp.200810006.

H. Xia and M. G. Shats. Inverse energy cascade correlated with turbulent-structure generation in toroidal plasma. Phys. Rev. Lett., 91(15):155001, Oct 2003. doi: 10.1103/PhysRevLett.91.155001.

G. Zimbardo. Magnetic turbulence in space plasmas: in and around the earth's magnetosphere. Plasma Phys. Cont. Fus., 48(12B):B295–B302, 2006. URL http://stacks.iop.org/0741-3335/48/B295.

S. J. Zweben. Search for coherent structure within tokamak plasma turbulence. Phys. Fluids, 28(3):974–982, 1985. doi: 10.1063/1.865069. URL http://link.aip.org/link/?PFL/28/974/1.

S J Zweben, J A Boedo, O Grulke, C Hidalgo, B LaBombard, R J Maqueda, P Scarin, and J L Terry. Edge turbulence measurements in toroidal fusion devices. Plasma Phys. Cont. Fus., 49(7):S1–S23, 2007. URL http://stacks.iop.org/0741-3335/49/S1.